Scattering correction in cone beam tomography using continuously thickness-adapted kernels

Navnina Bhatia

N°d'ordre NNT : 2016LYSEI092

THESE de DOCTORAT DE L'UNIVERSITE DE LYON

Opérée au sein de

Institut national des sciences appliquées de Lyon

Ecole Doctorale N° 160
Électronique, Électrotechnique, Automatique

Spécialité de doctorat : Traitement du signal et de l'Image

Soutenue publiquement le 29 Septembre 2016 par :

Navnina Bhatia

Scattering correction in cone beam tomography using continuously thickness-adapted kernels

Correction du diffusé en tomographie par une méthode de convolution par noyaux continus

---

Jury

Alessandro Olivo	Professeur, University College of London	Rapporteur
Jan Sijbers	Professeur, University of Antwerp	Rapporteur
Dimitris Visvikis	Directeur de recherche, Université de Brest	Examinateur
Jean Michel Létang	Maître de conférence, CREATIS	Directeur de thèse
David Tisseur	Ingénieur de recherche, CEA	Examinateur

CEA, LIST
Département d'Imagerie et de Simulation pour le Contôle (DISC)

INSTITUT NATIONAL DES SCIENCES APPLIQUÉES LYON

INSA LYON
Service Scolarité
Bât Camille Claudel

Année Universitaire 2015-2016

ECOLES DOCTORALES – SPECIALITES
A REMPLIR LORS DE VOTRE INSCRIPTION

A établir obligatoirement avec votre directeur de thèse

Nom : Bhatia Prénom : Navnina Singh **Signature :** Navnina

ECOLES DOCTORALES n° code national	SPECIALITES	Cocher la case correspondante
ED CHIMIE DE LYON (Chimie, Procédés, Environnement) EDA206	Chimie	☐
	Procédés	☐
	Environnement	☐
HISTOIRE, GEOGRAPHIE, AMENAGEMENT, URBANISME, ARCHEOLOGIE, SCIENCE POLITIQUE, SOCIOLOGIE, ANTHROPOLOGIE (ScSo) EDA483	Géographie – Aménagement - Urbanisme	☐
ELECTRONIQUE, ELECTROTECHNIQUE, AUTOMATIQUE (E.E.A.) EDA160	Automatique	☐
	Génie Electrique	☐
	Electronique, micro et nanoélectronique, optique et laser	☐
	Ingénierie pour le vivant	☐
	Traitement du Signal et de l'Image	☒
EVOLUTION, ECOSYSTEMES, MICROBIOLOGIE , MODELISATION (E2M2) EDA 341	Paléoenvironnements et évolution	☐
	Micro-organismes, interactions, infections	☐
	Biologie Evolutive, Biologie des Populations, écophysiologie	☐
	Biomath-Bioinfo-Génomique évolutive	☐
	Ecologie des communautés, fonctionnement des écosystèmes, écotoxicologie	☐
INFORMATIQUE ET MATHEMATIQUES DE LYON (InfoMaths) EDA 512	Informatique	☐
	Informatique et applications	☐
	Mathématiques et applications	☐
INTERDISCIPLINAIRE SCIENCES-SANTE (EDISS) EDA205	Biochimie	☐
	Physiologie	☐
	Ingénierie biomédicale	☐
ED MATERIAUX DE LYON EDA 034	Matériaux	☐
MEGA DE LYON (MECANIQUE, ENERGETIQUE, GENIE CIVIL, ACOUSTIQUE) (MEGA) EDA162	Mécanique des Fluides	☐
	Génie Mécanique	☐
	Biomécanique	☐
	Thermique Energétique	☐
	Génie Civil	☐
	Acoustique	☐

Pour le Directeur de l'INSA Lyon
Et par délégation

Marie-Christine BAIETTO
Directrice du Département FEDORA
Formation par la Recherche Et des Etudes Doctorales

Cette liste est mise à jour annuellement par le Département FEDORA, en collaboration avec les Ecoles Doctorales.

To My Mother

Acknowledgment

This PhD thesis is not just an individual work, rather it has been created with guidance, help, encouragement and cooperation of many and I would like to thank them individually below.

First and foremost, I want to thank my thesis supervisor Jean Michel Létang. This study could not have been possible without his expertise and guidance. He has put his valuable experience and wisdom in this thesis. He provided critical advice on all the results and suggested many important additions and improvements in this thesis. It has been greatly enriching experience for me to work under his supervision. I want to thank him for believing in me to finish this study with success.

I would like to give my sincere gratitude to my CEA supervisor, David Tisseur, who has been the sole of this thesis work. It is his encouragement and enthusiasm that has made this thesis successful. He was always available throughout my PhD to answer all my questions and guide me in the right direction. In spite of his busy schedule, he was never short of time for his PhD students. He has provided many important insights for this thesis. Hands down, I dedicate this thesis to him.

I gratefully thank my team and fellow PhD students at CEA for their help and encouragement.

I thank all my friends in France and India for their support. Vishnu for all his help and encouragement specially at times when I was stressed. A special deserving thanks to my brother, who has always been a source of inspiration, for always being there for backing and encouragement. My father, for always being supportive. Though I always give credit to mummy, I secretly know I could not have achieved this success without constant encouragement and support by my father. I hope this doctorate degree will make him proud. Last but not the least, I want to thank my mother, without whose struggles and patience, her children would not have accomplished success. Thank you for her unconditional love.

Abstract

Advanced Cone Beam Computed Tomography (CBCT) typically uses a divergent cone-beam source and a large area detector. As a result, there is an inevitable increase in the size area of illumination causing an increase in the intensity of X-ray scatter signal, both from the object and the detector. This leads to the violation of prime assumption of reconstruction process which is based on straight line path integrals followed by the photons. Consequently scatter artifacts appear in the reconstruction images as steaks, cupping effect and thus produce wrong reconstruction values. Due to the severity of the reconstruction artifacts caused by scatter, many scatter corrections methods have been adopted in literature. The first part of this study reviews most of the existing scatter correction methods. The effect of scattering becomes more prominent and challenging in case of X-ray source of high energy which is used in industrial Non Destructive Testing (NDT), due to higher scatter to primary ratio (SPR). Therefore, in this study, we propose a continuously thickness-adapted deconvolution approach based on improvements in the Scatter Kernel Superposition (SKS) method. In this method, the scatter kernels are analytically parameterized over the whole thickness range of the object under study to better sample the amplitude and shape of kernels with respect to the thickness. The method is tested for both homogeneous and heterogeneous objects as well as simulated and experimental data. Another important aspect of this study is the comprehensive evaluation of the contribution of the detector scatter performed using continuous method by separating the contribution of scatter due to the object and the detector. This is performed by modeling the scatter kernels using a four-Gaussian model. In the first approach, we performed this evaluation based on simulation of kernels from Monte Carlo simulations and the corrections are performed on typical industrial experimental data. The obtained results prove that the scatter correction due to the object only is not sufficient to obtain reconstructed images, free from artifacts, as the detector also scatters considerably. In order to prove this point experimentally and to have a better modeling of the detector, we describe a method based on combination of experiments and simulations to calculate the scatter kernels. The results obtained also prove that the contribution of the detector scattering becomes important and that the PSF of the detector is not constant as considered in the studies so far, but it varies to a great extent with the energy spectrum.

Keywords : 3D Computed Tomography, scatter artifact, detector scatter, NDT, scatter correction

Résumé

La tomodensitométrie intégrant une source de rayons X à faisceau divergent et un détecteur grand champ est une technique bien connue dans le domaine de la tomographie industrielle. La nature des matériaux et les épaisseurs traversées conduisent inévitablement à la génération de rayonnement diffusé. Ce dernier est généré par l'objet mais également par le détecteur. La présence de rayonnement parasite conduit à ne plus respecter l'hypothèse de la loi de Beer-Lambert. Par conséquent, on voit apparaitre sur les coupes tomographiques des artefacts de reconstruction comme des streaks, des effets ventouses ou des valeurs d'atténuation linéaire erronée. Par conséquence, on retrouve dans la littérature de nombreuses méthodes de correction du diffusé. Ce travail vise à mettre en point et tester une méthode originale de correction du diffusé. Le premier chapitre de cette étude, dresse un état de l'art de la plupart des méthodes de corrections existantes. Nous proposons, dans le deuxième chapitre, une évolution de la méthode de superposition des noyaux de convolution (Scatter Kernel Superposition). Notre méthode repose sur une description continue des noyaux en fonction de l'épaisseur traversée. Dans cette méthode, les noyaux de diffusion sont paramétrés analytiquement sur toute la plage d'épaisseur. Le procédé a été testé pour des objets à la fois mono-matériaux et poly-matériaux, ainsi que sur des données expérimentales et simulées. Nous montrons dans le troisième chapitre l'importance de la contribution du diffusé détecteur dans la qualité de l'image reconstruite. Mais également l'importance de décrire les noyaux de convolution à l'aide d'un modèle à quatre gaussienne. Les résultats obtenus à partir de données expérimentales prouvent que la correction du diffusé de l'objet seul ne suffit pas pour obtenir une image de reconstruite sans artefacts. Afin de disposer d'une meilleur modélisation du diffusé du détecteur, nous décrivons, dans le dernier chapitre, une méthode basée sur la combinaison de données expérimentales et simulées permettant d'améliorer l'estimation des noyaux de diffusé.

List of Symbols

d_{OD}	Object-to-detector distance
I	Measured intensity
I_o	Unattenuated intensity
K	Total scatter kernel
K_d	Detector scatter kernel
K_o	Object scatter kernel
k	Total scatter kernel weight
k_d	Detector scatter kernel weight
k_o	Object scatter kernel weight
P	Primary intensity
S	Scatter intensity
T	True object thickness
t	Index of range of thickness
W	Integral of point spread function
ρ_e	Electronic density
λ	Relaxation parameter

List of Acronyms

CBCT	Cone Beam Computed Tomography
CIVA	NDT simulation software developed at CEA
CNR	Contrast to Noise Ratio
CPU	Central Processing Unit
CT	Computed Tomography
ESF	Edge Spread Function
FBP	Filtered Back Projection
FDK	Feldkamp, Davis and Kress
FOV	Field of View
GPU	Graphical Processing Unit
LSF	Line Spread function
LUT	Look Up Table
MC	Monte Carlo
MTF	Modulation Transfer Function
NDT	Non Destructive Testing
NIST	National Institute of Standards and Technology
PSF	Point Spread function
SKS	Scatter Kernel Superposition
SNR	Signal to Noise Ratio
SPR	Scatter to Primary Ratio
TFT	Thin Film Transistor
VOI	Volume of Interest
WET	Water Equivalent Thickness

Contents

List of Figures

List of Tables

Chapter 1

Scattering correction in cone beam tomography

1.1 Introduction

X-ray Cone Beam Computed Tomography (CBCT) has been widely used for both industrial Non-Destructive Testing (NDT) and medical imaging applications for obtaining three dimension images of the object under study. Advanced CBCT typically uses a divergent cone-beam source and a large-area detector. This increase in the size of X-ray illumination inevitably results in an increase of the X-ray scatter contibution on the projection images. However, in the standard reconstruction theory, reconstruction of the 3D images using these projections is performed using straight-line integrals of the X-ray passing through the object under study. This prime assumption of the straight line integrals is violated due to presence of scattered photons which are randomly oriented. Therefore, these scatter signals in CBCT degrade the image quality by reducing contrast and causing severe reconstruction artifacts like streaking and cupping effect, thus greatly hamper the applications of CBCT.

Due to the severity of the artifacts caused by scattering of photons in CBCT, a lot of research has gained importance over the years on the correction of scatter artifacts. This chapter aims at describing the basics of cone beam computed tomography. The scatter artifact in CBCT is described in detail, beginning from the arising cause of scatter artifact due to various sources of scatter in CBCT. This chapter also aims at providing a review of the existing scatter correction techniques which are broadly summarized in two categories: pre-processing and post-processing methods. A brief summary of various scatter correction methods is provided with advantages and concerns of each method. Finally in the concluding section of this chapter, our motivation for scatter correction using continuously thickness-adapted kernels method is described.

Summary

1.2 Basics of cone beam computed tomography

CBCT is an imaging technology used in medical as well as industrial applications to produce 3D visualizations of the object under study. The 3D geometry visualization of the object are produced by performing tomographic reconstruction on a large number of 2D X-ray images taken around the object in either a full 360 ˚rotation scanning or the recent advances of limited angle rotation scanning.

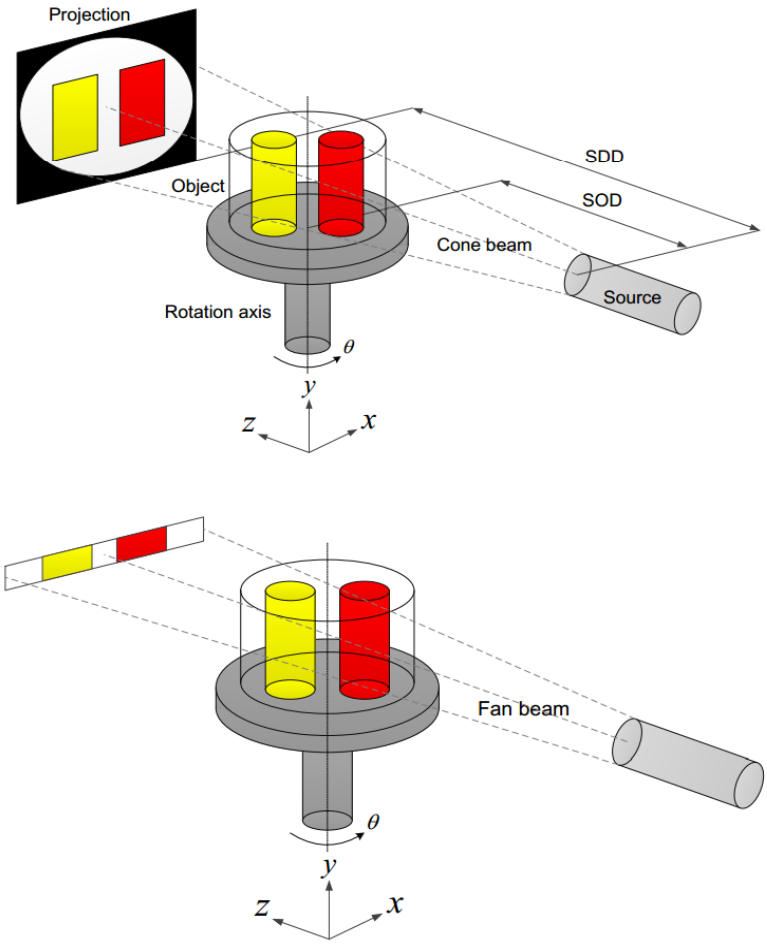

Figure 1.1: Schematic of acquisition with Cone Beam Computed Tomography and fan beam tomography [1]

Figure 1.1 shows the standard geometrical setup in CBCT with an X-ray cone beam source and Flat Panel Detector (FPD) rotating around a perpendicular axis passing through the object under study. An X-ray source emits a cone beam of X-ray that are attenuated as they propagate through an object and 2D attenuation profiles in term of projections are formed on the detector by the incident photons. This conical shape of the beam distinguishes this method from classical fan beam CT, which uses fan-shaped beam source to obtain 1D projections (figure 1.1). As a result of the acquisition of the 2D projections at each angle in CBCT, only one rotation or less is needed to acquire a full (3D) data set.

The obtained projections from all angles are then reconstructed into a 3D matrix, containing volume elements (voxels) each having a certain grey value which represents

the linear attenuation coefficient within this volume element. The grey value for each voxel is determined by the reconstruction algorithm (section 1.2.3), which combines the information from all obtained projections.

1.2.1 X-ray interaction with matter

This study focuses on the scatter correction for the X-yay energy range used in industrial applications. Therefore, for the energy range in this study of few tens keV to few MeV, X-ray interact with matter using three primary interactions. These are the photoelectric effect, Compton scattering and pair production.

Photoelectric effect occurs when a photon strikes out an inner shell electron from its orbit converting its energy in the release of electron. The emitted electron is termed a photo electron and it is released with kinetic energy equal to the energy of the incident photon minus the binding energy of the electron. An electron from a higher shell may fill the vacancy, which is accompanied by the emission of a characteristic X-ray, most likely for high Z material or by emission of an Auger electron, most likely for low Z material. The probability of photoelectric effect varies strongly with X-ray energy and the atomic number of the material. An approximate expression the photoelectric cross section $\sigma_{p.e}$ over energy E and atomic number Z of the material is given by

$$\sigma_{p.e} \approx \frac{Z^5}{E^{3.5}} \tag{1.1}$$

$\sigma_{p.e}$ E

Z Therefore photoelectric effect is dominant for high Z material but decreases strongly with the increase of energy.

Compton scattering takes place when a photon scatters off an outer shell electron. As a result, a photon of lower energy and a recoil electron are produced in this interaction. The energy of the scattered photon $E^{'}$ is given by:

$$E^{'} = \frac{E}{1 + \frac{E}{mc^2}(1 - \cos\theta)} \tag{1.2}$$

where E is the energy of the incident photon, mc^2 is the rest mass energy of the recoil electron and θ is the scattering angle of the photon.

The probability of a photon scattering at a given angle is illustrated in figure 1.2 (Klein-Nishina distribution) for various photon energies. It can be noted that probability of forward scattering increases with increasing energy.

The probability of Compton scattering is less dependent on energy and atomic number of the material compared to photoelectric effect, but is strongly dependent on the density of electrons in the medium.

Pair production results in the complete attenuation of the incident photon. Pair production can only occur if the incident photon energy is at least 1.022 MeV (sum of the rest mass energy of an electron and a positron). As the photon interacts with the strong

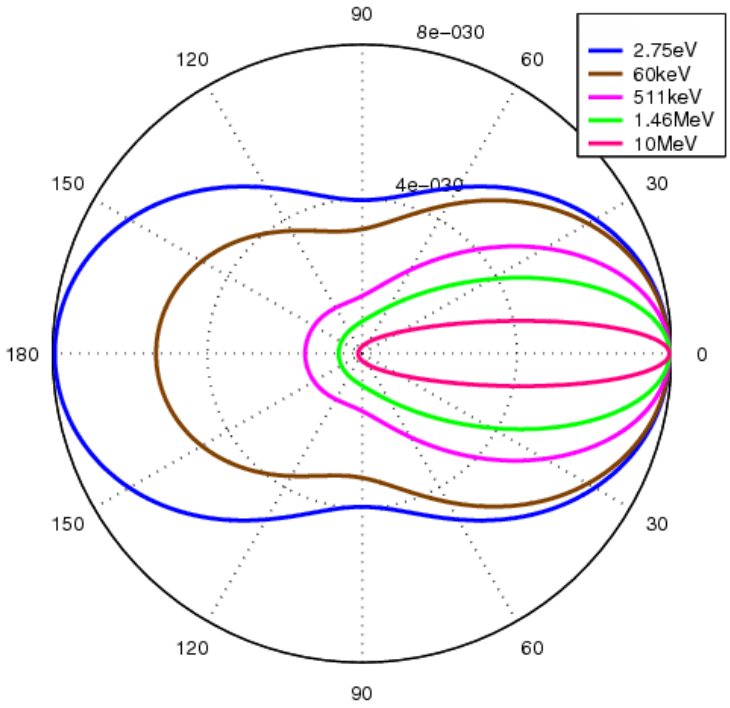

Figure 1.2: The polar graph shows the Klein-Nishina distribution of scattering-angle cross sections over commonly encountered energies [1]

electric field around the nucleus it undergoes a change of state and is transformed into two particles, an electron and a positron.

The relative importance of each of the interaction is illustrated in figure 1.3 in which the mass attenuation coefficient for aluminium is plotted as a function of photon energy. The probability of interaction of X-ray with matter, measured in terms of the attenuation coefficient, is strongly dependent on the atomic number Z and the density of the absorbing material, varying strongly with X-ray energy. As can be noticed in figure 1.3, in the industrial energy range, the most dominant interaction of X-ray with matter is Compton scattering for a common industrial material like aluminium. Therefore, the intensity reaching the detector has an important contribution from the Compton scattered photons. Thus, this energy range is usually accompanied by high scatter to primary ratio (SPR). The effect of this strong contribution of scatter intensity can create lot of reconstruction artifacts as described in detail in section 1.4.

1.2.2 Attenuation of X-ray

The interaction of X-ray with matter as described above causes the beam to attenuate as it passes through a material. The relation between the intensity of photons P that reaches the detector after an initial intensity I_o, passing through an object of thickness T is given by the Beer-Lamber law of attenuation as

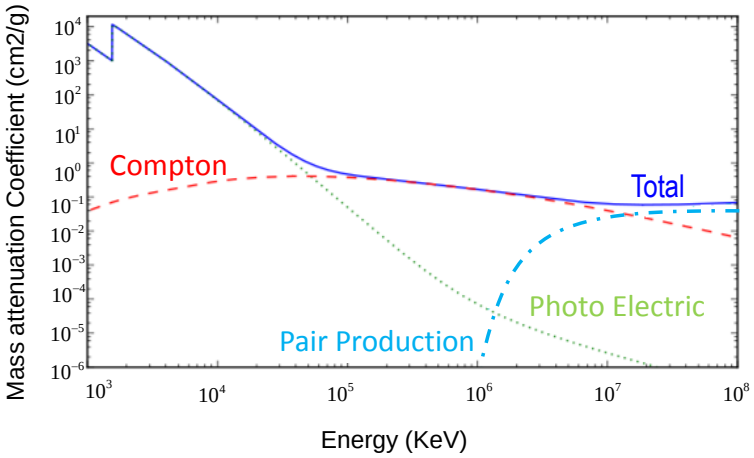

Figure 1.3: Mass attenuation coefficient variation over the photon energy for aluminium [2]

$$-\ln\left(\frac{P}{I_o}\right) = \int_T \mu(t)\mathrm{d}t \tag{1.3}$$

where μ is the linear attenuation coefficient given in per cm.

However, the above derived equation is valid only if all the photons are of same energy (monochromatic source). In reality, the X-ray spectrum contains photons of a wide range of energies. It should be noted that the attenuation coefficient of the material itself depends on the energy of photons, as described earlier. Therefore each X-ray energy is attenuated differently and the total attenuation is actually the sum of attenuation at all X-ray energies. This polychromatic nature of the spectrum itself becomes a source of artifact in CBCT also known as beam hardening artifact described, in detail in section 1.3.

1.2.3 CBCT 3D reconstruction

In this section, we want to briefly cover the 3D reconstruction stage of CBCT. The theory of CBCT reconstruction has been extensively studied in various texts and mathematical details can be found in these texts [8][9][10]. Here, we want to describe the underlying reconstruction process which forms the basis of reconstruction artifact due to scattering of photons, without discussing the mathematical details.

The 3D reconstruction task is to recover the linear attenuation coefficient μ of the object by using the set of 2D projections. Feldkamp, Davis, and Kress (FDK) algorithm [11], which is based on filtered back projection (FBP), is the most commonly used analytical reconstruction algorithm. It is built on the hypothesis that the monochromatic X-ray attenuation measured at the pixel of the detector is calculated as a line integral of the linear attenuation coefficient of the object over the straight line path (Radon transform). In reality, as mentioned previously, the X-ray source is polychromatic in

nature and as a result beam hardening artifacts (section 1.3) are formed. Moreover, secondary radiation is always present in the form of scattered photons that travel in random directions. Therefore, the violation of this straight line integrals hypothesis forms a source of scatter artifacts (section 1.4) leading to streaks, cupping effect etc on the reconstructed images. FBP, in general, needs a large number of projections to form a good quality image. Moreover, the FDK algorithm is formulated for 1D reconstruction in a fan beam geometry and is only an approximation for the cone beam reconstruction. A single circular geometry does not provide sufficient sampling for an exact cone beam reconstruction. Therefore, the algorithm performs reasonably well for small cone beam angles and is only exact in the source central plane. When the cone beam angle becomes large or similarly, if the object is long, shading and streaks artifacts can be produced (figure 1.4). The shape of the object reconstructed in the direction of the rotation axis, can also be distorted. Another approach based on iterative methods [12][13][14] has been developed to overcome some of the limitations of the analytical approach. Iterative approaches refine and modify the image iteratively in order to minimize a cost function which measures the fit of the image to the projection data. They are more realistic and can better model the physics of data acquisition. In addition, they can handle much noisier data, allow more flexibility in the scanning geometry, deal with incomplete or sparse data sets and can easily incorporate prior knowledge into the reconstruction process. The major drawback of iterative algorithms is that the reconstruction cannot be performed at the same time as data acquisition, as is instead possible in the case of analytical methods which can produce on the fly reconstruction.

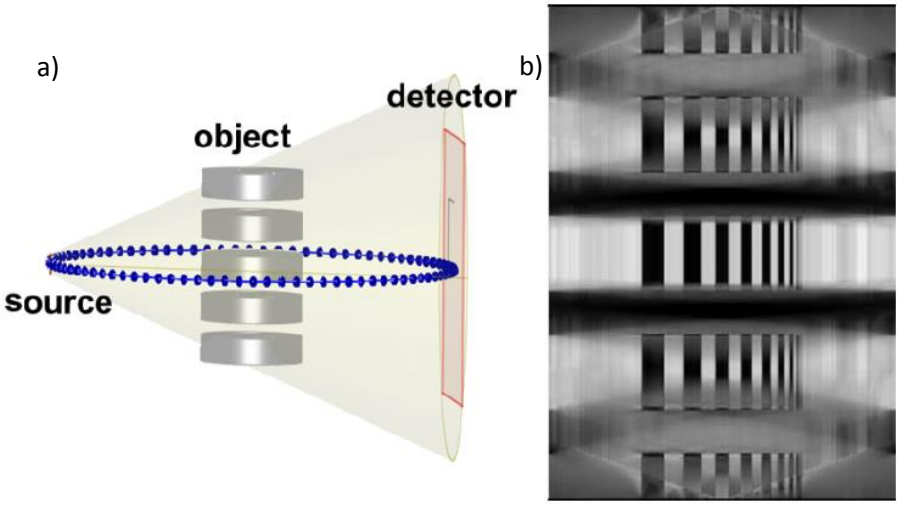

Figure 1.4: a) Acquisition setup geometry simulation in CIVA [3](NDT simulation software developed at CEA) with a multidisk object b) Vertical slice shows the artifact in the non central plane due to limitation of FDK algorithm [4]

1.3 Beam hardening effect in CBCT

As introduced in section 1.2.2, the polychromatic nature of the spectrum also forms an important source of artifacts in CBCT called beam hardening effect. Scatter and beam hardening artifacts usually both arise in CBCT reconstruction, and they can also form similar cupping artifact. In the following chapters, we have also integrated a beam hardening correction scheme into the scatter correction algorithm. Therefore it is important here to provide a brief description and review of the beam hardening effect and correction schemes. As a polychromatic beam of X-ray passes through matter, low energy photons are preferentially absorbed, causing the mean energy of the X-ray spectrum to increase [15]. The more material an X-ray beam penetrates, the more low energy photons are removed from the spectrum, which makes it increasingly difficult to further attenuate the beam. This means the X-ray beam becomes more penetrating, or "harder", at higher penetration depths, hence the term beam hardening. As a consequence of beam hardening, the outer edges of objects are reconstructed as being apparently more attenuating than those at higher penetration depths. This effect occurs because the first few millimeters of material rapidly attenuate lower energy photons from the incident spectrum, whilst, the material at higher penetration depths is irradiated by harder X-rays.

The most common and easily implemented method to correct the beam hardening is by the use of a filter [16][17]. A filter made of highly attenuating material (such as aluminium, copper, brass) is placed in between the source and the object. This causes the low energy photons to be absorbed before reaching the sample, so the beam is "pre-hardened". The main disadvantage of this method is that it reduces overall Signal-to-Noise Ratio (SNR) due to reduced overall photon flux. To compensate for this, the beam current needs to be increased in the system. In most cases a trade off between dose rate and filtering is found when there is limitation on the scanning time. Another important method to reduce the beam hardening effect is called linearisation method. This method aims at mapping the measured signals to signals one would measure in an ideal, monoenergetic case for the same path lengths. Therefore, a linear relationship between corrected signals and measured path lengths is restored. The mapping function can either be found experimentally [18] or by simulations with polychromatic spectra [19]. This is a pre-processing method which is applied before reconstruction and can be correct only for single material objects. This is because, for objects composed of multi-materials, measured projection integrals represent unknown mixtures of attenuation contributions from the different materials transverses by the beam. To overcome this problem of multi-material, another post-reconstruction approach has been developed based on iteration schemes during the forward projecting step of the reconstruction [20][21]. Another important method is the use of dual-energy approaches [22] to correct for beam hardening. This type of method requires two scans with two different X-ray voltages or an energy resolved detector.

1.4 Scatter artifacts in CBCT

As described previously, the reconstruction process in CBCT is based on the assumption of the X-ray that follow straight lines to reach the detector, in order to calculate the line integrals. However, in real conditions, the contribution of scattered photons mainly

due to Compton interaction which is dominant in the industrial energy range, violates this straight line assumption. Therefore the measured intensity at the detector pixel is the sum of scattered photons intensity plus the primary photons intensity (photons which did not undergo any attenuation or scattering) (figure 1.5).

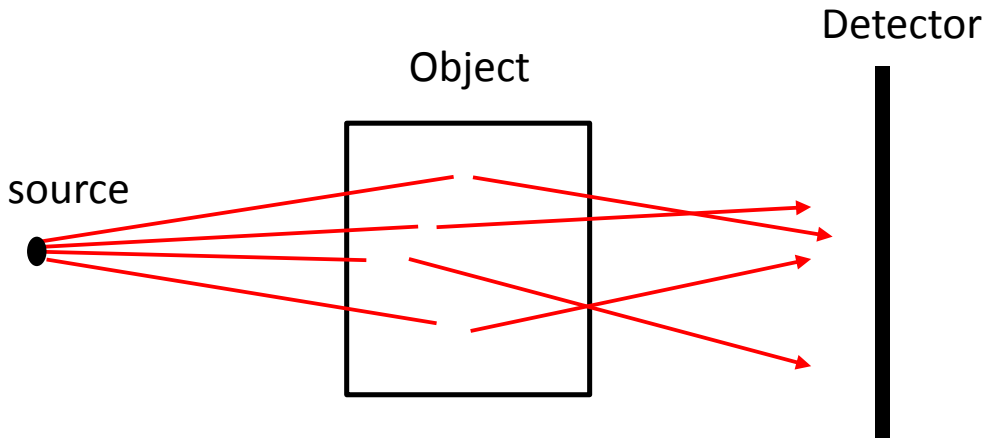

Figure 1.5: Illustration of scattered photons reaching the detector in the real conditions

These overestimated intensities in the voxels along the path correspond to an underestimation of absorption, i.e. in the attenuation coefficient of the reconstructed object. Since this effect is proportional to the amount of scattering present, is thus prominent in CBCT due to the large area of illumination on the 2D detectors. It causes various artifacts such as contrast reduction, streaks, cupping effect etc. Due to the severity of these artifacts, their correction is a very important aspect of both industrial and medical applications of CBCT.

1.4.1 Scattering due to the object

The scattering due to the object that finally reaches the detector is dependent on various factors, including the characteristics of the material: (1) atomic number Z, (2) thickness and (3) the distance between the object the detector also called air-gap. In the industrial energy range, as described above, Compton scattering is the dominant process, which increases with the decrease of the atomic number of the material. The scatter effect is found to increase with increasing thickness of the object. However, due to the decrease in primary transmission owing to more attenuation, it is expected to eventually reach a maximum and then start to decrease. This is due to the fact that the absorption of scattered photons accounts for a significant fraction of the scattered photons actually generated. The scatter fraction decreases with increasing air-gap between the object and the detector, due to decline in the scatter fluence, following the inverse square law. The decrease in the scatter fluence depends on its angular distribution which in turn depends on the energy. The lower is the energy of the beam, the broader will be the angular distribution of scatter and hence the detected

scatter fluence will be even lower. Moreover, the air-gap influences not only the relative magnitude of the scatter but also its spectrum. The mean energy of the scattered photons reaching the detector increases with increasing the air-gap. The lower energy scatter fluence has a broader angular spread and as a result with increasing the air-gap, there is a lower chance of lower energy scatter to reach the detector. Therefore, the overall spectrum of the scatter fluence moves towards higher energy with increasing the air-gap.

1.4.2 Scattering due to the detector

The majority of scatter correction techniques focus on scatter contribution from the object only. But recent studies [23][24][25] have proved that, in the high energy range used in industrial Non-Destructive Testing (NDT), the contribution of detector scatter also becomes important. While evaluating the role of detector in the reconstruction artifacts, a number of scattering and blurring processes within the detector need to be taken into account.

Firstly, X-ray radiation can be Compton scattered by any part of the detector surroundings such as mountings, back-plates or even the detector layer itself [23]. Bub et al [23] show that this scattering can also lead to the edge blurring of the object in the obtained projections. Another important effect at high X-ray energy is the backscattering of photons from the material behind the detector [26]. If the scintillator layer is made of a low absorbing material, a large part of radiation can be transmitted to the back-plate. For energies above K edge of the back-plate, there is appreciable increase in backscattering, due to the production of low energy fluorescence X-ray. These backscattered photons may be reabsorbed at a different site than the primary interaction site. As a result the overall spatial resolution of the detector decreases.

Additionally, when X-rays interact with a phosphor (mostly by photo-electric effect), X-ray fluorescence photons are produced which may be reabsorbed by detector areas adjacent to the primary X-ray interaction site. This may cause a loss of spatial resolution and an increase in image noise [27][28]. Moreover, the fluorescence optical photon may also scatter within the scintillator layer which causes blurring, also known as veiling glare [29][30]. Its magnitude mainly depends on the thickness and material characteristics of the detection layer.

1.5 Scatter correction techniques

Due to the severity of scatter artifacts on the reconstruction, a lot of attention has been given to correct this artifact over the years, in both medical and industrial fields. These methods can be broadly divided into two categories: Pre-processing and Post-Processing. In the pre-processing approaches, also called scatter rejection methods, scatter is corrected or removed before it reaches the detector and contributes in the intensities of the projections. This is achieved by changing the geometrical setup and often requires some extra hardware as described in detail in section 1.5.1. Conversely, in the post processing methods the scatter is corrected in the projections or in the reconstruction stage using some prior knowledge about the geometrical conditions,

object under study etc. The following sections describe these scatter correction methods in detail.

1.5.1 Pre-processing methods

Pre-processing methods are based on the incident angular distribution of the scatter process. The primary photons have slight divergent incident angle on the detector which is based on the X-ray focal spot whereas the scatter photons have comparatively random incident angles. It is, therefore possible to separate scattered and primary photons based on the distribution of their incident angles by modification of the geometrical setup. The chief advantage of these scatter rejection methods is that they can prevent the stochastic noise due to the scatter to reach the detector and hence can increase the Contrast-to-Noise ratio (CNR).

Anti-scatter grids

The first important method that uses this approach consists in introducing anti-scatter grids [31][32] in front of the detector. The anti-scatter grids are made of high Z material such as lead. This anti-scatter grid is made to focus with the X-ray spot so that the primary photons pass through the grid whereas the scattered photons are absorbed in the high Z material due to their random incident angles. The effectiveness of this approach have been studied in [33][34][35]. This approach does not lead to any magnification as there is no modification in the setup other than the insertion of grids. However, this approach is accompanied by many disadvantages. Most importantly, the grid attenuates the primary photons which contains useful information. For example, Wiegert et al. [36] showed that the SNR was degraded by the use of anti-scatter grid for head and thorax phantoms. To compensate for this loss, there is a need to increase the X-ray dose so as to maintain the same statistics. Moreover, this technique does not take into account scattering due to the detector itself which is an important additional source of scattering. There is a need of additional hardware and different grids with different properties may be required for each scan geometry depending on the energy of the source, which becomes important in terms of cost. Also as stated above, the grids need to be properly aligned well with the focal spot to maximize transmission of primary photons. Any misalignment can cause degradation in image quality. There is a reduction of efficiency of this method at higher energies due to increased transmission of scattered photons through the grids. Moreover, the improvement in CNR is limited by this method [37]. This is due to the fact, that because of the attenuation of primary intensity, the noise in the projections is increased. A thorough description on the characteristics of the anti-scatter grids can be found in Neitzel [37] and Wiegert et al. [36].

Air-Gap method

Another popular pre-processing scatter correction approach is the air-gap method [38][37][39]. Air-gap is defined as the distance between the imaged object and the detector. This method exploits the fact that scattered radiation originating from the

imaged object appears as a secondary X-ray source. As the air-gap between the object and the image receptor increases, the intensity of X-ray from the secondary X-ray source falls faster than the intensity of the primary beam reaching the detector due to the inverse square law. More scatter photons miss the detector as the air-gap increases, due to their unfocused incident angles as described in section 1.4.1. Sorenson et al. [39] showed that SPR can be reduced by a factor of 2 to 6 with respect to when no air-gap is introduced. The main advantage of air-gap is the ability to reduce SPR and to increase CNR at the same time as there is less reduction in primary intensities as compared to anti-scatter grids. The air-gap method also has an advantage of simplicity as no special algorithms or additional hardware is needed. It is more reliable, cheaper and does not require any additional physical element as is the case with grids. However, the method requires an increase of the distance from the imaged object to the detector, which is considered as unfeasible in many applications due to space limitation and safety regulations. Moreover, the projections are characterized by a defect of magnification which increases with increasing air-gaps. In applications that require high spatial resolution, increased air-gap also leads to image unsharpness due to the effect of the X-ray focal spot size also being magnified. Also, as pointed out earlier, higher energy photons are easily scattered in the forward direction so they have a greater chance of reaching the detector even after increasing the air-gap. Therefore, this method has a limited efficacy for the higher energy sources used in industrial CBCT.

Collimation of Field of View (FOV)

Because the SPR strongly depends on the size of field of view (FOV), limiting the FOV to a volume of interest (VOI) can significantly reduce the SPR. Smaller FOV can be simply achieved by collimating the beam along the CBCT rotation axis. Scatter rejection is further improved by limiting the FOV in the axial plane, known as the VOI scanning technique [40][41][42]. This technique typically relies on two CBCT scans. The first scan is a full field scan that serves as a guide to locate the relevant VOI. After the location of the VOI is determined, either the object is moved to align the VOI with the isocenter or the CBCT gantry is moved to align its isocenter with the VOI. The second scan covers the VOI only. To eliminate truncation artifacts in the reconstructed image, projections from both CBCT scans are combined, and composite projections are used for reconstruction. VOI techniques have two advantages in terms of achieving increased contrast sensitivity. First, the SPR can be significantly reduced, directly translating into an increase in the contrast sensitivity. Second, with the full view scan performed with lower exposures and the VOI scan performed with higher exposures, the image noise level may be reduced and the CNRs increased within the VOI. Lai et al. [43] investigated the application of the VOI scanning technique for medical CBCT, and they demonstrated that collimated scan of VOIs with several centimeters in size can decrease the SPR by an order of magnitude in the projection images of a breast phantom.

1.5.2 Post-processing methods

Pre-processing methods are limited in their efficacy as mentioned above and therefore are often accompanied with scatter correction by a post-processing approach. In the post-processing approach, the scatter effect is suppressed after its detection. A

prior knowledge of the setup, object, or scatter distribution is generally needed in advance. Once the scatter is estimated, it is subtracted from the scatter-contaminated projections, to obtain scatter free projections. 3D reconstruction using these corrected projections is then performed using standard reconstruction techniques. The main disadvantage of these methods is the lack of improvement in CNR. As mentioned, post-processing methods suppress the effect of scatter after the scatter intensity has reached the detector. Therefore, while scatter free-images are recovered however, the noise component due to scatter cannot be decoupled as is the case for pre-processing methods. They help to restore correct reconstruction values and the artifacts are reduced, but at the cost of image noise.

Measurement-based methods

One important method based on post-processing approach is called beam-stop method [44][6][45]. In this approach, a beam-stop object (often called as beam-stop array) usually a lead strip or a disc, is inserted in between the X-ray source and the imaged object, to obtain the scatter only measurement. The thickness of the beam-stop array is chosen with the primary assumption that most of the primary radiations are blocked by the beam-stop array and the final signal reaching the detector corresponds only to the scatter fluence. The scatter signal behind the shadow of the beam-stop array is interpolated based on a low frequency assumption for the scattering distribution. This type of approach can correct all sources of secondary radiations (object, environmental, detector) simultaneously. They do not depend on the scatter model for the estimation of scatter. However, the mechanics of the approach forms one of the major disadvantages. The system geometry changes with the insertion of beam-stop array, therefore, the measured signal does not match with the one without the beam-stop array. Therefore usually, a series of measurements with different beam-stops are needed to be carried out to obtain an optimal value. Moreover, a complete and accurate reconstruction of the object is not possible with a single scan. At least one extra scan is required to recover the missing primary signals. This is not desirable due to higher dose in medical CBCT and also an increased acquisition time. One way to reduce the number of redundant projections is to perform acquisition with widely sampled projection views and interpolating the scatter for the in between projections [46][47]. Another way is to move the beam-stop array in between the acquisition. The beam-stop array can be positioned at different places for different projections and thus the total image may be recovered by interpolation [48][49]. The beam-stop array method can also deliver problems at the edges of the object due imperfect estimation of scatter shape at the object edges, where the scatter image presents its largest gradient. In the cases where the scatter signal is composed of higher frequency components such as the ones due to scattering in the detector, a finer sampling of the arrays is needed to fully take into account the shape of the scatter.

An alternative to beam-stop methods to reduce the number of redundant projections, was proposed by Zhu et al [50] and Banihashemi et al [51] which employ slight modification of the X-ray hardware. They call this method as primary modulation, where a reference object (primary modulator) is placed in between the X-ray source and the object. The basic assumption about this method is that majority of scatter component in the total signal is composed of low frequency. The primary modulator is inserted with a known pattern of high frequency attenuation [52]. As a result, the primary distribution

is modulated by the same high-frequency function, while the scatter distribution still has dominant low frequency components, based on the hypothesis. Therefore, primary and scatter signals are strongly separated in the frequency domain. An accurate scatter estimate can then be obtained using filtering and demodulation techniques. Their method gave satisfactory results using a single scan and no extra dose. However, it is highly dependent on modulator design. Generally modulator with low transmission factor and high modulation frequency is preferred for better scatter correction. However it does not take into account beam hardening effect. Moreover, in the early-stage study of the primary modulation method, several non-ideal effects of a practical X-ray CBCT system are not fully considered, such as gantry vibration. These effects may degrade the scatter correction performance. Also, as pointed out in the earlier section, the scatter component coming due to the detector may contain high contribution in the overall scatter. This scatter generally is composed of higher frequency, therefore, prime assumption of scatter component containing only low frequency contribution may not be true in cases where detector scatter contribution is important.

Monte Carlo simulation based methods

Compared with measurement-based methods discussed above, MC calculations enable studying effects of underlying physical processes in more detail and thus evaluate a wider range of system parameters to characterize scattered radiation in CBCT [53][54][55][56][57][27]. This technique has the potential to remove the scatter contamination in the projections very accurately. However, direct use of MC calculations for object-specific scatter correction has not been considered until recent years due to the vast computational cost in simulating the photon interaction with the object on an event basis. Moreover, a very precise model of the object and setup are needed to be known in advance to carry out scatter correction with MC simulations. With the increasing computation speed and fast MC algorithms, MC calculations are increasingly considered for object-specific scatter corrections. Generally, MC-based scatter corrections are performed in CT image domain, that is, the scatter distributions are calculated by forward projecting the CBCT image of the object itself [58][59][60]. Such calculations offer potentially the most accurate software-based scatter corrections, but the challenge lies in performing MC calculations in an acceptable time frame. To accelerate MC calculations of scatter projections, variance reduction techniques have been implemented improving computation speed by several orders of magnitude [61][62]. In addition to variance reduction, use of graphics processing units (GPUs) enabled improved parallelization of MC calculations, and significant gains in computation speeds have been reported. Badal and Badano [63] reported that calculation of projections from CT image sets was more than an order of magnitude faster with GPUs, compared with calculations based on single central processing unit (CPU). Jia et al. [64] calculated a single forward projection in less than 2 min using GPU acceleration with image quality comparable to a digitally reconstructed radiograph. The MC methods are also usually used together with methods based on deterministic models to improve the scatter estimation accuracy. For example, Hansen et al. [65] proposed a method of generating scatter kernels methods (described below) using MC simulations.

Scatter Kernel Superposition (SKS) method

One of the most important scatter model based method is called Scatter Kernel Superposition (SKS) [65][66][67][5][68]. This method does not effect the X-ray system and correct the scatter from the obtained projections according to the system geometry and object information. The accuracy of this method depends on the accuracy of the scatter model used. The key element of a SKS method is the scatter kernel, which can be, thought as a transfer function that relates primary fluence at a point within the object to its corresponding scatter intensity distribution in the detector plane. The total scatter distribution is then calculated using the superposition of these scatter intensity at each point. This method requires a prior knowledge about the physical properties of the object. SKS methods are implemented in projection image domain. The scatter kernel is obtained for a pencil beam that transverses the slabs of uniform thickness of the same material as the object under study, and falls on the detector. A simplified deterministic relationship between the scatter distribution and the primary distribution is then obtained. Typically, the scatter distribution is approximated as the convolution of the primary distribution with the pencil beam scatter kernels. This is an inverse problem where true primary estimate is determined using the technique of deconvolution.

If the kernels are assumed rotationally symmetric and stationary, then the computation cost of these techniques are even lower as the convolution can be performed in the Fourier domain. However, the stationary kernel assumption generally gives over simplified estimation of the scatter distribution, which, in reality can be of complicated nature depending on the complex geometry of the object under study. A way to address this problem is to decompose the kernels as a multiplication of a weighting term proportional to the total scatter intensity and a shape term which addresses the shape of the scatter distribution. Initially non stationary kernels were implemented for specific known objects [69][70]. First non-stationary implementation was performed by Naimuddin et al. [71] where they used look up tables to calculate the weighting function for the kernels. Kruger et al. [72] proposed regionally variable pencil beam scatter kernels for different anatomic region. Another way to address this problem of object geometry dependency of the scatter distribution is to parameterise the weighing function and shape function in terms of thickness. Free parameters can be empirically fitted according to the object thickness and the shape function can be still kept stationary. The shape of shape function of the kernel, generally used at keV energy, has long tails that deviate from single Gaussian distribution. Sun et al. [5] and Meyer et al. [73] use double Gaussian model to take into account long shapes of the kernels. Sun et al. [5] let free parameters vary in terms of the object thickness, however the scatter correction method is based on a course sampling of the scatter kernels in terms of thickness. Their method is originally developed for diagnostic energy range using only water-like objects where the SPR is comparatively lower than what is experienced in the industrial energy range. This discrete sampling of kernels may have short coming when applied to industrial data due strong variation in kernel's shape and amplitude with respect to the thickness of the object. Maltz et al. [67] stored precalculated kernels in a database that were indexed as a function of water equivalent thickness, object size, and imaging geometry. This approach may be computationally less efficient but, in contrast, it also avoids issues related to inaccurate kernel parameterisation and can potentially accommodate nonstationary kernel shapes.

Scatter kernels can be obtained both using experimental methods and simulations each of them having their own advantage and disadvantages. There are many SKS techniques based on calculation of kernels using MC simulations [65][66][5][74][75]. In MC calculations, kernels are generated by simulating a pencil-ray beam incident on slabs and registering scatter distribution in the detector plane. Compared with experimental methods, MC calculation gives more flexibility for generation of kernels. They can be obtained for any arbitrary object shape and imaging geometry with relative ease. The object scatter kernel modeling is usually proposed using two-Gaussian model as in [5][76][77]. However most of these methods do not take into account a realistic modeling of the flat panel detector leading to the calculation of only object scatter kernels. To tackle this issue, the use of experimentally calculated kernels [78][25][56] makes it possible to correct the scatter contributions due to both the object and the detector, without having to rely on an accurate 3D modeling of the detector. Kernels are usually derived from measurements using the slanted-edge method to compute the edge spread function (ESF) response. In these techniques, the scattered radiation is approximated by pencil-beam kernels with purely experimental [78] or analytically-fitted [25][56] models. Their results demonstrate that the contribution of scatter glare in the detector is important, the long-tails creating a MTF drop in the low-frequency domain. Those analytical kernels involve a single exponential [25] or Lorentzian [56] model, the use of multiple terms in fitting the kernels being reported subject to instabilities for high-frequency components [56]. A single term in the analytical kernel model is however not able to discriminate the scatter contributions. Two-Gaussian initialization of the detector scatter kernel has been proposed by [5] but in a post-processing step taken outside the iterative SKS deconvolution. This approach might not be sufficient, notably, to taken into account the hardening of the beam spectrum.

As discussed above, modifications and flexibility have been studied in the SKS method to overcome the major drawback of the dependency on the object geometry. Nonetheless, the advantages of this technique of not requiring any additional hardware, scanning time or additional dose and independence over the object motion make this technique ideal method in various medical and industrial applications. Currently, this method offers the best compromise between computation speed and scatter correction accuracy.

Image processing methods

The methods discussed so far use physics based approach. Another way to handle the scatter artifact could by the use of post reconstruction image processing tools [79][80][81]. Their performance mainly depends on the visibility and easy detection of scatter artifact in the reconstruction. Generally the detection of degradation in reconstruction values is non trivial and thus the artifacts may not be fully corrected.

1.6 Motivation and aim of the study

Different types of scatter rejection and correction methods in CBCT imaging were reviewed in this chapter. The scatter rejection methods help in reducing the scatter

artifact from the reconstructed images. At the same time they help to improve overall CNR by reducing the scatter intensity from reaching the detector. Anti-scatter grids are useful in improving scatter artifact but the attenuation of the primary intensity reduces the SNR and degrades the image quality. The air-gap method is comparatively simpler to implement and both artifact reduction and improved CNR is achieved. However, it has a limited efficiency and an increased unsharpness due to magnification. Collimating the FOV to the application area can greatly improve SPR and CNR in that region but it only works in the volume of interest.

Scatter correction methods as compared to scatter rejection method have better efficiency in reducing the scatter artifact from the images but without any improvement in CNR. Measurement-based methods like beam-stop array are not computationally demanding and can address the scatter due to various sources all together. However, this method generally requires acquisition of redundant projections and thus, may lead to increased acquisition time and dose. Moreover, development of special beam-stop array in each case is a challenging task. Measurement-methods based on primary modulation do not usually require acquisition of redundant projections. But their efficiency is highly dependent on the modular designing. MC simulation based methods are potentially very accurate if object and setup description are very well known in advance but computationally very expensive even with accompanying time reducing algorithm. Post-reconstruction image processing approach can provide a fast correction of scatter artifact. They may not require measurement and calibration procedures. However, they are applicable to only specific imaging task and true reconstruction values may not be recovered.

It is evident that scatter correction using SKS approach currently bring together best compromise between robust scatter correction and computational speed. They are applicable over a wide range of imaging conditions. No need of any extra hardware form a major advantage of this approach specially in the cases where experimental complexities are needed to be avoided. Thus post-processing scatter correction approach over formerly acquired data with classical acquisition can be applied using this method. They do not impose requirement of building complicated hardware as in the case of measurement-based methods. They are computationally very effective as compared to MC approach making them a practical scatter correction method. Moreover, they do not require any additional dose or scanning time, which is important in the medical imaging field.

The only major disadvantage of using the SKS scatter correction method is that they may not fully take into account the variation of scatter due to object shape and thickness as well as spatial distribution of the heterogeneity in the object. As mentioned in section 1.5.2, several modifications have been adopted in the field of SKS method to take into account the variation of object shape for calculating scatter distribution. However, several questions still need to be answered in these modifications for considering the correction in industrial energy range which is the scope of this study. In the industrial energy range the SPR is very high compared to medical energy range. With this high value of SPR, the variation of shape and amplitude of the kernels is very high with respect to the thickness of the object. As mentioned in section 1.5.2, among many modifications produced in SKS method, one of the approach is to parameterise the kernels in terms of thickness as proposed by Sun et al. [5]. In the parameterisation approach of the kernels, a discrete set of thickness-dependent kernels are used and for a range of thickness only one kernel is used. This method gives satisfactory results in

many applications including the medical application where originally this method was tested. However, for higher SPR, the different steps of the SKS correction algorithm have to be reconsidered. In particular a better sampling of the kernels with respect to the thickness of the object is required to get an accurate model of variability in shape and in amplitude of the scatter kernels over the whole thickness range. Moreover, the scatter level is not negligible due to higher SPR with respect to the primary radiations. Therefore, the robustness and the convergence of the iterative correction scheme become critical since a slight overestimation of the scatter radiation level might lead to large negative values of the primary transmittance. The iteration scheme adopted in the original method is based on subtraction of scatter from the measured projections. This type of scheme may not be suitable in the energy range of this study as the scatter distribution may be overestimated at any iteration step leading to negative primary estimates.

Therefore, the next chapter of this study describes a proposition to tackle these issues of high SPR in higher energy case. We propose an empirical fitting of the scatter kernel parameters which are derived in terms of object thickness to form continuously thickness-adapted kernel map [75]. This approach has the ability to better sample the kernels with respect to thickness of the object. The scatter corrections are performed using this approach and the results obtained are compared with the classical approach. The object and material used are typical materials used in industrial applications, like iron and aluminium. Moreover, a multiplicative iteration approach is implemented to tackle the problem of negative estimates of primary within the iteration process. Another important aspect of this chapter is to study the proposed method over multi-material object. Since in the energy range used, the dominant process of interaction is Compton scattering, therefore, the probability of interaction is independent of the atomic number of material. This property is exploited in this study to test the validation of the proposed approach over multi-material objects.

Another very important aspect of this study is to investigate the contribution of the scattering of detector. As mentioned in section 1.4.2, recent studies have shown contribution of the detector scattering becomes very important specially in the case of higher energy source with the scatter intensities coming from various parts of the detector. X-ray fluorescence and optical glare can also contribute in reducing the spatial resolution. Most of the scatter correction studies either only correct the scatter due to the object [65][66] or individual study of the detector scatter [25] contribution have been made using SKS approach. Sun et al. [5] proposed to account for the detector scatter during the initialization with two-Gaussian terms, but this preprocessing-step prior to the iterative SKS deconvolution might not be sufficient either to accurately model the detector kernel variability with respect to the object thickness, notably to take into account the hardening of the beam spectrum.

In the third chapter of this study, we propose to evaluate the contribution of detector scattering at NDT energy range using continuously thickness adapted SKS method [75]. A separable model using the continuous approach described in chapter two is proposed to separate the scatter due to the detector and the object. The continuous method and other classical SKS method [5] use a two-Gaussian model for the fitting of kernels. This two-Gaussian parametrization of kernels has several shortcomings. Firstly, the scatter contributions from the detector and the object are entangled, which makes the parameter fitting of the continuous model tricky. Moreover, we noticed that the high frequency contribution of the detector scatter generates a strong peak in the

center pixel of the detector where the pencil beam is impinged. This shape calls for the necessity to explore an increase in order of the Gaussian model. Therefore, we propose in this chapter, by means of both experiments and simulations, to identify the respective scatter contributions of the object and detector using a four-Gaussian model to have a more stable modeling. In this chapter, we also extended our method to be used at MeV energy range. Results obtained with the acquisition performed at 6 MeV source are also presented in the chapter.

So far the scatter correction performed in this study is based on the calculation of the kernels using MC simulations. In the realistic case, efficiency of this approach is dependent on the accuracy in the simulation of the real conditions, especially in the case of 3D modeling of the detector. The constituents of the detector are generally kept anonymous from the manufacturers to the users. Therefore modeling of accurate detector parts is difficult using MC simulations. Thus, generation of kernels using experimental approach can solve this issue.

The fourth chapter of this study presents the validation of the continuously-thickness adapted kernels approach using generation of kernels by experimental techniques. The same four-Gaussian model is used to separate the contribution of object and detector scatter. This chapter also includes a parameterisation scheme of the kernels with respect to magnification of the setup. Using this technique, only one set of kernels for a particular magnification are sufficient to recover scatter corrected projections acquired at different magnification geometry.

Therefore, the main aim of this study is to develop a scatter correction scheme which is flexible and adaptable to many different users working in different conditions. The objective is to produce a scatter correction technique capable of correcting scatter over-wide range of energies, as it has been tested in this study. To be able to correct scatter with object made of complex geometries and more than one material. To be able to perform scatter correction using MC simulations if they are handy to the user or to perform simple experiments to calculate the scatter kernels. The experiment acquisitions, for the scatter kernels, performed at one setup geometry for a given material, be able to apply for the scatter correction of other geometrical setup. With this aim in the mind, we begin the next to describe the main method of continuously-thickness adapted kernels.

Chapter 2

Scatter correction using continuously thickness-adapted kernels

This chapter is based on the publication, Bhatia et al. "Scattering correction using continoulsy thickness-adapted kernels" NDT& E International 78 (2016) 52-60

This chapter begins with the description of classical scatter correction scheme by SKS method (2.2) [65][66][67][5] in which the scatter signal is modeled as the sum of the scatter contributions from a group of pencil beams passing through the object and the detector. Section 2.3 of this chapter describes the idea of scatter correction using continuously thickness-adapted kernels [75] to tackle the variation of amplitude and shape of kernels by empirically fitting the parameters of the scatter kernels in terms of material thickness. Section 2.4 describes the modeling of kernels for multi-material objects using equivalent thickness scheme. Section 2.5 shows the generation of kernels using MC simulations and fitting of kernels with non-linear least square approach. Section 2.6 describes the iterative scatter correction process by multiplicative approach to ensure positive estimates of primary intensity. Section 2.7 illustrates the materials used in this study. Section 2.8 outlines the results obtained for the validation of the continuous approach for both homogeneous and heterogeneous objects.

Summary

2.1 Introduction

This chapter focuses on twofold modification of the classical discrete parameterisation approach of scatter correction by SKS method [5]. In this method scatter signal is modeled as the sum of the scatter contributions from a group of pencil beams passing through the object. It approximates the scatter distribution, as the convolution of primary signal with the scatter kernels. Pencil beam kernels are thickness dependent kernels and there is an appreciable change in the amplitude and shape of these kernels with respect to small variation in the thickness of the object. The classical scatter correction method is based on a discrete set of thickness-dependent kernels and for a range of thickness only one kernel is used. This method gives satisfactory results in many applications. However, when a high range is considered (typically [300,500] keV), the SPR is expected to be very large and this discrete description of kernels can be a source of artifact itself as the shape of the kernels is strongly dependent on the object thickness. Therefore different steps of the SKS correction algorithm have to be reconsidered. In particular a better sampling of the kernels with respect to the thickness of the object is required to get an accurate model of variability in shape and in amplitude of the scatter kernels over the whole thickness range. In this chapter we propose empirical fitting of the parameters of the scatter kernel, derived in terms of material thickness to produce a better sampling of kernels over the whole thickness range of the object. We call this method scatter correction using continuously thickness-adapted kernels [75] or simply continuous approach for future reference.

Another modification in this chapter is based on the fact that when the scatter level is not negligible with respect to the primary radiations as in the case of high SPR at the energy range used, the robustness and the convergence of the iterative correction scheme becomes critical since a slight overestimation of the scatter radiation level might lead to large negative values of the primary transmittance. To tackle this issue we propose the use of multiplicative iteration scheme which ensures positive primary estimates throughout the iteration process.

A further additional aspect of this chapter is to study the proposed continuous method for the multi-material case. At the energy range used, the dominant process of interaction is Compton scattering. Therefore the probability of interaction is independent of the atomic number of material but only depends on its electron density. This property is exploited for the modeling of multi-material objects as the kernels of equivalent thickness of single material can be used for a heterogeneous object.

The outline of this chapter includes the description of the methodology of scatter correction with pencil beam kernels. This is followed by the description of development of the analytic expression for continuous kernel map. The modeling and generation of kernels is described in depth. Subsequently, the modeling of the kernels for heterogeneous object is explained in detail. We then describe the iterative scheme followed for the scatter correction in the obtained projections. Afterwards, the acquisition set up and objects used are described. Finally the results obtained after the reconstruction performed using FDK algorithm [11] are compared for discrete set of kernels and continuous map of kernels for homogeneous and heterogeneous object.

2.2 Scatter correction by Scatter Kernel Superposition

The measured signal at the detector $I(m,n)$ has two components: $P(m,n)$ is the primary signal contributed by the photons passing directly without any attenuation or scattering and $S(m,n)$ is the signal contribution of the scattered photons from the object and the detector. Therefore, the measured signal is given by:

$$I(m,n) = P(m,n) + S(m,n) \tag{2.1}$$

I where m and n correspond to the pixel position on the detector.

The scatter signal can be modeled as the sum of the scatter contributions from a group of pencil beams passing through the object and the detector. For each pencil beam input, a resulting kernel which has the weight of the scatter to primary ratio is determined. The total scatter signal $S(m,n)$ can then be modeled as:

$$S(m,n) = \sum_k \sum_l P(k,l) K_{T(k,l)}(m-k, n-l) \tag{2.2}$$

where,

K_T is the thickness (T) dependent kernel, with amplitude equal to the ratio of the scattered signal at the current pixel to the primary signal, at the pencil beam centered pixel. The sum in the convolution process runs over all pixels (k,l) of the detector The thickness is calculated with the Beer Lambert law

$$T(k,l) \approx \frac{1}{\mu} \ln \frac{I_o(k,l)}{P(k,l)} \tag{2.3}$$

with μ being the attenuation constant of the object under consideration at the mean energy of the spectrum used. The pencil beam kernel K_T can be fitted into the equation formed by an amplitude factor $C(k,l)$ (which is a function of the primary signal $P(m,n)$ and the un-attenuated air intensity $I_o(m,n)$ and a form-function $G(m-k, n-l)$ consisting of two circularly symmetric Gaussian functions describing the shape of the kernel [5]:

$$K_T(m-k, n-l) = C(k,l) G(m-k, n-l) \tag{2.4}$$

$$C(k,l) = \left(\frac{P(k,l)}{I_o(k,l)} \right)^{\alpha} \ln \left(\frac{I_o(k,l)}{P(k,l)} \right)^{\beta} \tag{2.5}$$

$$\begin{aligned} G(m-k, n-l) = A \exp \left(- \frac{(m-k)^2 + (n-l)^2}{2\sigma_1^2} \right) \\ + B \exp \left(- \frac{(m-k)^2 + (n-l)^2}{2\sigma_2^2} \right) \end{aligned} \tag{2.6}$$

Equation 2.2 then becomes

$$S(m,n) = \sum_k \sum_l P(k,l)C(k,l)G(m-k,n-l) \tag{2.7}$$

2.3 Scatter correction using continuously thickness adapted kernels

In the discrete kernel approach, a few thickness ranges are selected from zero to maximum thickness of the object and a single average value for fitting parameters $\alpha, \beta, A, B, \sigma_1, \sigma_2$ is obtained for one particular thickness range. The superposition convolution equation is thus modified to the form

$$S(m,n) = \sum_t \sum_k \sum_l P(k,l)R_t(k,l)C_t(k,l)G_t(m-k)(n-l) \tag{2.8}$$

$$R_t(k,l) = \begin{cases} 1, & \text{if } T_t(k,l) \leq T(k,l) < T_{t+1}(k,l) \\ 0, & \text{otherwise} \end{cases} \tag{2.9}$$

where t gives the number of thickness groups and T_t and T_{t+1} are the lower and upper bound thicknesses of the t^{th} group.

In the continuous approach, the fitting parameters are also interpolated with respect to thicknesses to form a continuously varying profile of kernels. Hence equation 2.8 is modified to :

$$S(m,n) = \sum_k \sum_l P(k,l)C(k,l,T(k,l))G(m-k,n-l,T(k,l)) \tag{2.10}$$

2.4 Modeling for heterogeneous objects

When dealing with heterogeneous samples, the thickness map $T(k,l)$ computed from equation 2.3 gives an estimate of the kernel-material equivalent thickness, that sometimes is called WET (water-equivalent thickness) when water is used to compute the kernels [67]. Within the energy range used, Compton scattering is the most dominant interaction process. The likelihood of interaction is proportional to electron density and is independent of the atomic number of the material. Therefore equivalent thickness (T_A) of one material A, for a given thickness (T_B) of material B, can be calculated in terms of their electron density functions using the following relationship:

$$T_A \cdot \rho_{e,A} = T_B \cdot \rho_{e,B} \tag{2.11}$$

where $\rho_{e,A}$ and $\rho_{e,B}$ is the electron density for material A and B respectively. Given γ be the ratio between these densities, we have

$$\gamma = \frac{\rho_{e,A}}{\rho_{e,B}} = \frac{\rho_A Z_A A_B}{\rho_B Z_B A_A} \tag{2.12}$$

where ρ is the mass density, Z is the atomic number and A is mass number. Using Equation 2.11 and 2.12 we get

$$T_B = \gamma T_A \tag{2.13}$$

This property can be exploited for the scatter correction of heterogeneous objects. As the kernels for a particular thickness of a material do not depend on the atomic number of the material but only on its electron density. Therefore, the scatter kernels of single material can be used for the scatter correction of heterogeneous objects.

2.5 Generation and fitting of kernels

Monte Carlo (MC) simulations were performed in the CT module of CIVA software [3] for the generation of kernels. Developed by CEA LIST, CT module of CIVA combines deterministic and MC approach for the generation of primary and secondary radiation in tomography [82].

For the simulation of the kernels, imaging geometry corresponding to the acquisition setup was modeled in CIVA. Pencil beam source was impinged on slabs of same material as the object under study and discrete set of point spread 2D kernels were obtained on the flat panel detector. Equation 2.4 was fit on these kernels using non-linear least square fitting and the values for parameters $\alpha, \beta, A, B, \sigma_1, \sigma_2$ were calculated for these discrete sets of kernels.

To obtain the continuous kernel map, we calculated the expression for the parameters $\alpha, \beta, A, B, \sigma_1, \sigma_2$ in terms of the thickness of the object. To obtain these expressions, the values of the parameters obtained for discrete set of kernels were fitted with respect to the thickness using non linear least square curve fitting technique. The fitted models for the kernels parameters with respect to the material thickness are polynomials and Morse potential functions, with different constrain on the degrees of freedom for some. The two point-spread functions (PSF) in equation 2.6 are defined by standard deviations σ_1 and σ_2. These two PSF are representative of scattering of object and detector

1. σ_1 defines the higher order scattering from the object which is expected to increase with increasing the thickness of the object
2. σ_2 defines the first order scattering dominated from the detector and is expected to be a constant with varying of the thickness of the object.

2.6 Iterative scatter correction

At high energies, the combined scatter of the object and the detector can be much higher than the true primary itself due to high SPR. In such case when a simple additive iteration approach is applied (equation 2.14) to calculate the new primary estimate, negative values of the primary estimate can be obtained due to overestimation of scatter.

$$P^{i+1}(m,n) = P^{i}(m,n) + \lambda(S^{i}(m,n) - S^{i+1}(m,n)) \tag{2.14}$$

λ represents the relaxation parameter. It is difficult in the first place to estimate the value of λ that ensures positive primary estimate. Moreover, even if a suitable λ value is chosen to ensure the first scatter estimate to be lower than the measured signal, this type of iteration scheme gives no guarantee that the primary estimate will be positive at every iteration step.

Therefore we adopt a multiplicative iteration scheme given by equation 2.15 which ensures positive primary values.

The iterative scatter correction scheme consists of the following steps:

1. The measured projection is taken as the first estimate of the primary.
2. Equivalent thickness is calculated for each pixel by using equation 2.3.
3. Pixel wise convolution is performed by choosing the suitable kernel for the respective thicknesses.
4. Scatter is estimated either using equation 2.8 for the discrete approach or by using equation 2.10 for the continuous approach.
5. The primary estimate is updated using

$$P^{i+1}(m,n) = P^{0}(m,n) \times \frac{P^{i}(m,n)}{P^{i}(m,n) + S^{i}(m,n)} \tag{2.15}$$

Steps 1 to 5 are repeated until convergence is achieved.

The schematic representation of the projection wise scatter correction process by discrete method is shown in figure 2.1. Another important point to be noticed in the discrete approach as clear in schematic in figure 2.1 is that the detector scattering contribution is calculated outside the iteration process. The detector scatter is calculated with a single PSF of the detector. This approach may not be suitable in all cases specially when the detector scattering depends on the beam input on the detector as we will see in the coming chapters. The kernels are then simulated with a simple model of the detector consisting of only detection layer such as CSI.

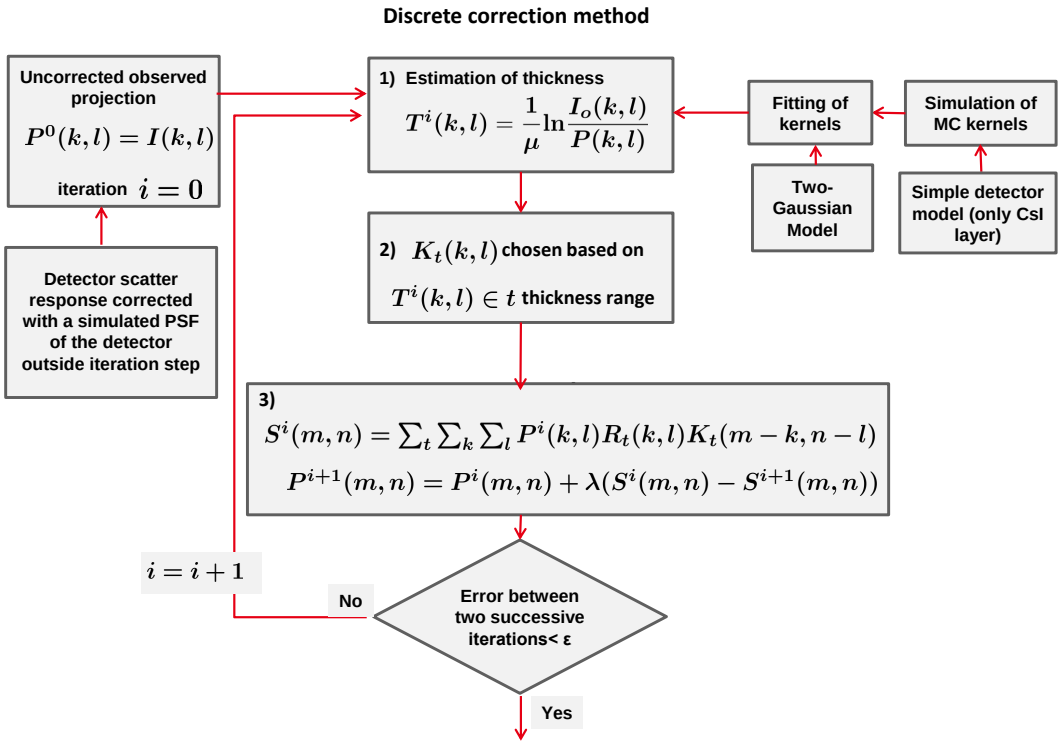

Figure 2.1: Schematic representation of the projection wise scatter correction process by discrete method by Sun et al.[5]

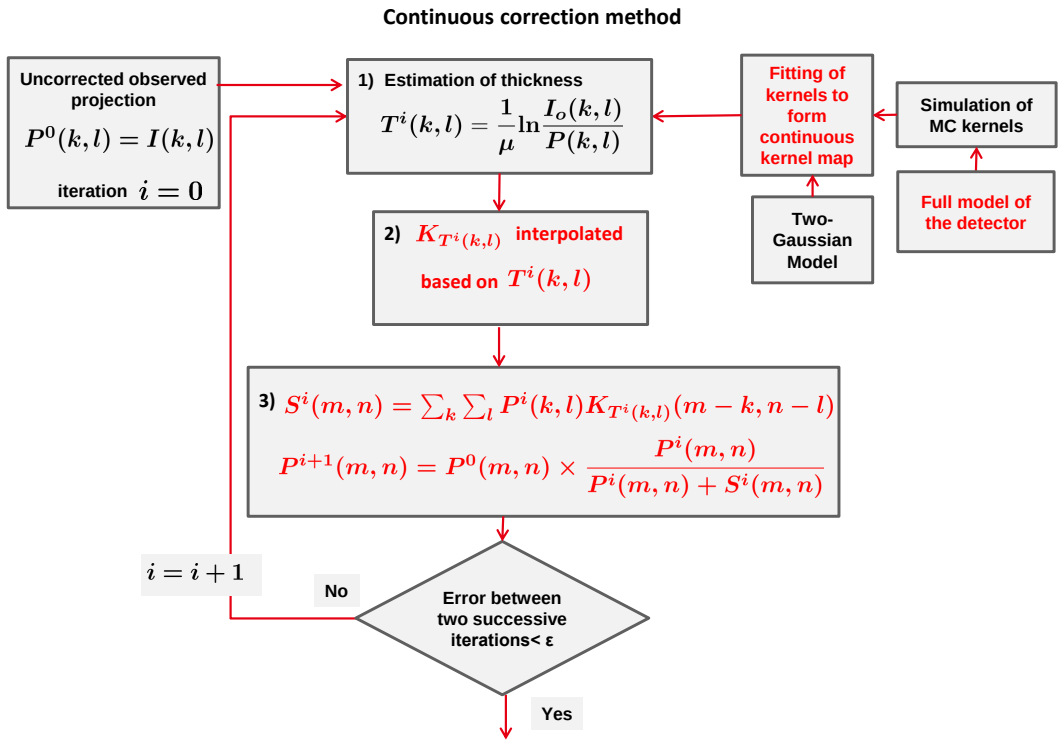

Figure 2.2: Schematic representation of the projection wise scatter correction process by continuous method. The modifications with respect to discrete corrections are shown in red.

We compare this schematic of discrete correction with the schematic of continuous correction as shown in figure 2.2. The modifications with respect to the discrete method are shown in red. In the continuous model we have taken the full model of the detector within the iteration step to simulate the kernels as opposed to the discrete model.

2.7 Materials

2.7.1 Validation on homogeneous object

For the acquisition setup, the source to detector distance was kept 371 cm and the distance between source and axis of rotation was kept at 353 cm. The setup mainly consisted of an X-ray source, an object rotational table and a flat panel detector.

The X-ray source unit used was a 400 kV X-ray generator manufactured by Philips (model MG450). The maximum tube current was 15 mA. Two focal spot sizes were available: 1.5 mm and 4.5 mm and angle of the target, made of tungsten, was 26°. A filtration of 4 mm of Pb + 1 mm of Cd was used in order to reasonably remove the beam hardening effect. With this filtration the total number of the X-ray photons with energy less than 200 keV represented the 4% of the X-ray beam spectrum while it was 92% without filtration [6].

The flat panel detector called FlashScan 33 developed by Thales Electron Devices consisted of Gadolinium Oxysulfide(Tb) scintillator screen for the X-ray conversion. The detector was based on amorphous silicon TFTs array and was designed to work on a wide kV range (from 25 keV to few MeV). The active area consisted of 2240 × 3200 pixels of 127 µm size [6].

Acquisitions were performed on an iron hub sample as given in figure 2.3. The sample is 32 mm in height and 52 mm in the external diameter.

Figure 2.3: Picture of sample of the iron hub [6]

2.7.2 Validation on heterogeneous object

In order to check the feasibility of the algorithm for heterogeneous objects, projections were simulated in CIVA for an object, consisting of a 60 mm diameter cylinder of aluminium containing a 20 mm diameter cylinder of iron inspected at 450 keV

monochromatic source and a flat panel detector of 750 × 750 pixels with 220 µm size. figure 2.4 shows the setup of the object.

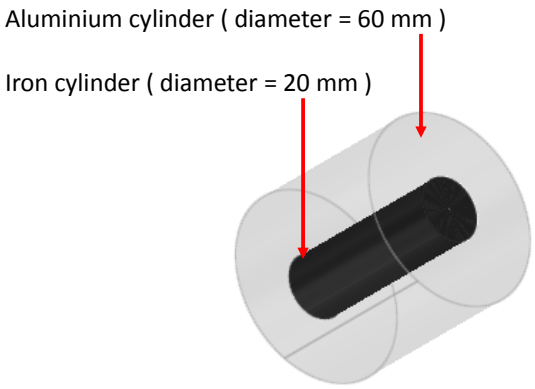

Figure 2.4: Setup of heterogeneous object consisting of a 60 mm diameter cylinder of aluminium containing a 20 mm diameter cylinder of iron

2.8 Results

2.8.1 Empirical fitting of kernels for continuous kernel map

Figure 2.5 (a) shows the 1D profile of the kernels obtained by MC simulation in CIVA and 2.5 (b) shows the kernels normalised to the maximum value of the detector kernel (0 mm thickness).

The fitting of parameters $\alpha, \beta, A, B, \sigma_1, \sigma_2$ with respect to thickness using least square fitting is shown in figure 2.6. The SPR first decreases and then increases for thicknesses above 20 mm due to higher attenuation of primary as seen in figure 2.5 (a). Figure 2.5 (b), however, clearly shows that with increasing the thickness of the object the higher order scattering increases and broadens the shape of the kernels. Parameters A and B, which are representing the amplitude of the shape of the kernels, first decrease up to a thickness of 20 mm and slowly increase beyond 20 mm. For fitting this, we used Morse potential energy function. Parameter α which is dependent on the attenuation, increases linearly with the thickness. Following the same argument parameter β, on the other hand, decreases with increasing the thickness. As mentioned in section 2.5, σ_2 defining the scattering from the detector remains a constant with varying material thickness and σ_1 defining the higher order scattering from the object increases along with the thickness of the object. The relative absolute error with respect to thickness between CIVA 2D kernels and fitted models is between $6 - 8\%$ as shown in figure 2.8a).

(a) **(b)**

Figure 2.5: (a) Plot profile of the simulated kernels using MC simulation in CIVA for different aluminium slab thickness (b) Plot profile of the simulated kernels normalised to the maximum value of kernel for detector kernel (0 mm thickness)

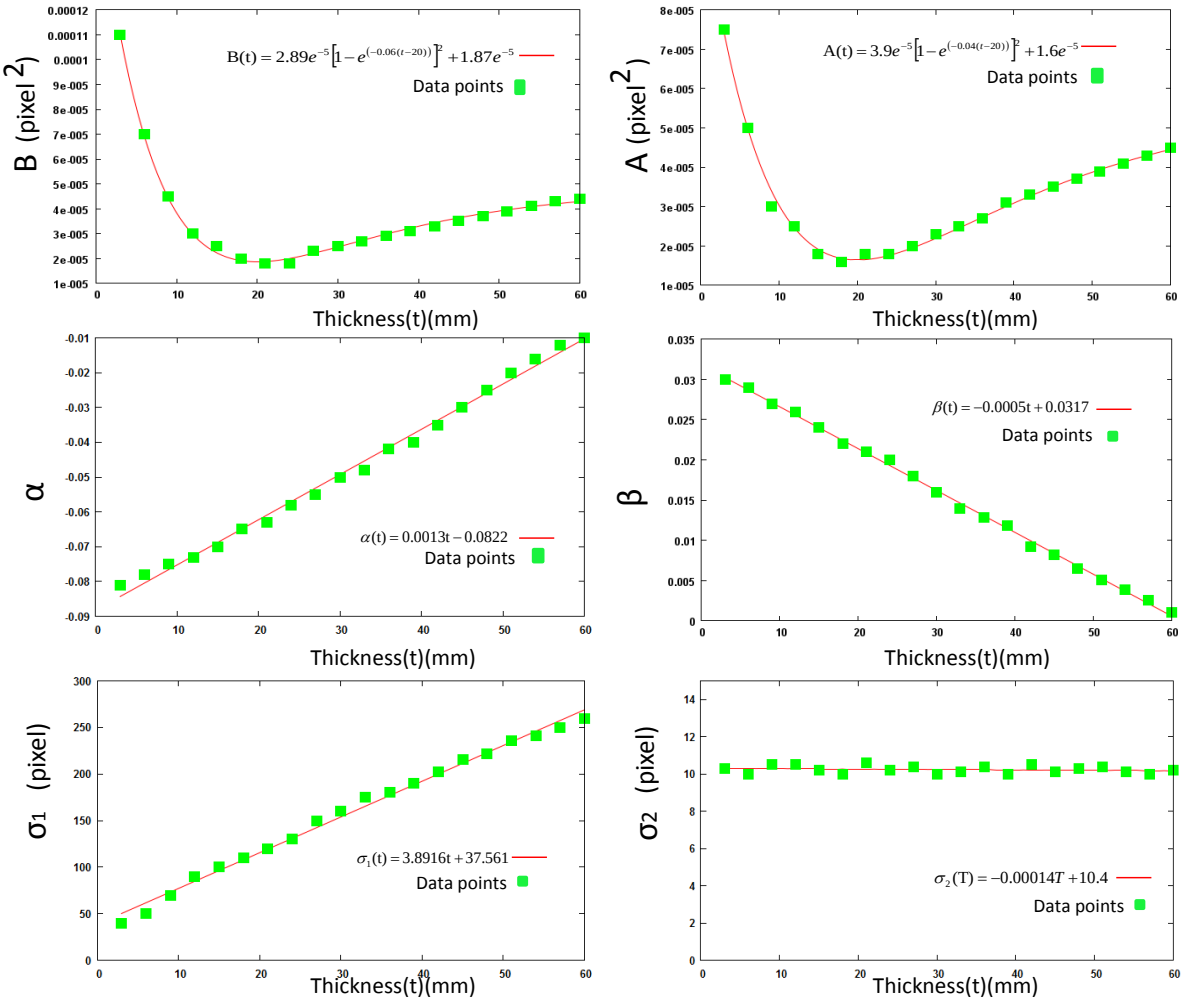

Figure 2.6: Fitting of parameters $\alpha, \beta, A, B, \sigma_1, \sigma_2$ with thickness

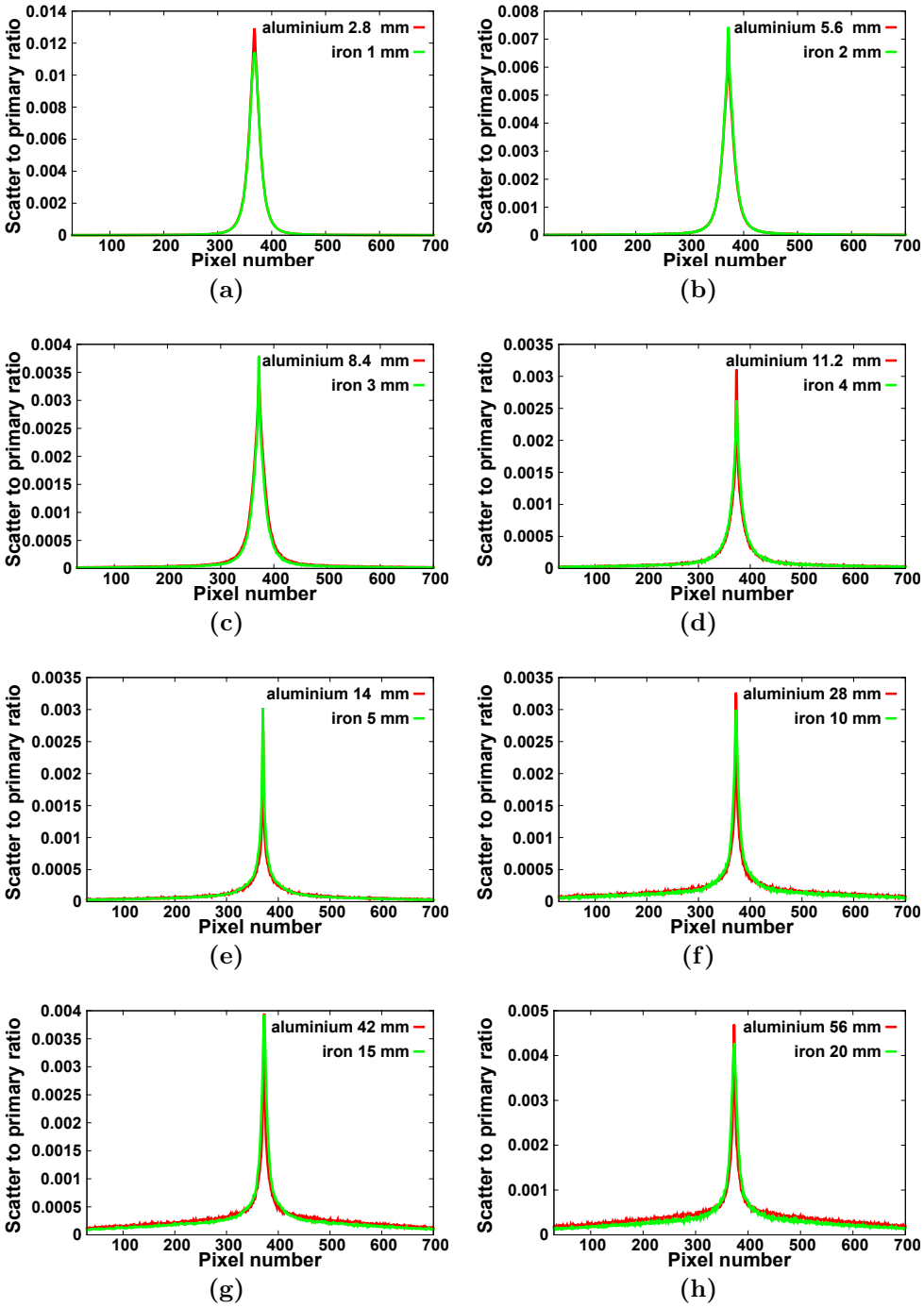

Figure 2.7: Comparison of aluminium slab kernels with equivalent thickness iron slab kernels

The kernels for aluminium and the equivalent thickness of iron using $\gamma = 2.8$, computed from equation 2.12, for the geometry described in section 2.7.2 are compared in figure 2.7 for different slab thicknesses. It can be seen from the comparison of the kernels (figure 2.7) that scatter to primary ratio is almost identical for aluminium slab and its equivalent thickness of iron slab. The relative absolute error with respect to thickness aluminium-equivalent kernels and iron kernels is between $5-8\%$ as shown in figure 2.8b). This allows us to evaluate the scatter correction of projections using only aluminium slab kernels. The results obtained are shown in section 2.8.4.

2.8.2 Multiplicative iteration vs additive iteration

To check the efficiency of multiplicative iteration approach Vs additive iteration approach, we randomly initialized the scatter estimate maps N (=50 in our case) times for each type of iteration process. We then calculate the mean of the error in the convergence value from the true value, for these N initial estimates at each iteration step. We plot the error vs number of iteration plot for multiplicative approach and additive approach for different values of λ. The result obtained is given in figure 2.9.

In our case, we choose the maximum value of $\lambda = 0.45$ to ensure that the first estimate of scatter is lower than the measured signal. From figure 2.9, it can be seen that additive approach is sensitive to the value of λ converges with a higher error as compared to multiplicative scheme, due the presence of negative primary estimates within the iteration steps. The multiplicative approach, however, ensures positive primary estimate at each iteration step as well as converges with a faster rate (in this case iteration step 20).

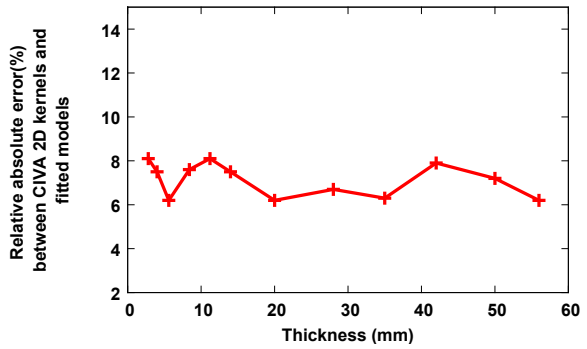

(a)

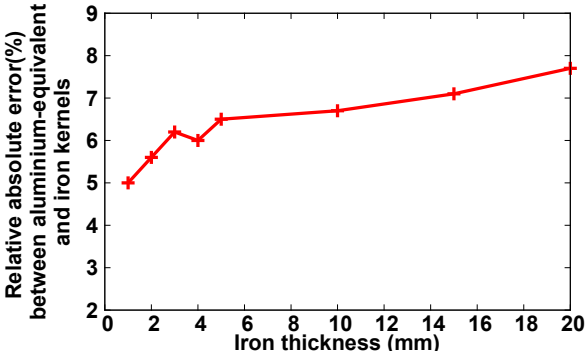

(b)

Figure 2.8: Plot of relative absolute error with respect to thickness between (a) CIVA 2D kernels and fitted models (b) aluminium-equivalent kernels and iron kernels

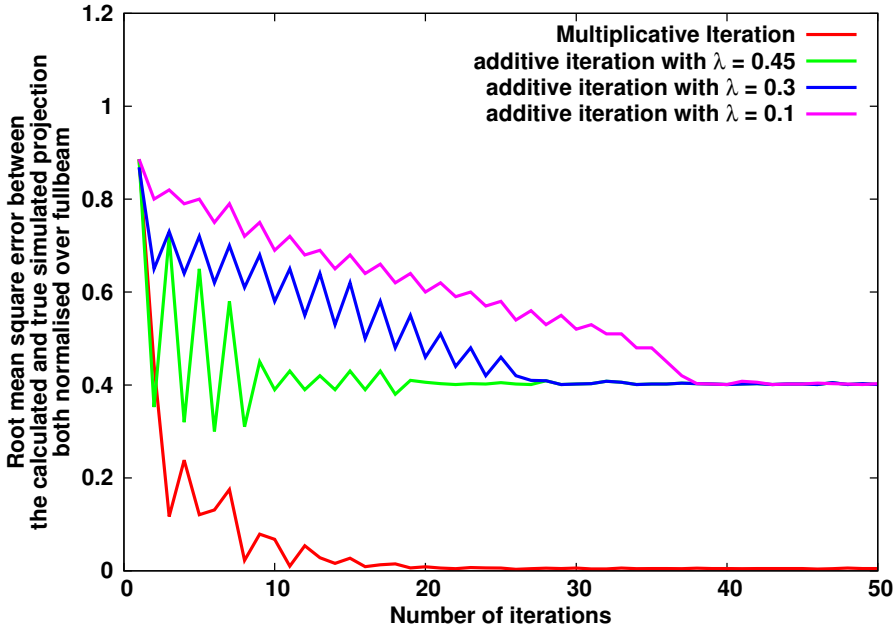

Figure 2.9: Plot of error Vs Number of iteration for different iteration schemes

2.8.3 Scatter correction on homogeneous object

Figure 2.10 displays a sample projection of the iron-hub. To evaluate the performance of continuous and discrete scatter correction on the projections, the vertical and horizontal profiles of the corrected and uncorrected normalized projections are plotted in figure 2.11. Figure 2.11 also displays calculated scatter profiles with discrete and continuous approach.

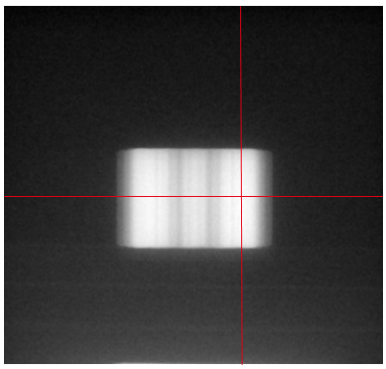

Figure 2.10: Sample projection of iron hub sample

On the vertical profile of corrected projection 2.11(b), we can see that the continuous method performs better edge enhancement of the object than the discrete method. This is due to better sampling of the kernels with respect to thickness at the edges.

Figure 2.12 displays reconstruction slices of the top tip of the iron hub obtained for uncorrected and corrected projections using continuous and discrete methods. Table 2.1 displays the mean and standard deviation of the reconstructed values for corrected and uncorrected data in air and iron region calculated using binary masks.

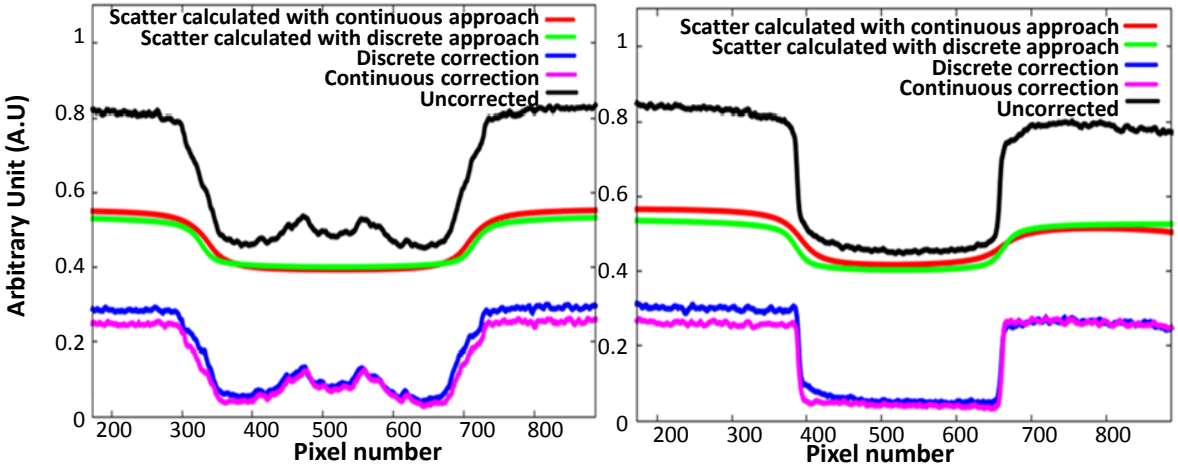

Figure 2.11: a) Horizontal profile b) Vertical profile of uncorrected and corrected projection by continuous and discrete method

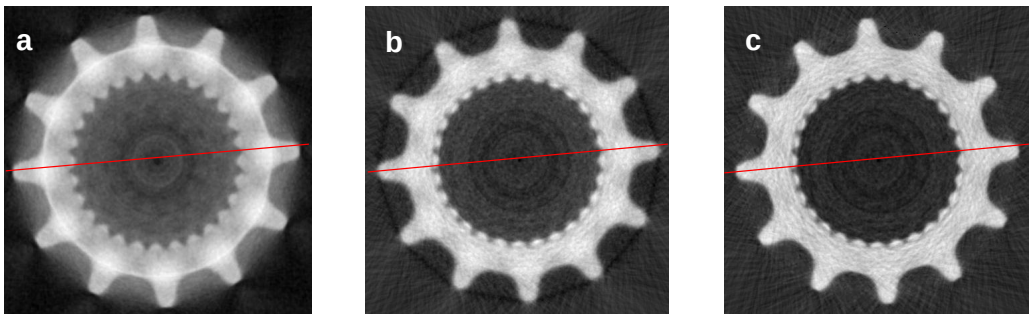

Figure 2.12: Reconstruction slice of a) Uncorrected projections b) Corrected projections by discrete method c) Corrected projections by continuous method

		mean (cm^{-1})	std. dev.
Uncorrected	air	0.024	± 0.002
	iron	0.196	± 0.007
Discrete corrected	air	0.003	± 0.006
	iron	0.634	± 0.005
Continuous corrected	air	0.001	± 0.006
	iron	0.800	± 0.009
Mean spectrum value	air	0.000	
	iron	0.836	

Table 2.1: Mean and standard deviation values for aluminium and iron region for uncorrected and corrected reconstruction slices

Uncorrected value of 0.196 cm^{-1} for the linear attenuation coefficient of iron is estimated by the discrete approach at 0.634 cm^{-1} whereas it is estimated at 0.80 cm^{-1} by

the continuous approach. In the considered energy range, the value of linear attenuation constant per cm for mean energy 319 keV is 0.836 cm^{-1}, which is in agreement with the obtained result. The continuous method presents improved reconstruction values with respect to the discrete approach as can be seen in figure 2.13, which gives the plot profile of the reconstruction slice shown in figure 2.12, which exhibits better edge enhancement by the continuous approach.

The obtained result of the scatter profile and reconstruction values is in agreement with correction performed using beam stop arrays method by A. Peterzol [6], which requires many acquisitions for the correction leading to higher dose.

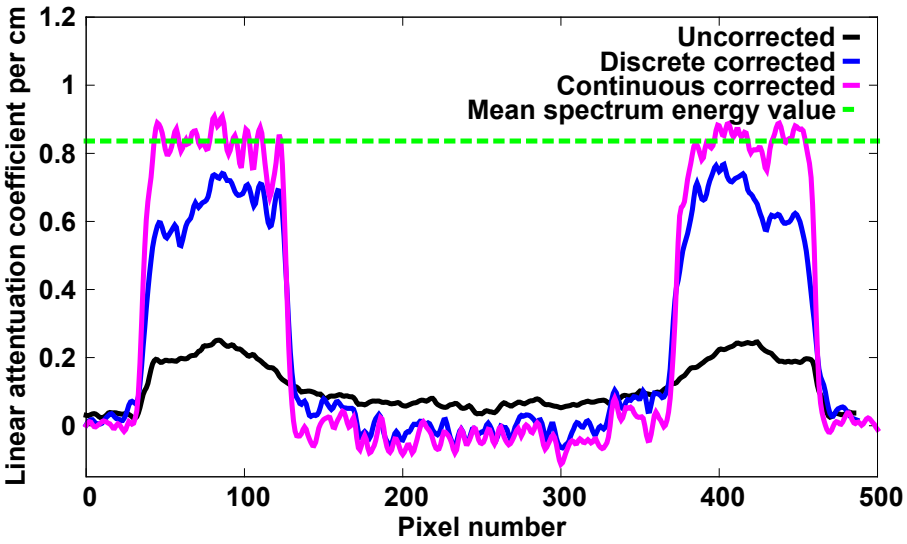

Figure 2.13: Plot profile of the reconstruction slice of a) Uncorrected projections b) Corrected projections by discrete method c) Corrected projections by continous method

2.8.4 Scatter correction on heterogeneous object

Figure 2.14(a) shows the profile of the scatter obtained by simulation in CIVA. It is compared with the scatter profile obtained by the continuous and the discrete corrections. The relative error profiles of continuous scatter and discrete scatter with respect to the true value obtained from CIVA are also plotted. Clearly at the edges of the object continuous approach has lesser relative error as compared to discrete approach.

Figure 2.14(b) and 2.14(c) show horizontal and vertical profile of the projection without scatter obtained in CIVA compared with corrected projection profile using the continuous and the discrete approach and their relative error profiles.

Figure 2.15 displays reconstruction slices obtained for uncorrected and corrected projections using the continuous and the discrete method. Table 2.2 displays the mean and standard deviation of the reconstructed values for corrected and uncorrected data for aluminium and iron region.

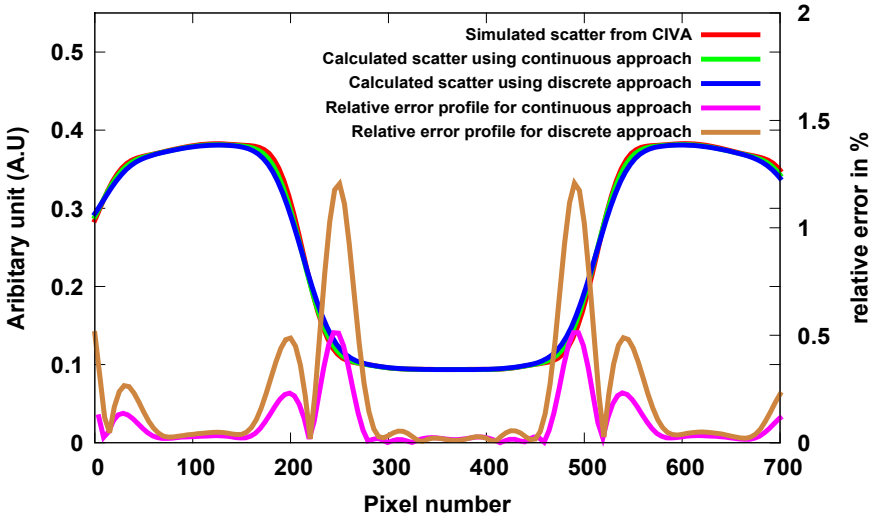

(a) Plot profile of the scatter obtained using continuous and discrete approach

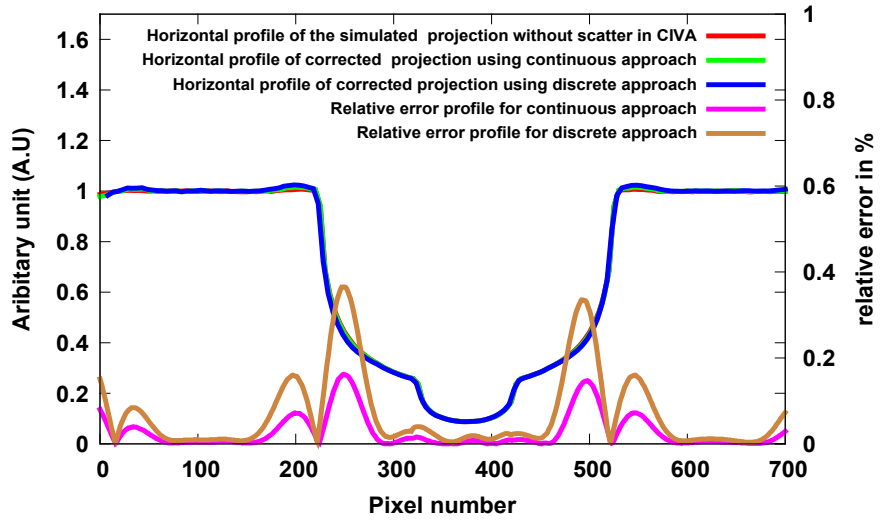

(b) Horizontal profile of corrected projection using continuous and discrete approach

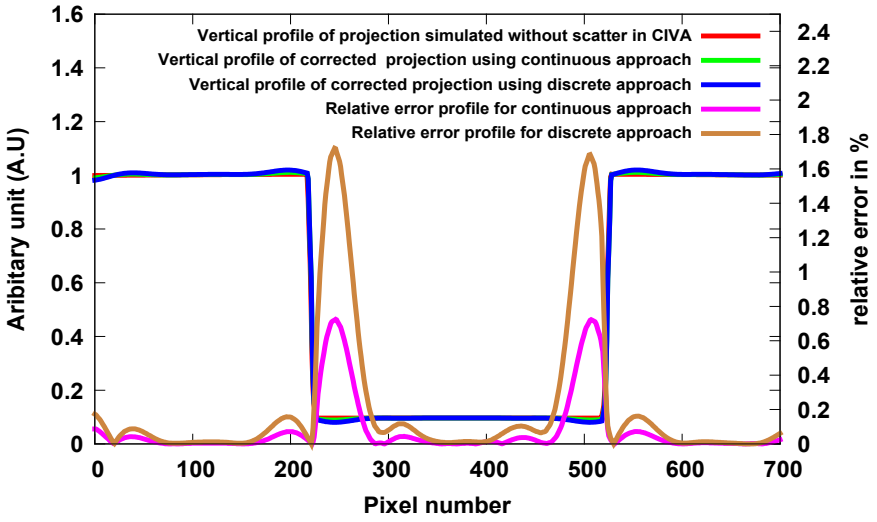

(c) Vertical profile of corrected projection using continuous and discrete approach

Figure 2.14: Plot profiles of scatter and corrected projections for the heterogeneous object

The plot profile of the uncorrected and corrected reconstruction slices is shown in figure 2.16. The algorithm performs efficiently using only aluminium slab kernels. The linear attenuation coefficient obtained for iron and aluminium is 0.718 cm^{-1} and 0.249 cm^{-1} respectively for the continuous approach, which is in agreement with the expected linear attenuation value of 0.247 cm^{-1} for aluminium and 0.720 cm^{-1} for iron at 450 keV monochromatic source. However, comparing the standard deviation, we notice that the difference in the attenuation coefficient of aluminium and iron obtained by discrete and continuous approach is not significant.

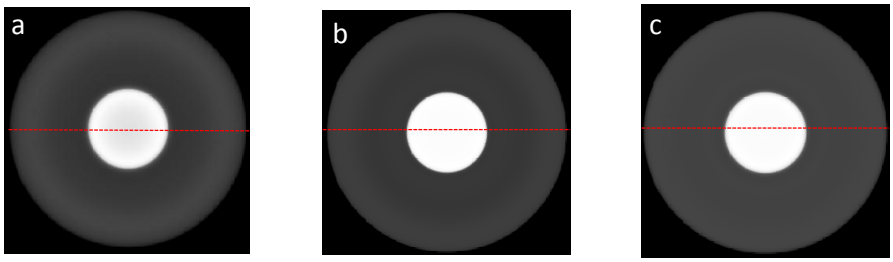

Figure 2.15: Reconstruction slice of a) Uncorrected projections b) Corrected projections by discrete method c) Corrected projections by continuous method

		mean(cm^{-1})	std.dev	Relative absolute error (%)
Uncorrected	aluminium	0.268	± 0.001	8.5
	iron	0.560	± 0.006	22
Discrete corrected	aluminium	0.252	± 0.009	2.0
	iron	0.713	± 0.005	0.9
Continuous corrected	aluminium	0.249	± 0.007	0.8
	iron	0.718	± 0.004	0.2
Theoretical values	aluminium	0.247		
	iron	0.720		

Table 2.2: Mean and standard deviation values for aluminium and iron region for uncorrected and corrected reconstruction slices

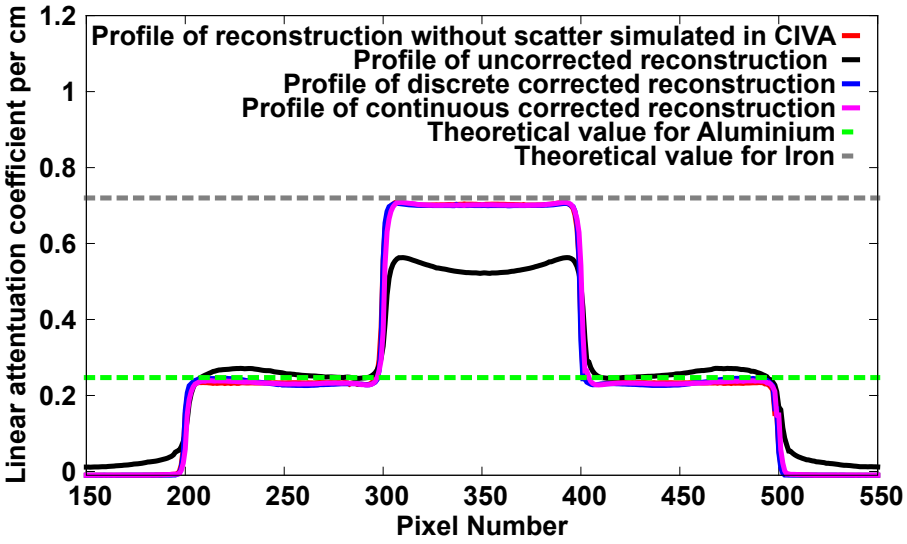

Figure 2.16: Plot profile of the reconstruction slice obtained with a) Projection without scatter from CIVA b) Uncorrected projections c) Corrected projections by discrete method d) Corrected projections by continuous method

2.9 Discussion and conclusion

Scatter Correction using pencil beam kernels produced significant improvement in the quantitative reconstruction values for the homogeneous object like iron hub. We adopted a continuous kernel approach by interpolating the kernels for each thickness. This approach offers superior improvement in the edges of the object after correction due to extended number of kernels. The reconstruction values are also improved in the continuous approach with respect to the discrete one, especially for areas in the reconstruction slices where thin and thick structures are connected such as the tips of the iron hub. This shows superior efficiency of continuously-thickness adapted kernels to calculate scatter distribution in complex geometries.

We also adopted a multiplicative iteration scheme which offered better convergence and ensured positive primary estimates at each iteration step as compared to additive iteration scheme which does not ensure positive primary estimates for higher SPR. As a result, multiplicative approach gives lesser error from the true value value as compared to additive iteration approach.

The algorithm has been also tested for heterogeneous object. At the energy range used, Compton scattering is the most dominant interaction. The likelihood of interaction is proportional to electron density and is independent of the atomic number of the material. Therefore, kernels corresponding to a single material can be utilized for the correction of heterogeneous object projections. The obtained results are well within the expected reconstruction values proving the efficiency of the algorithm for heterogeneous objects.

Beam hardening correction is well taken care of by the filtering procedure in the acquisition. A high filtration of 4 mm of Pb + 1 mm of Cd removes 96% of photons which are below 200 keV.

In the simulation of kernels, we noticed strong peak of the kernels in the center pixels of

the impinged pencil beam. This contribution in the kernels could be coming from the contribution of the high frequency scatter of the detector. The original two Gaussian scatter modeling was developed for modeling only the object scatter contribution. It was developed for medical energy range with an assumption of single order scattering coming from the object incorporating the amplitude factor term based on simple first order scattering. However, in this study we are adapting this method under different conditions such as higher SPR experienced in industrial applications. Moreover, we take combined scattering of the object and detector within the modeling of the scatter kernels and iteration step. We are not limited to first order scattering, as higher order scattering can have important contribution for the industrial energy range. Therefore the two-Gaussian modeling has limitations when applied with the conditions mentioned above. The scatter contribution from the object and detector are entangled. A higher order model of the scatter can help us identify the kernel contribution in terms of the source: object or detector, type of scatter: Rayleigh or Compton, order of the scattering: first or higher. Therefore, in the next chapter we want to evaluation higher order of kernel modeling for proper kernel identification.

Another factor to be taken care of is the correction of beam hardening. Here in this case study, a filtering method was adopted to correct most of the beam hardening effect which may not be the case in acquisition setup. We want to develop a generalized method to be used in each case to correct beam hardening. To perform this task we want to avoid using Beer-Lambert law for the calculation of thickness at each pixel, and instead incorporate thickness calculation using look-up table method which will also take care of the beam hardening in the scatter correction procedure. This method is also described in the next chapter.

With these aims in mind we begin to describe the next chapter which develops a separable model for the scattering of object and detector.

2.10 Chapter summary

In this chapter we presented a two-fold modification of the SKS scatter correction method presented by Sun et al. [5] with the pencil beam kernels. The continuously-thickness adapted kernels method [75] is proposed which empirically fits the parameters the kernels with respect to the thickness of the object and a continuous-map of kernels is obtained. The kernels are generated using MC simulations in CIVA. The fitting of the kernels is performed using least-square fitting with the two-Gaussian model accounting for the shape of the kernels. The parameters of the kernels are further fitted with respect to the thickness of the object using least-square fitting. The scatter correction is performed in an iterative manner taking the first estimate of the primary as the measured projection, convolution is performed using superposition of the kernels at each pixel. The thickness at each pixel is calculated using Beer-Lambert law often refereed to as Water Equivalent Thickness (W.E.T) when the slabs are made of water. The primary estimate is updated in a multiplicative manner which imposes the condition of positive primary estimates. Corrections are performed with experimental data of iron hub with both classical discrete correction and continuous method. Corrections are also performed on simulated data of object made of multi-material composed of iron and aluminium.

Chapter 3

Separable scatter model of the detector and object contributions

This chapter is based on the publication, Bhatia et al. "Separable scatter model of the detector and object contributions using continuously thickness-adapted kernels in CBCT" JXRT 2016.

The contribution of scattering of photons inside the detector itself becomes prominent and challenging in case of X-ray source of high energy which is used in typical industrial NDT. In this chapter, comprehensive evaluation of contribution of the detector scatter is performed using continuously thickness-adapted kernels. A separation of scatter due to the object and the detector is presented using a four-Gaussian model for a better adaptation to the low frequency contribution of the object and high frequency contribution of the detector. The obtained results are also validated experimentally using a collimator in front of the object to remove the contribution of the object scatter. This chapter also extends the scope of this scatter correction procedure to MeV energy data from a linear accelerator source. The results obtained for this energy range are also presented in chapter.

Summary

3.1 Introduction

A lot of research and development has been devoted to correct the scatter from the object under study. But lately, studies have proven the importance of scattering inside the detector [23][24][25] specially for the industrial energy range used in NDT. There are various interactions inside the detector that contribute to scattering inside the detector as detailed in section 1.4.2. The contribution of the scattering inside the detector can come from the Compton scattering inside the various parts of the detector like mountings, back plate etc. The effect of backscattering from the backplate of the detector increases rapidly with the higher energy source [26]. Additionally, the contribution of the X-ray fluorescence photons and glare produced by the optical photons also results in reduction of the spatial resolution.

In this chapter, we propose to evaluate the contribution of detector scattering at NDT energy range using continuously thickness-adapted Scatter Kernel Superposition (SKS) method [75] described in chapter two. This continuous method takes into account better sampling of the kernels with respect to the thickness of the object to get an accurate model of variability in shape and in amplitude of the scatter kernels over the whole thickness range. However, a two-Gaussian model has been adopted in the continuous method and other classical SKS method [5] for the fitting of kernels. This two-Gaussian parameterisation of kernels has several limitations. Firstly, the parameter fitting of the continuous model is tricky because the scatter contributions from the detector and the object are entangled. As the original two-Gaussian model was developed on for medical energy ranges for only single order scattering coming from just the object, we believe that this model is not sufficient for combining of detector and object scattering including the higher order scattering. Moreover, the high frequency contribution of the detector scatter generates a strong peak in the center pixel of the detector where the pencil beam is impinged. This shape calls for the necessity to explore an increase in order of the Gaussian model. Therefore, we propose in this chapter, to identify the respective scatter contributions of the object and detector using a four-Gaussian model to have a more stable modeling. The experimental validation of the model is also given with the results obtained using collimator slits in between the detector and the object.

The effect of scattering becomes more prominent when the input X-ray energy is higher. Specially in case of MeV energy, a number of aspects are needed to be taken into account. First of all, there is an appreciable increase in the forward Compton scattering of the photons and hence they are more likely to reach the detector. Also, these scattered photons are more energetic and therefore more likely to escape from the scattering object. By increasing the incident energy, the energy of charged particles released (recoil electrons and positrons) in the scattering object also increases, resulting in a marked increase in the number of photons generated through the bremsstrahlung process. At photon energies in excess of 1.022 MeV, positrons are generated through pair production, which, upon annihilation, produce photons that can contribute to the scatter fluence. We also extend the scope of the continuously thickness-adapted kernels over the MeV energy data using a linear accelerator of 6 MeV in this chapter.

The outline of the chapter is as follows. We begin by describing the four-Gaussian analytic description of the kernels. Subsequently, the CBCT acquisition setup used for generating keV and MeV data is described in detail. To take into account the beam

hardening effect, a fitting procedure to calculate the thickness at each pixel is described using the look-up table. An in-depth analysis of the four-Gaussian contributions is carried out in section 3.3. Experimental validation is then performed with both fan beam and cone beam geometries. Finally results obtained for MeV data are also shown in detail.

3.2 Method and materials

3.2.1 Four-Gaussian model

In the SKS scatter correction approach with continuously thickness-adapted kernels [75], the scatter signal can be modeled as the sum of the scatter contributions from a group of pencil beams passing through the object and the detector. For each pencil beam input, a resulting kernel which has the weight of the scatter to primary ratio is determined. The total scatter signal $S(m,n)$ with m and n as the pixel position on the detector, can then be modeled as:

$$S(m,n) = \sum_k \sum_l P(k,l) K_{T(k,l)}(m-k, n-l) \tag{3.1}$$

where, K_T is the thickness (T) dependent kernel, with amplitude equal to the ratio of the scattered signal at the current pixel to the primary signal, at the pencil beam centered pixel. P is the primary signal contributed by the photons passing directly without any attenuation. Instead of using Beer-Lambert law based on an effective linear attenuation coefficient [5], the thickness $T(k,l)$ in equation 3.1 is directly computed from a look-up table function f_{BH} – computed during the calibration stage of the kernels – that relates the true slab thickness with respect to the transmittance

$$T(k,l) = f_{BH}\left(\frac{P(k,l)}{I_o(k,l)}\right) \tag{3.2}$$

where I_o is the unattenuated image. It is worthy to note that the beam hardening is taken care of with this procedure. The acquisition parameters and the material of the calibration slabs must be the same as the object under study. Value of directly transmitted primary fluency P was calculated for each thickness of the simulated slabs. The thickness in terms of the transmittance $P(k,l)/I_o(k,l)$ is calculated as described in section 3.3.1.

The pencil beam kernel K_T can be fitted into the equation formed by four circularly symmetric Gaussian functions describing the shape of the kernel as:

$$\begin{aligned} K_T(m-k, n-l) = A\exp\left(-\frac{(m-k)^2+(n-l)^2}{2\sigma_1^2}\right) + B\exp\left(-\frac{(m-k)^2+(n-l)^2}{2\sigma_2^2}\right) \\ + C\exp\left(-\frac{(m-k)^2+(n-l)^2}{2\sigma_3^2}\right) + D\exp\left(-\frac{(m-k)^2+(n-l)^2}{2\sigma_4^2}\right) \end{aligned} \tag{3.3}$$

The four-Gaussian model is necessary in order to clearly separate the contributions of the object and the detector.

The schematic representation of the projection wise scatter correction process by four-Gaussian model is shown in figure 4.2

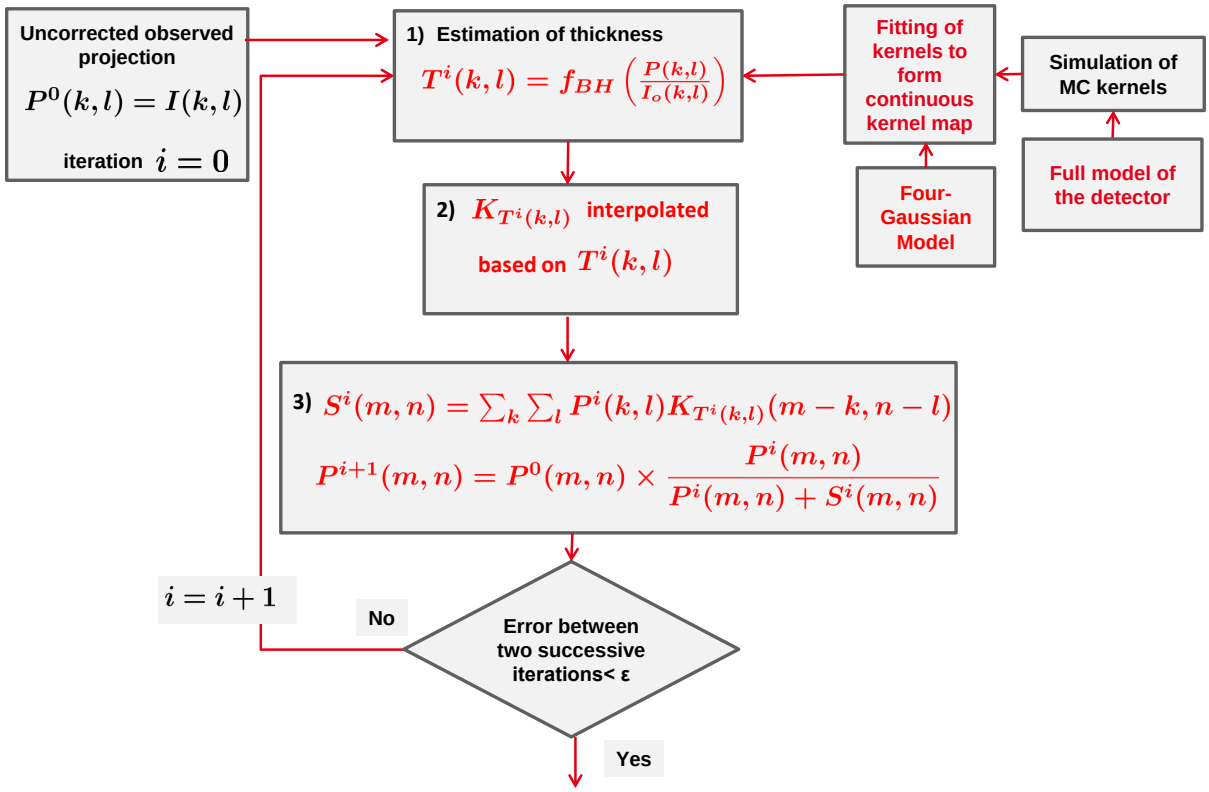

Figure 3.1: Schematic representation of the projection wise scatter correction process with the four-Gaussian model. The modifications with respect to discrete approach by Sun et al. [5] are shown in red.

3.2.2 Kernel generation and fitting

Monte Carlo (MC) simulations were performed in the CT module of CIVA software [3] for the generation of kernels. Pencil beam source was impinged on slabs of the same material as the object under study and discrete set of point spread 2D kernels were obtained on the flat panel detector.

The flat panel was modeled in a standard multi-layer representation consisting of 0.1 mm aluminium front layer followed by air-gap of 0.8 mm, a 600 µm CsI layer, 1 mm silicon substrate and finally a 1 mm lead back plate.

The eight parameters of equation 3.3, $A, B, C, D, \sigma_1, \sigma_2, \sigma_3, \sigma_4$ are also interpolated in terms of thickness to obtain a continuous kernel map with respect to the thickness [75]. We have used a four-Gaussian model in order to separate the contribution of the object and the detector. To get realistic kernels and in particular to take into account optical

processes in the detector, real acquisitions on slabs of various thickness could also be advantageously used in practice with an X-ray pencil beam geometry as described in the next chapter.

3.2.3 Acquisition setup with aluminum turbo

For the acquisition setup, the source to detector distance was 845 mm and the distance between the source and the axis of rotation was at 424 mm. The setup mainly consisted of an X-ray source, an object rotational table and a flat panel detector. The X-ray source unit of maximum 230 kV was used. A copper filter of 0.35 mm was used in the spectrum. Flat panel detector used had a size 1840 $\times$ 1456 with 2 $\times$ 2 binning size and 0.254 mm pixel size.

Acquisitions were performed on an aluminum turbo as given in figure 3.2 which had a maximum dimension of around 300 mm.

Figure 3.2: Picture of the sample of aluminum turbo

3.2.4 Acquisition setup with collimator slit

In order to validate our results with experimental results, acquisitions were performed with collimator slits inserted in between the object and the detector. The setup is described in figure 3.3. The collimator slits were made of steel, with a thickness of 30 mm and width of 15 mm. The introduction of the collimator removed approximately all the contribution of the object scatter.

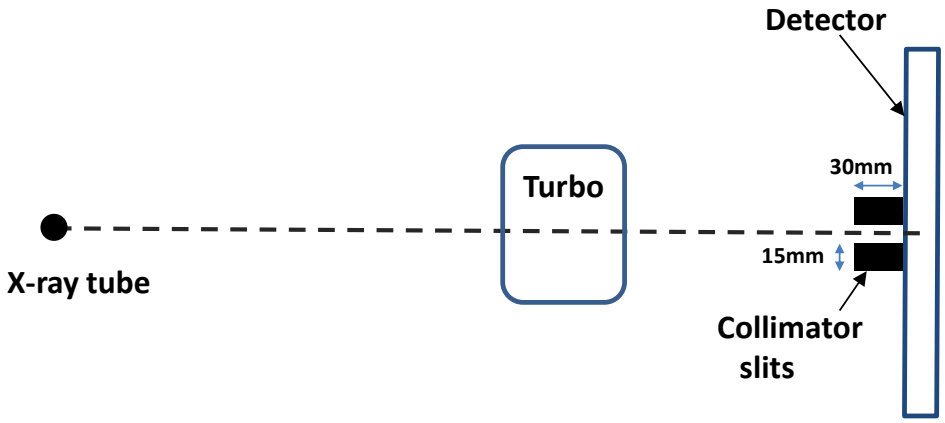

Figure 3.3: Schematic of the acquisition setup with the collimator slit

3.2.5 Acquisition setup with iron gear

The acquisitions were performed with a linear accelerator 6.0 MV source. The source to detector distance was 3.18 m and the source to object distance was 2.45 m. The acquisitions were performed on the gear made of iron as shown in figure 3.4 with a maximum diameter of 7.5 cm. The detector used was a flat panel detector with the pixel size of 200 µm, consisting of a 10 mm copper window. We want to compare the CIVA simulations with the Penelope simulations, as CIVA simulations have not been benchmarked for MV energy range.

Figure 3.4: Picture of the iron gear sample

3.3 Results

This section presents the results for the keV data and MeV data using the four-Gaussian model.

3.3.1 Results for keV data

Fitting for calculation of thickness

As discussed in section 3.2.1, in order to calculate the thickness at each pixel, simulations were performed with slabs of different thicknesses. The acquisition parameters and the material of the slabs were kept the same as the object under study. The value of directly transmitted primary fluency P was calculated for each thickness of the simulated slabs.

The thickness vs transmittance LUT f_{BH} given in equation 3.3 has been calculated using least square fitting as shown in figure 3.5 to determine the coefficients a_1,b_1, a_2, b_2 in equation 3.4. The classical thickness determination based on the effective linear attenuation coefficient is also shown by the red curve in figure 3.5. The beam-hardening, although not really strong, is clearly visible. Equation 3.4 gives the relationship of thickness T value in terms of transmittance $P(k,l)/I_o(k,l)$.

$$\begin{aligned} T(k,l) &= f_{BH}\left(\frac{P(k,l)}{I_o(k,l)}\right) \\ &= -a_1 \ln\left(\frac{P(k,l)}{I_o(k,l)}\right)^{b_1} - a_2\left(\ln\frac{P(k,l)}{I_o(k,l)}\right)^{b_2} \end{aligned} \tag{3.4}$$

using $a_1 = 20.8$, $b_1 = 0.83$, $a_2 = 0.000572$, $b_2 = 1$

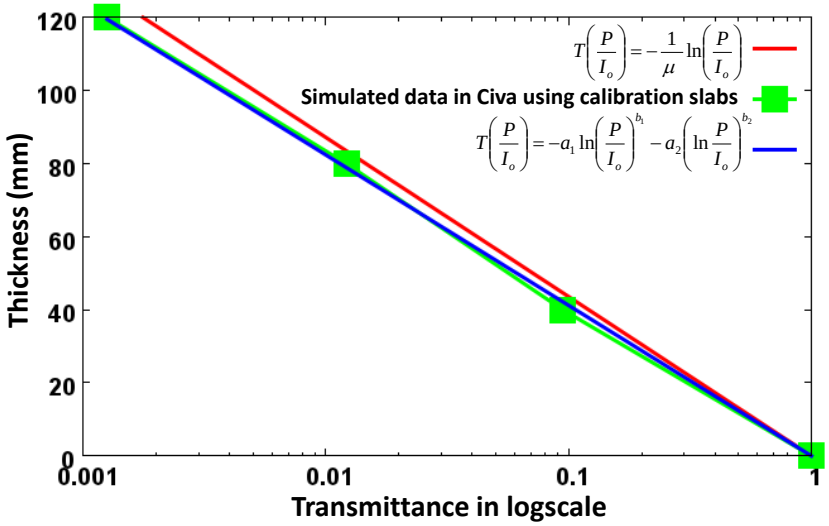

Figure 3.5: Fitting of thickness vs transmittance curve to obtain the correct value of the thickness in terms of the transmittance

Empirical fitting of kernels for continuous kernel map

The fitting of parameters $A, B, C, D, \sigma_1, \sigma_2, \sigma_3, \sigma_4$ of the four-Gaussian model with respect to thickness using least square fitting is shown in figure 3.6. From the fitting of these parameters, we observe that the standard deviation σ_1 and σ_2 vary over the thickness of the object whereas σ_3 and σ_4 remain constant. We can draw inference that σ_1 and σ_2 give the the scattering contribution of the object which increases over the thickness of the object. Moreover, we notice that σ_1 is very far from σ_2. Henceforth, we analyze that σ_1 displays the low frequency contribution of multiple scattering inside the object, whereas σ_2 gives comparatively low order scattering contribution. We also mark not much differences in the parameters A & B which weight the amplitude of the Gaussians. This variation of parameters A, B, σ_1, σ_2, demonstrate that atleast a two-Gaussian model for the object is necessary.

Similarly, observing σ_3 and σ_4 remain constant over the thickness of the object, we infer that σ_3 and σ_4 define the high frequency contribution from the detector. Following the same line of reasoning, σ_3 and σ_4 are different from each other whereas and parameters C & D are not outlying each other. The amplitude parameters for the detector, $C\&D$, decrease with thickness. Due to the higher attenuation, lesser primary intensity reaches the detector leading to fewer Compton scattering events in the detector and its surrounding. Also, D, which weights the higher frequency detector contribution, remains constant while C, which weights comparatively lower frequency detector contribution, decreases with respect to thickness. One explanation of this behavior could be that C is related to the back scattering from the back plate and since the effective energy increases with respect to thickness, the scattering from the back plate becomes less and less back scattered. Whereas, D could be related to florescence in the scintillator, which remains constant over the thickness. Therefore, atleast a two-Gaussian model for the detector is also crucial.

Scatter correction on aluminum turbo

Figure 3.12 a) displays the reconstruction slice obtained with uncorrected projections using FDK algorithm [11]. We first evaluated the scatter contribution of the object alone and we corrected the projections with only scatter kernels of the object. The result obtained is shown in figure 3.12 b). It clearly shows that the scatter correction due to only object is not sufficient as scatter artifacts are still visible in the reconstruction image. This is also demonstrated in figure 3.8 which displays the plot profile of the corrected and the uncorrected reconstruction slices. The scatter kernels of the detector and the object were then used to perform the corrections of the projections. The reconstruction obtained with this correction is shown in figure 3.12 c). The obtained result with the scatter correction of the object and the detector is in agreement with the expected value of the effective linear attenuation coefficient at a mean energy of 100 keV (0.48 per cm).

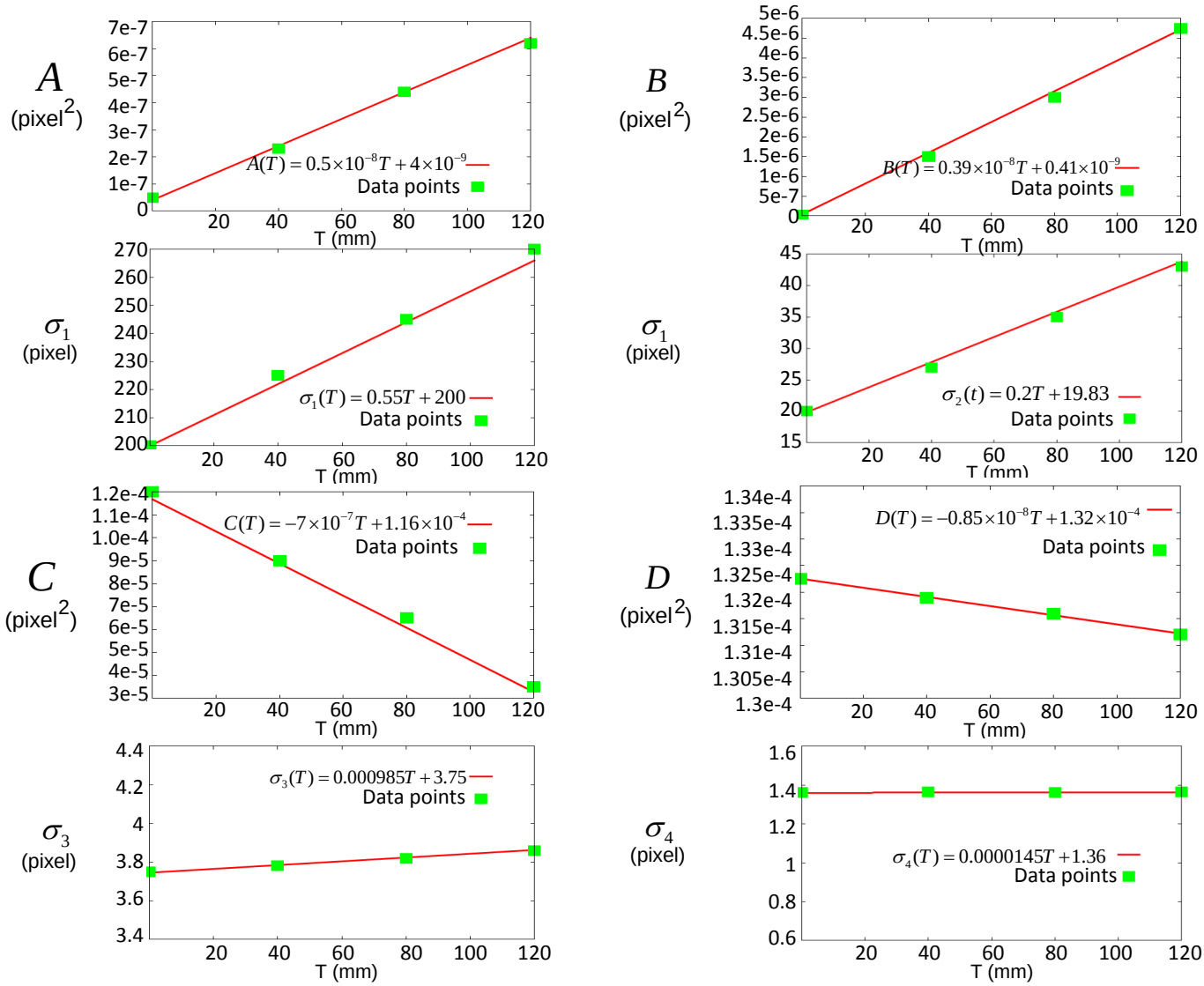

Figure 3.6: Fitting of parameters $A, B, C, D, \sigma_1, \sigma_2, \sigma_3, \sigma_4$ with thickness

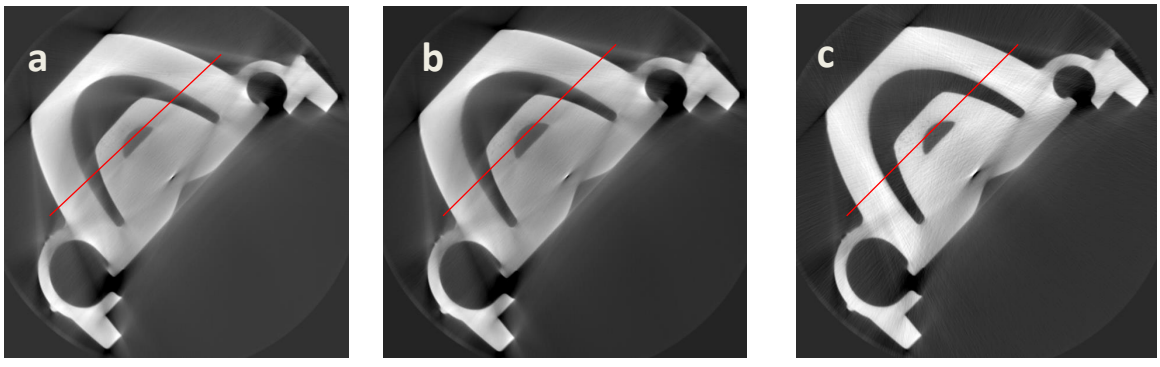

Figure 3.7: Reconstruction slice with a) uncorrected projections b) corrected projections by only scatter kernels c) corrected projections by scatter and detector kernels

Figure 3.8: Plot profile of uncorrected and corrected reconstruction slice by only scatter kernels and scatter and detector kernels. The black horizontal line represents the constant value of linear attenuation coefficient of aluminum at the mean energy of the spectrum used.

Table 3.1 displays the mean and standard deviation of the reconstructed values for corrected and uncorrected data in air and aluminum region, calculated using binary masks. Uncorrected value of 0.258 cm^{-1} for the linear attenuation coefficient of aluminum is estimated. By using only the object scatter kernels, we obtain a value of 0.324 cm^{-1} for the linear attenuation coefficient of aluminum. In the considered energy range, the value of linear attenuation constant for mean energy 100 keV is 0.48 cm^{-1}. The relative absolute error is 32.5% in the case of scatter correction with only the object kernels. Whereas, for the detector and the object kernels, we obtain a value of 0.510 cm^{-1} for aluminum. Also, the relative absolute error is reduced to 6.25%. The remaining artifact that we see in the scatter corrected reconstruction arise from the very high attenuation along the largest dimension of the object. The dynamic range of the detector was not high enough to take into account the attenuation along the largest dimension.

		mean (cm^{-1})	std. dev.
Uncorrected	aluminum	0.258	± 0.008
	air	0.098	± 0.005
Object scatter correction	aluminum	0.324	± 0.001
	air	0.106	± 0.006
Object and detector scatter correction	aluminum	0.510	± 0.008
	air	0.001	± 0.007
Mean spectrum value	aluminum	0.48	
	air	0.000	

Table 3.1: Mean and standard deviation values for aluminum and air region for uncorrected and corrected reconstruction slices

Validation by experimental result using a collimator

In order to validate the results obtained with the continuously thickness-adapted SKS scatter correction algorithm, we performed acquisitions using a collimator made of steel with 30 mm thickness. The setup is described in the section 3.2.4. Fan beam was produced and the contribution of the scatter from the object was eliminated by introducing collimator slits between the object and the detector. All the other acquisition parameters were kept same as the previous setup without the collimator slits. The reconstruction was performed on the projections obtained with this setup and the result is shown in figure 3.9 a). It clearly shows the presence of scatter artifacts due to the detector. We compare this experimental result with the result obtained by scatter correction performed by the algorithm using only the object scatter kernels as shown in figure 3.9 b). Figure 3.10 compares the plot profile of the experimental result with the collimator slits and the scatter correction by the algorithm using the object scatter kernels. The plot profiles demonstrate identical results, validating the results obtained by the algorithm and proving considerable contribution of detector scatter.

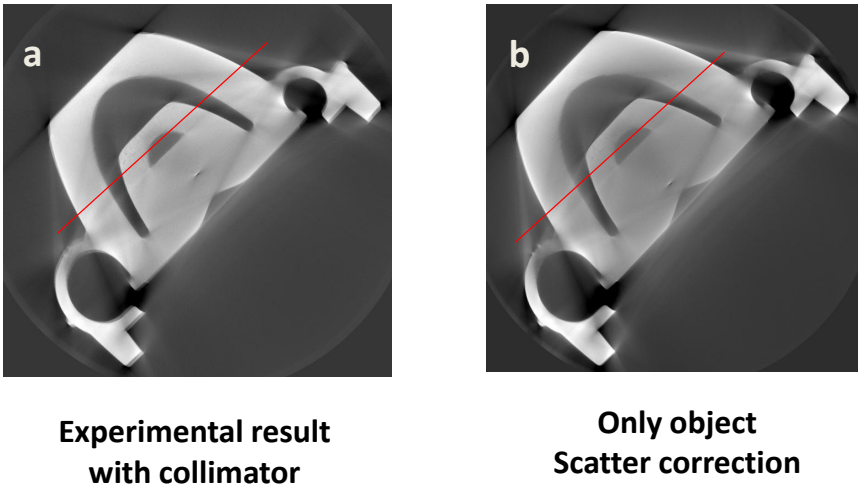

Figure 3.9: Reconstruction slice by a) experimental results with collimator b) corrected projections by only the object scatter kernels.

Figure 3.10: Plot profile of experimental result obtained with the collimator slits and the scatter correction with the object scatter kernels. The black horizontal line represents the constant value of linear attenuation coefficient of aluminum at the mean energy of the spectrum used.

		mean(cm^{-1})	std.dev
Experimental result with collimator	aluminum	0.312	± 0.006
	air	0.096	± 0.002
Correction with object scatter kernels	aluminum	0.324	± 0.009
	air	0.106	± 0.007
Theoretical values	aluminum	0.480	
	air	0.000	

Table 3.2: Mean and standard deviation values for aluminum and air region for experimental result with collimator and correction with the object scatter kernels

Table 3.2 displays the mean and standard deviation of the reconstructed values for air and aluminum region for experimental result and correction with object scatter kernels. The linear attenuation coefficient obtained for aluminum and air is 0.312 cm^{-1} and 0.096 cm^{-1} respectively for the experimental result. This is in agreement with the scatter correction with the object kernels result, which is 0.324 cm^{-1} for aluminum and 0.106 cm^{-1} for air. In the considered energy range, the value of the linear attenuation coefficient for mean value of spectrum (100 keV) is 0.48 cm^{-1} and 0.0001 cm^{-1} for aluminum and air respectively. This result demonstrates that, in this case study, the object scatter correction is not sufficient and the detector scatter contribution also needs to be taken into account to obtain correct reconstruction values.

3.3.2 Results for MeV data

Kernel simulation using CIVA and Penelope

Figure 3.11 shows the simulated kernels with iron slabs using CIVA and Penelope. We observed a discrepancy in the simulated kernels with CIVA and Penelope, especially in the case of smaller thickness of the slabs. This discrepancy could arrive from the fact that in the CIVA simulation, the Bremsstrahlung effect produced after pair-production is not taken into account. Therefore, at the lower thicknesses this effect may be important as seen in figure 3.11. Whereas, for higher thicknesses, CIVA and Penelope correspond to each other due to self-attenuation of Bremsstrahlung photons inside the slab.

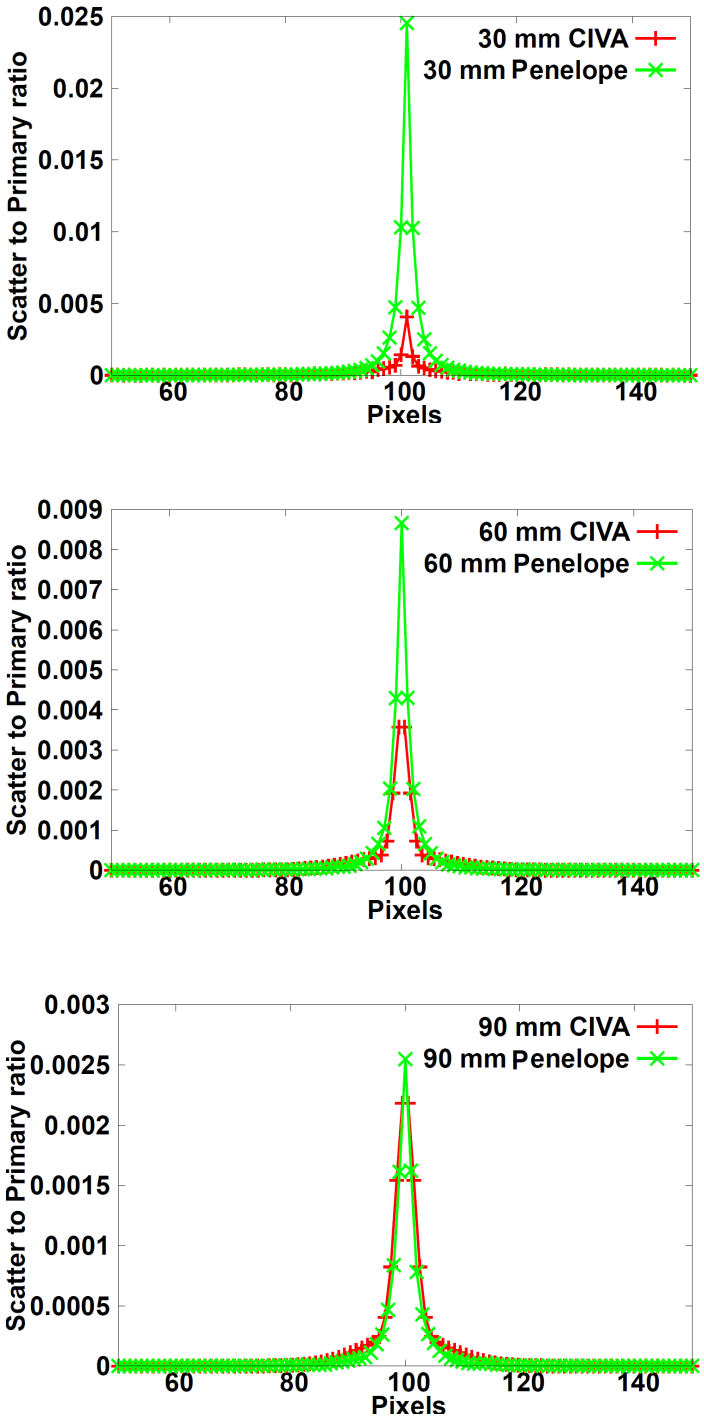

Figure 3.11: Comparison of simulation of the scatter kernels with CIVA and Penelope

Figure 3.12 a) displays the reconstruction slice obtained with uncorrected projections for the iron hub. The scatter correction on the projections was applied using continuously thickness-adapted kernels with the four-Gaussian model. The result obtained with CIVA is shown in figure 3.12 b) and the result obtained with Penelope is shown in 3.12 c). Figure 3.13 displays the cropped view of the reconstructions. We can notice the horizontal artifacts on the reconstruction images due to the jamming of the rotational axis during the acquisition, and not due to scatter.

Figure 3.14 shows the plot profile of the uncorrected and corrected reconstruction

images. Table 3.3 summarizes the mean and standard deviation of the reconstructed values for the corrected and the uncorrected data in air and iron region calculated using binary masks. It can be clearly seen that scatter correction with both CIVA and Penelope improves the contrast of the reconstruction image. Uncorrected value of 0.172 cm^{-1} for the linear attenuation coefficient of iron is estimated. We obtain a value of 0.388 cm^{-1} after the scatter correction with CIVA, and 0.395 cm^{-1} after the scatter correction with Penelope for the linear attenuation coefficient of iron. In the considered energy range, the value of linear attenuation constant for mean energy 900 keV is 0.44 cm^{-1}. The relative absolute error is reduced from to 60.9% to 11.7% for the CIVA correction and 10.4% for the Penelope correction.

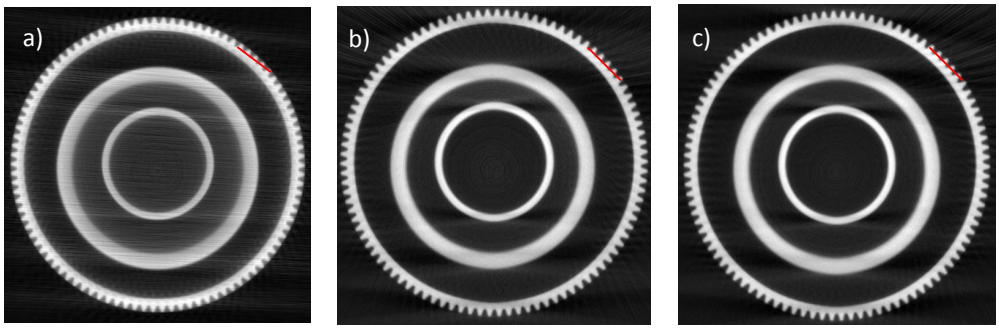

Figure 3.12: Reconstruction slice with a) Uncorrected projections b) Corrected projections with CIVA c) Corrected projections with Penelope

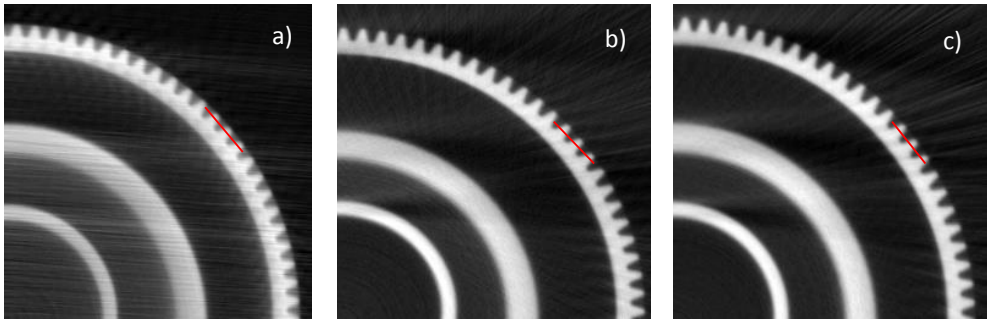

Figure 3.13: Cropped reconstruction slice with a) Uncorrected projections b) Corrected projections c) Corrected projections with Penelope

		mean (cm^{-1})	std.dev
Uncorrected	iron	0.172	±0.094
	air	0.095	±0.004
Correction with CIVA	iron	0.388	±0.032
	air	0.068	±0.004
Correction with Penelope	iron	0.395	±0.036
	air	0.055	±0.004
Mean spectrum value	iron	0.440	
	air	0.000	

Table 3.3: Mean and standard deviation for corrected and uncorrected projections

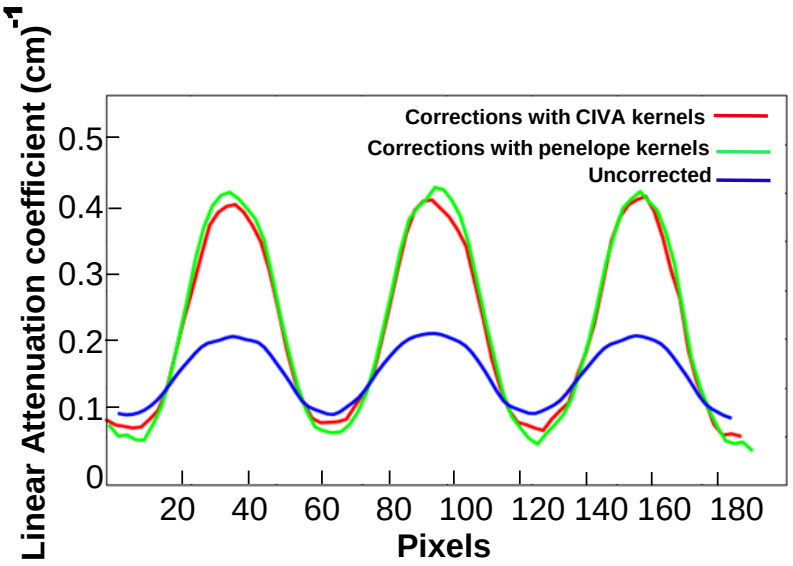

Figure 3.14: Plot profile of uncorrected and corrected projections

3.4 Discussion and conclusion

The scatter kernel fitting using the four-Gaussian model separates the low frequency contribution of the scatter due to the object and the high frequency contribution of the detector. This separation of the contributions is necessary to clearly follow the effect of the detector scatter on the reconstruction in CBCT by developing a separate model for the detector.

The object scatter itself requires a two-Gaussian model to take into account the higher order and the lower order scattering from the object. The amplitude parameters of scatter kernels $A\&B$ increase, with increase in thickness of the object because of the increase in SPR. σ_1 represents the very low frequency contributions from the object after multiple scattering of photons and σ_2 represents comparatively high frequency contribution from the object after fewer scattering of the photons. Both these parameters increase with the thickness of the object. Similarly, the high frequency contribution

of the detector model also requires a two-Gaussian model. The amplitude parameters for the detector, $C\&D$, decrease with thickness. Due to the higher attenuation, lesser primary intensity reaches the detector leading to fewer Compton scattering events in the detector and its surrounding. Also, D, which weights the higher frequency detector contribution, remains constant while C, which weights comparatively lower frequency detector contribution, decreases with respect to thickness. One explanation of this behavior could be that C is related to the back scattering from the back plate and since the effective energy increases with respect to thickness, the scattering from the back plate becomes less and less back scattered. Whereas, D could be related to florescence in the scintillator, which remains constant over the thickness. The high frequency contribution of the detector given by σ_3, σ_4 remain constant over the thickness of the object.

Since we have been able to identify that, two kernels in the four-Gaussian model are needed for detector kernel modeling and two for the object kernel modeling, in the next chapter we will represent the four-Gaussian model by notations clearly separating the detector and object contribution. The detector kernel parameters will be defined with a subscript "d" such as $w_{d,1}, w_{d,2}$ representing the amplitude and $\sigma_{d,1}, \sigma_{d,2}$ representing width of the two Gaussian. Similarly object parameters will be represented by a subscript "o" such as $w_{o,1}, w_{o,2}$ representing the amplitude and $\sigma_{o,1}, \sigma_{o,2}$ representing width of the two Gaussian.

Using this fitting of the scatter kernels, the projections were corrected for keV data to perform a comprehensive study of the contributions of the object and the detector scattering. The correction of the projections using only the object scatter kernels produced reconstruction image with scatter artifacts. The relative absolute error with respect to the expected value is 32.5% for the scatter correction with only the object kernels. The correction of projections using the object and the detector scatter kernels reduced the relative error to 6.25%. The results obtained were validated with experimental results using a collimator. The relative absolute error between the experimental result using collimator and the scatter correction using object kernel was 3.7%. This proved that the scatter correction due to object is not sufficient to completely remove scatter artifacts in the reconstruction. The contribution of the detector scattering becomes very important at the energy range used which is not taken into account in the CIVA simulations.

The obtained result proves, in this particular case study, that the correction of the scatter due to the object only is not sufficient to completely remove scatter artifacts in the reconstruction. The contribution of the detector scattering is significant at the energy range used. We remark that the detector scatter depends on several parameters including the spectrum used and components (front filter, back plate etc.) configuration of the detector. The importance of the contribution of the detector scatter over the object scatter will therefore depend on each case study. Although the information about the component structure of the detector was only approximate in the simulation model of this study – as it is generally kept anonymous by the manufacturer - the improvement in the scatter reduction using both object and detector scatter kernels is noteworthy. To further improve the realism of the detector kernels, either a more accurate 3D description of the detector could be used in the Monte Carlo simulation instead of a simple multi-layer model or direct measurements of the detector kernel could be carried out which forms the scope of our next chapter. Moreover, it could be additionally possible to implement a detector-specific tuning of the apodization function

of the FDK reconstruction [11], for example, by measuring the noise power spectrum of the detector to take into account the detector variability of noise levels.

Significant improvement in the quantitative reconstruction values for the homogeneous object like the iron gear for MeV data is obtained. We compared the CIVA kernels with the Penelope kernels as CIVA simulations have not been benchmarked for MV energy range. We observed discrepancy in CIVA and Penelope kernels mainly for the lower thicknesses. This discrepancy may be arising from the fact that CIVA does not take into account the photons produced after the Bremsstrahlung process. Whereas, the contribution of photons with Bremsstrahlung process may be self-attenuated at higher thicknesses, it can be important in the case of lower thicknesses. As a result, we observed that reconstructed results by CIVA and Penelope correspond to each other, apart from small differences at the edges of the object where lower thicknesses are present. The addition of the Bremsstrahlung process is currently under development in CIVA.

3.5 Chapter Summary

This chapter begins with defining the four-Gaussian model to be able to separate the contribution of the detector and the object scatter. Subsequently, the CBCT acquisition setups used for generating keV and MeV data are described in detail. To take into account the beam hardening effect, a fitting procedure to calculate the thickness at each pixel is described using the look-up table. An in-depth analysis of the four-Gaussian contributions is carried out in the results section for keV data. Experimental validation is then performed with both fan beam and cone beam geometries. Finally results obtained for MeV data are also shown in detail.

Chapter 4

Scatter correction using kernels combining measurements and Monte Carlo simulations

This chapter is based on the submitted publication, Bhatia et al. "Convolution-based scatter correction using kernels combining measurements and Monte Carlo simulations" JXST 2016

The results obtained in the last chapter prove that the correction of the scatter due to the object alone is not sufficient to completely remove scatter artifactS in the reconstruction. The scatter kernel calculation was performed using MC simulations. We remark that the detector scatter depends on several parameters including the spectrum used and components (front filter, back plate etc.) configuration of the detector and information about the component structure of the detector is kept undisclosed by the manufacturers. Therefore, to further improve the realism of the detector kernels, direct measurements of the detector kernel should be carried out which forms the scope of this chapter. In this chapter, we present an approach combining experimental data and Monte Carlo simulations to estimate the scatter kernels based on the continuously thickness-adapted kernels strategy based on a four-Gaussian modeling of kernels. We compare this approach with a pure experimental technique based on the two-Gaussian modeling of the kernels. The results obtained prove the superiority of four-Gaussian model to effectively take into account both the contribution of the object and the detector scattering as compared to the two-Gaussian approach. We also present parameterisation of the scatter kernels with respect to the magnification. This approach facilitates the use of a single geometry for calculation of scatter kernels over the whole magnification range of the acquisition set up.

Summary

4.1 Introduction

There are many deconvolution techniques based on calculation of kernels using Monte Carlo simulations [65][66][5][74][75]. The object scatter kernel modeling is usually proposed using a two-Gaussian model as in [5][76][77]. However, since the internal structure of the detector panel is mostly kept anonymous to the user, most of these methods do not take into account a realistic modeling of the flat panel detector leading to the calculation of only object scatter kernels. To tackle this issue, the use of experimentally calculated kernels [78][25][56] makes it possible to correct the scatter contributions due to both the object and the detector, without having to rely on an accurate 3D modeling of the detector. Kernels are usually derived from measurements using the slanted-edge method to compute the edge spread function (ESF) response. In these techniques, the scattered radiation is approximated by pencil-beam kernels with purely experimental [78] or analytically-fitted [25][56] models, and sometimes thickness-dependent [78]. Their results demonstrate that the contribution of scatter glare in the detector is important, the long-tails creating a modulation transfer function (MTF) drop in the low-frequency domain. Those analytical kernels involve a single exponential [25] or Lorentzian [56] model, the use of multiple terms in fitting the kernels being reported subject to instabilities for high-frequency components [56]. A single term in the analytical kernel model is however not able to discriminate the scatter contributions. Sun et al. [5] proposed to account for the detector scatter during the initialization with two Gaussian terms, but this preprocessing-step prior to the iterative SKS deconvolution might not be sufficient either to accurately model the detector kernel variability with respect to the object thickness, notably to take into account the hardening of the beam spectrum. The respective contribution of detector and object scatter in the kernels should be more clearly identified within the iterative deconvolution process, tuning the kernels according to the material thickness and the magnification when appropriate.

The overall scatter correction process requires correction from the scatter contribution of both the object and the detector. Whereas the object scatter can be accurately simulated using MC simulations, the detector compositions may not be accurately modeled in the simulations due to undisclosed model of the detectors by manufacturers. Therefore, experimental measurements are needed to accurately calculate the scatter kernels of the detector and to calibrate the weighting factor of the kernels.

We propose in this chapter to combine experimental measurements and Monte Carlo simulations to calculate the kernels of the two main scatter contributions, object and detector. We begin by describing a four-Gaussian modeling of the detector kernels calculated from joining experimental method and simulation. We then compare this approach with an experimental approach based on a two-Gaussian modeling of kernels. We further describe the method of parameterisation of scatter kernels over the magnification range. The acquisition set up and the material used are described in the next section. Finally the results obtained with the four-Gaussian model and the two-Gaussian model are compared for the reconstructions performed using classical FDK algorithm [11] with CIVA.

4.1.1 Combining experiment and simulation: Four-Gaussian model

The measured intensity I is the sum of primary intensity P and the scatter intensity S such that

$$I(x, y) = P(x, y) + S(x, y) \tag{4.1}$$

The scatter signal can be modeled as the sum of the scatter contributions from the object and the detector. For each contribution, a resulting kernel which has the weight of the scatter to primary ratio is determined. The total scatter signal S using the continuously-thickness adapted kernels [75] can then be modeled as:

$$S(x, y) = P(x, y) \otimes K(x, y, T) = P(x, y) \otimes (K_o(x, y, T) + K_d(x, y, T)) \tag{4.2}$$

where, $\otimes$ represents convolution and K is the thickness T dependent scattering kernel having its contribution from the object and detector scattering. Subscript d and o stand for the detector and the object respectively.

The scatter kernel can be rewritten as

$$K(x, y, T) = k(T)\, K^*(x, y, T) \tag{4.3}$$

where, the weight $k(T)$ to be applied to the unit-integral scatter kernel K^* is the sum of the weights from the object scattering $k_o(T)$ and the detector scattering $k_d(T)$ such that

$$k(T) = \iint K(x, y, T)\, \mathrm{d}x\, \mathrm{d}y = k_o(T) + k_d(T) \tag{4.4}$$

To determine the detector kernel $K_d(x, y, T)$, two setups were used in this study as described in figure 4.1. In the setup described in figure 4.1 a), a zirconium sheet of thickness 0.1 mm was placed with a tilt of around 5° on the aluminum slabs of different thicknesses assuming spatial isotropy. This setup provides the point spread function (PSF) after considering both object and detector scatter. In the second setup described in figure 4.1 b), the zirconium plate was placed directly on top of the detector. This setup provides the PSF after considering only the detector scatter. The ESF was first calculated for both the setups. In order to reduce the noise in the calculation of the ESF, one-hundred acquisitions were averaged out. A line spread function (LSF) can then be found from the derivative of the ESF.

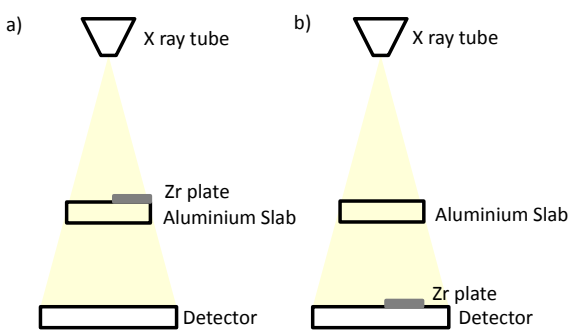

Figure 4.1: Schematic of the acquisition setup for the calculation of experimental kernels

The object scatter kernels $K_o(x, y, T)$ are determined by MC simulations as described in Bhatia et al. [75].

For both the acquisition setups (figure 4.1) and for each material thickness, the obtained LSF was fit using a two-Gaussian model [75], given as

$$LSF(x, T) = \sum_{i=1}^{2} A_i(T) \exp\left(-\frac{x^2}{2\sigma_i^2(T)}\right) \tag{4.5}$$

It should be noted that this two-Gaussian model is just to compute the weighting factor $k(T)$ and not to model the scatter kernels. The relationship between PSF and LSF is given as

$$LSF(x, T) = \int_{-\infty}^{\infty} PSF(x, y, T)\mathrm{dy} \tag{4.6}$$

Therefore, the PSF of the LSF of form given in equation 4.6 is

$$PSF(x, y, T) = \sum_{i=1}^{2} a_i(T) \exp\left(-\frac{x^2 + y^2}{2\sigma_i^2(T)}\right) \tag{4.7}$$

where $a_i(T) = \dfrac{A_i(T)}{\sqrt{2\pi\sigma_i^2(T)}}$

From the PSF corresponding to the setup depicted in figure 4.1 a) we have the following weight

$$W_a(T) = \iint PSF_a(x, y, T)\,\mathrm{d}x\,\mathrm{d}y \;\propto\; 1 + k_o(T) + k_d(T) \tag{4.8}$$

Similarly for the setup in figure 4.1 b) we have

$$W_b(T) = \iint PSF_b(x, y, T)\,\mathrm{d}x\,\mathrm{d}y \;\propto\; 1 + k_d(T) \tag{4.9}$$

Combining the integral of the PSF measurements for the two setups gives

$$\frac{W_b(T)}{W_a(T) - W_b(T)} = \frac{1 + k_d(T)}{k_o(T)} \tag{4.10}$$

The object weight factor $k_o(T)$ is calculated using MC simulations (CIVA) and therefore, the weight factor of detector $k_d(T)$ scatter can be calculated using

$$k_d(T) = \frac{W_b(T)}{W_a(T) - W_b(T)}\, k_o(T) - 1 \tag{4.11}$$

The final detector scatter kernels can then be calculated as

$$K_d(x, y, T) = (1 + k_d(T))\, PSF_b^*(x, y, T) - \delta[x, y] \tag{4.12}$$

where $\delta[x, y]$ is the Kronecker delta function and is null except for $x = 0$ and $y = 0$ where it is 1. Superscript * represents until normalized PSF.

Instead of using the Beer-Lambert law based on an effective linear attenuation coefficient μ, the thickness T at each pixel is directly computed from a look-up table f_{BH} – computed with CIVA for different slab thickness, that relates the true slab thickness with respect to the transmittance given by

$$T(x,y) = f_{BH}\left(\frac{P(x,y)}{I_o(x,y)}\right) \tag{4.13}$$

where I_o is the unattenuated image. It is worthy of note that the beam-hardening is taken care of with this procedure. The acquisition parameters and the material of the calibration slabs must be the same as the object under study. The directly transmitted primary fluency P was calculated for each thickness of the simulated slab. The thickness in terms of the transmittance $P(x,y)/I_o(x,y)$ is then calculated as described in section 4.3.1.

The final scatter kernels were then fitted with a four-Gaussian model as follows

$$K(x,y,T) = \sum_{i=1}^{2} w_{d,i}(T)\exp\left(-\frac{x^2+y^2}{2\sigma_{d,i}^2(T)}\right) + \sum_{i=1}^{2} w_{o,i}(T)\exp\left(-\frac{x^2+y^2}{2\sigma_{o,i}^2(T)}\right) \tag{4.14}$$

where,

$$k_d(T) = 2\pi(w_{d,1}(T)\sigma_{d,1}^2(T) + w_{d,2}(T)\sigma_{d,2}^2(T)) \tag{4.15}$$

and

$$k_o(T) = 2\pi(w_{o,1}(T)\sigma_{o,1}^2(T) + w_{o,2}(T)\sigma_{o,2}^2(T)) \tag{4.16}$$

For generating the continuous map [75] of kernels, the amplitude parameters, w_d and w_o and the shape parameters σ_d and σ_o were also fit with respect to the thickness of the object.

The schematic representation of the projection wise scatter correction process by comibination of MC simulations and experiments is shown in figure 4.2

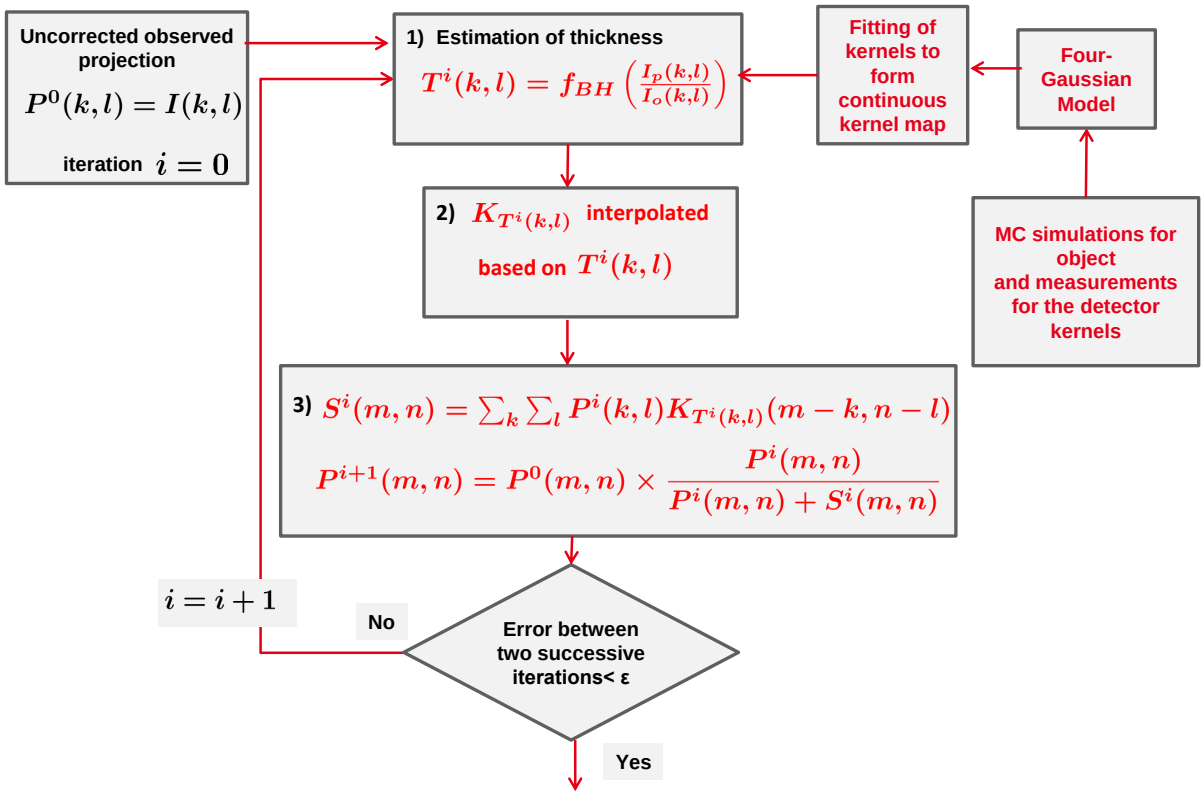

Figure 4.2: Schematic representation of the projection wise scatter correction process by combination of MC simulations and experiments. The modifications with respect to discrete approach by Sun et al. [5] are shown in red.

4.1.2 Parameterisation of the kernels in terms of the distance

Acquisitions to calculate the scatter kernels can be tricky and time consuming for different sets of geometrical conditions. We propose a practical solution to correct the scatter over the whole magnification range by parameterisation of object scatter kernels over the distance between the center of the object (where the rotational axis lies at the center of the object) and the detector. We call this distance d_{OD} for future reference. For this, we propose to acquire the detector kernels using the setup in figure 4.1 b) assuming that the detector kernels do not vary over the magnification. We then fit the parameters of the simulated object kernels over d_{OD}. Objects in the case of kernels calculations, refer to the slabs which are centered on the rotation axis.

The amplitude parameters of the object scatter kernels are expected to decrease over the increase in d_{OD} whereas kernel widths, given by sigma, of the two Gaussians are expected to increase over d_{OD}: the object scattering kernels progressively become flatter.

We describe these parameters as a power function of the distance d_{OD} as:

$$p(T, d_{OD}) = p(T, 0) d_{OD}^{\alpha} \tag{4.17}$$

where $p \in \{w_{o,1}, w_{o,2}, \sigma_{o,1}, \sigma_{o,2}\}$ is any of the thickness T dependent parameters of the object scatter kernels. We expect the parameter α to be negative in case of amplitude parameters and positive in the case of standard deviation parameters.

4.1.3 Experimental approach: two-Gaussian model

In order to form a pure experimental approach, we calculated the weight factor $\bar{k}(T)$ using the ratio of experimental transmittance and theoretical transmittance calculated by the Beer-Lambert law, giving

$$\bar{k}(T) = \frac{E_{trans}(T)}{T_{trans}(T)} - 1 \tag{4.18}$$

where, $E_{trans}(T)$ represents the experimental transmittance obtained from experimental kernels and $T_{trans}(T)$ is the theoretical primary transmittance calculated according to the Beer-Lambert law.

The experimental transmittance was calculated corresponding to the setup shown in figure 4.1 a) such that

$$E_{trans}(T) \propto \frac{W_a(T)}{W_a(0)} \propto \frac{1 + k_o(T) + k_d(T)}{1 + k_d(0)} \tag{4.19}$$

Therefore in reality, using equation 4.18, $\bar{k}(T)$ corresponds to

$$\bar{k}(T) = \frac{k_o(T) + k_d(T) - k_d(0)}{1 + k_d(0)} \tag{4.20}$$

Therefore, to compute an estimate of the kernel weight $k(T)$ using a solely experimental approach, the kernels weight of the detector scatter without object $k_d(0)$ must be assumed to be negligible.

The final kernels of the setup in figure 4.1 a) were then fitted with a two-Gaussian model as

$$K(x, y, T) = w_{d,1}(T) \exp\left(-\frac{x^2 + y^2}{2\sigma_{d,1}^2(T)}\right) + w_{o,1}(T) \exp\left(-\frac{x^2 + y^2}{2\sigma_{o,1}^2(T)}\right) \tag{4.21}$$

where,

$$\bar{k}(T) = 2\pi(w_{d,1}(T)\sigma_{d,1}^2(T) + w_{o,1}(T)\sigma_{o,1}^2(T)) \tag{4.22}$$

The result obtained with this method was compared with the results obtained using the four-Gaussian model described in section 4.1.1.

4.2 Material

The acquisition setup mainly consisted of an X-ray source, an object rotational table and a flat panel detector. The X-ray source unit with 150 kV voltage, 750 µA current and the focal size of around 120 microns was used. Filtration consisted of a 0.3 mm aluminium inside the tube and a 1.5 mm external aluminium filter. Figure 4.3 shows simulated spectrum with internal and external filters at 150 kV source voltage. Figure 4.4 shows the variation of the mass attenuation coefficient of aluminium over the energy. The data was taken from NIST tables [2]. The flat panel detector used had an array size of 1024 × 1024 with 0.2 mm of pixel size.

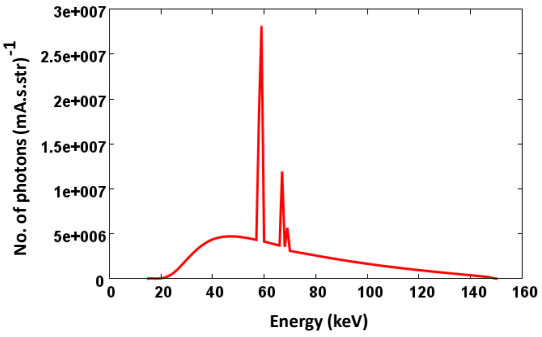

Figure 4.3: Simulated spectrum with internal and external filters at 150 kV source voltage with MCNP [7].

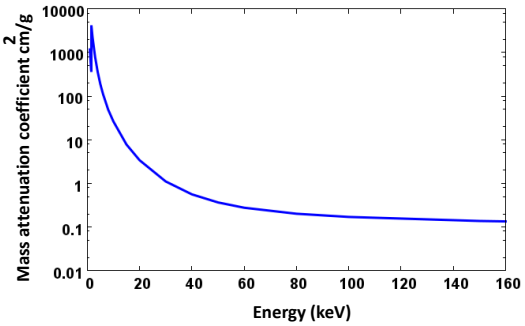

Figure 4.4: Variation of mass attenuation coefficient of aluminium over energy [2]

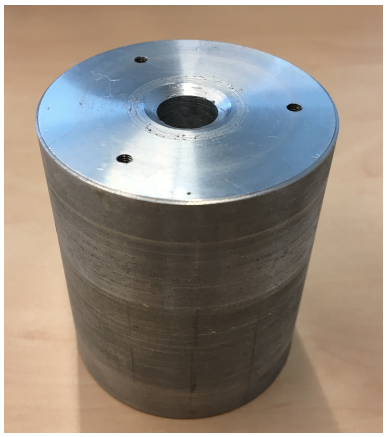

Figure 4.5: Picture of the aluminium cylinder with one central air insert (10 mm diameter) and three peripheral air inserts (3 mm diameters)

Acquisitions were performed on an aluminium cylinder as given in figure 4.5 with a diameter of 60 mm. The aluminium cylinder consisting of one central air insert (10 mm diameter) and three peripheral air inserts (3 mm diameters).

Two different magnification setups were used in order to validate the parameterisation of kernels in terms of different d_{OD}. In the first case, d_{OD} was 95 mm, whereas in the second case it was 295 mm. The source to detector distance was kept 600 mm in both cases.

4.3 Results

4.3.1 Fitting of calculation of thickness: Beam-hardening correction

In order to calculate the thickness at each pixel, simulation was performed with slabs of different thicknesses. The directly transmitted primary fluency P was calculated for each thickness of the simulated slab. The thickness vs transmittance LUT f_{BH} given in equation 4.13 has been calculated using least square fitting as shown in figure 4.6. The classical thickness determination based on the effective linear attenuation coefficient is also shown by the blue curve in figure 4.6. The beam-hardening, although not really strong, is taken care of with this procedure. Equation 4.23 gives the relationship of thickness T value in terms of transmittance $P(x,y)/I_o(x,y)$.

$$\begin{aligned} T(x,y) &= f_{BH}\left(\frac{P(x,y)}{I_o(x,y)}\right) \\ &= b\left(\log\left(\frac{P(x,y)}{I_o(x,y)}\right)\right) + c \end{aligned} \tag{4.23}$$

using $b = -14.1$, $c = 1.14$

Table 4.1: Table summarizing the calculated weighting factor $k(T)$ and $k_d(T)$ using PSF areas $W_a(T)$ and $W_b(T)$ and the simulated weighting factor $k_o(T)$ for object kernels of different thicknesses

Thickness(mm)	$W_a(T)$ (pixel^2)	$W_b(T)$ (pixel^2)	$k_o(T)$	$k_d(T)$	$k(T)$
10	1867	1760	0.12	0.99	1.12
26	621	555	0.32	1.68	2.00
42	587	493	0.70	3.27	3.02
58	955	807	1.10	4.99	6.10

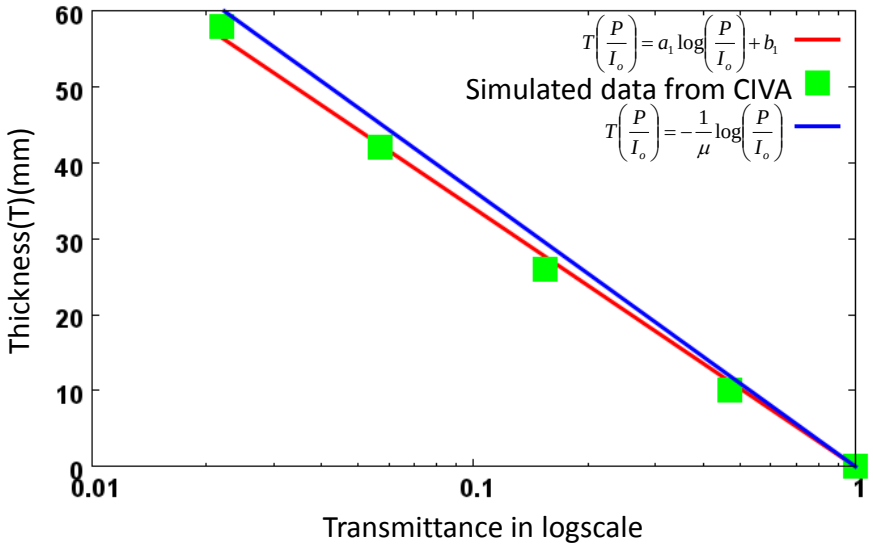

Figure 4.6: Thickness (in mm) vs transmittance: MC simulations (green squares), fitted model (red curve) and monoenergetic curve (blue line)

4.3.2 Four-Gaussian model

Table 4.1 gives the calculated weighting factor $k(T)$ and $k_d(T)$ using the PSF areas $W_a(T)$ and $W_b(T)$ and the simulated weighting factor $k_o(T)$ for object kernels of different thicknesses using equation 4.11.

The scatter kernel fitting using the four-Gaussian model in comparison to the two-Gaussian model, can separate the low frequency contribution of scatter due to the object and the high frequency contribution of the detector. Moreover, we observed that the two-Gaussian model is not sufficient to fully take into account the contribution of the lower frequency scatter from the object. Table 4.2 shows a comparison of the fitting parameters for the two slab thicknesses (10 mm and 42 mm) with the two-Gaussian model and the four-Gaussian model for the combined (detector and object) scatter kernels, both simulated with CIVA. It also displays parameters object scatter kernels alone. We notice that the two-Gaussian model only provides the amplitude parameters $w_{(d,1)}$ and $w_{(d,2)}$ and neglects the contribution of the parameters $w_{(o,1)}$ and $w_{(o,2)}$, which actually correspond to the object scatter kernels. We also notice the underestimation of CIVA detector modeling as compared to the real experimental measurements.

Table 4.2: Simulated kernels with CIVA: Comparison of the fitting parameters for the two slab thicknesses (10 mm and 42 mm) with the two-Gaussian model and the four-Gaussian model for combined detector and object scatter kernels obtained with CIVA. Table also displays the parameters of the object scatter kernels alone. All the values of σs are in pixels and amplitude factors w are in pixel^2

Thickness (mm)	Model	Detector				Object			
		$w_d(1)$ $\times 10^{-3}$	$w_d(2)$ $\times 10^{-1}$	$\sigma_d(1)$	$\sigma_d(2)$ $\times 10^{-1}$	$w_o(1)$ $\times 10^{-4}$	$w_o(2)$ $\times 10^{-4}$	$\sigma_d(2)$ $\times 10^{1}$	$\sigma_d(2)$ $\times 10^{1}$
10	Two-Gaussian	0.085	4.5	2.1	4.7				
	Four-Gaussian	0.076	4.2	2.5	4.8	0.27	2.0	1.0	2.9
	Two-Gaussian					0.25	1.8	1.0	2.9
46	Two-Gaussian	1.8	1.3	4.6	4.8				
	Four-Gaussian	1.7	1.2	4.6	4.9	1	2.6	1.9	4.8
	Two-Gaussian					1	2.7	2.1	5.0

The noise level in the experimentally obtained LSF with the setup shown in figure 4.1 a) is high even after averaging over a hundred acquisitions, due to the noise coming from various sources such as quantum and electrical. Moreover, the output of the flat panel detector is limited by its optical transfer function. Therefore, we have designed the four-Gaussian model by a two Gaussian fitting of experimentally obtained detector kernels using the setup described in 4.1 b) and a two-Gaussian fitting of the object scatter kernels obtained from CIVA simulations. Figure 4.7 shows the experimentally calculated detector kernels and figure 4.8 shows the parameters of the fitting for the detector kernels. Figure 4.9 shows the simulated object kernels and figure 4.10 shows the parameters for the simulated object scatter kernels.

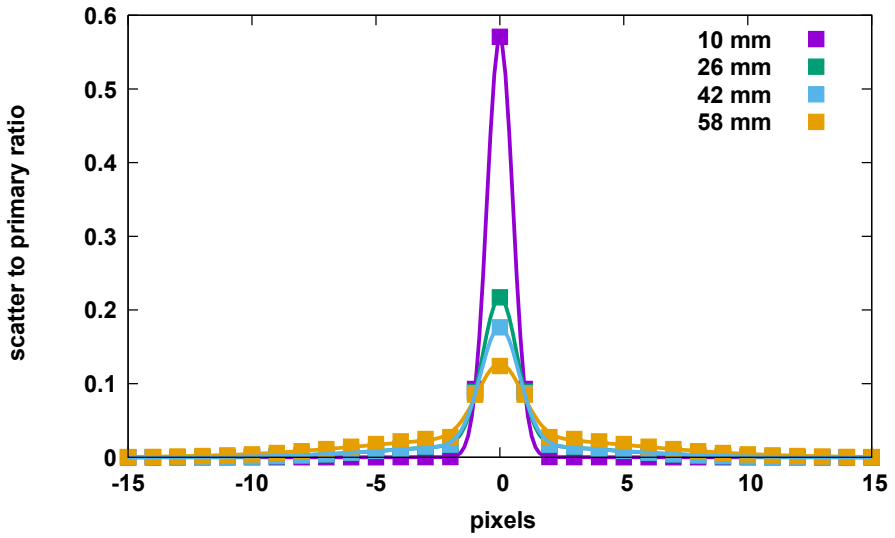

Figure 4.7: Plot profile of experimental detector kernels for different thicknesses for the setup in figure 4.1 b)

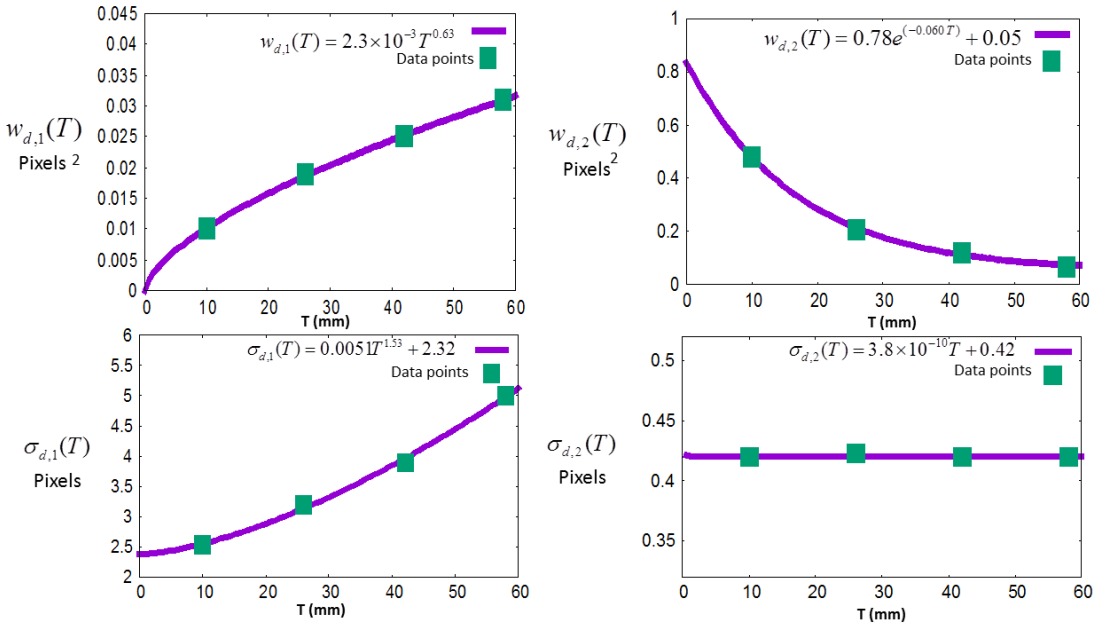

Figure 4.8: Fitting parameters of the experimental detector kernels using two Gaussian with respect to the thickness for the setup in figure 4.1 b)

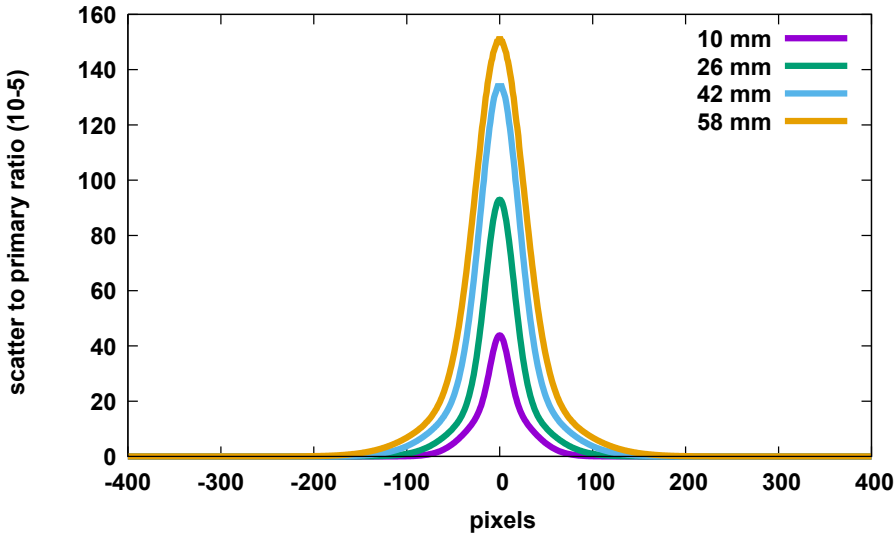

Figure 4.9: Plot profile of the simulated object kernels for different thicknesses

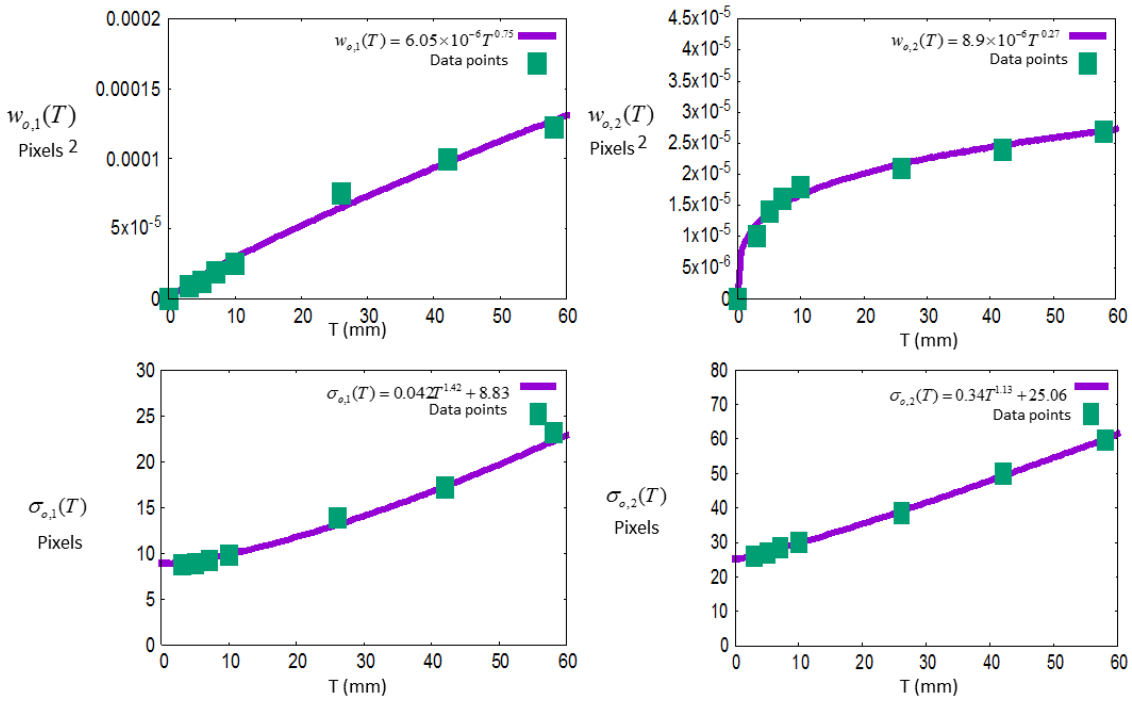

Figure 4.10: Fitting parameters of the simulated object scatter kernels using the two Gaussian terms with respect to the thickness

4.3.3 Two-Gaussian model

As described in section 4.1.3, the weighting factor $\bar{k}(T)$ for each thickness of the slab is calculated using the experimental transmittance $E_{trans}(T)$ and the theoretical transmittance $T_{trans}(T)$ using equation 4.18. To form a continuous map for the application of continuous approach, $\bar{k}(T)$ was parametrized over the whole thickness range shown in figure 4.11. Figure 4.12 shows the plot profile of the experimental kernels derived for the setup in figure 4.1 a) for different thicknesses of aluminium slabs. The corresponding fitted parameters are plotted in figure 4.13.

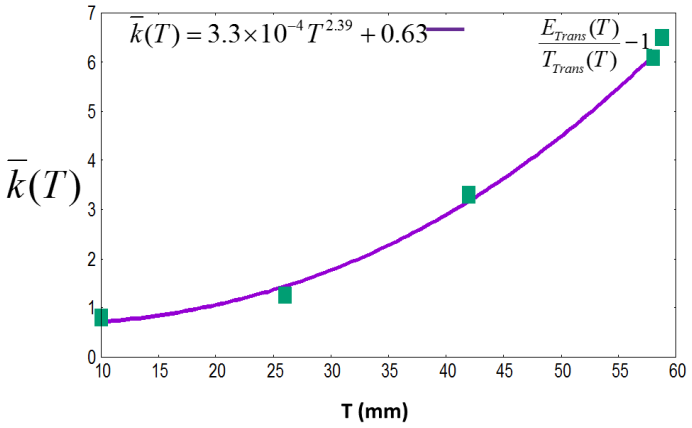

Figure 4.11: Continuous map of $\bar{k}(T)$ over the thickness calculated from the experimental transmittance and the theoretical transmittance

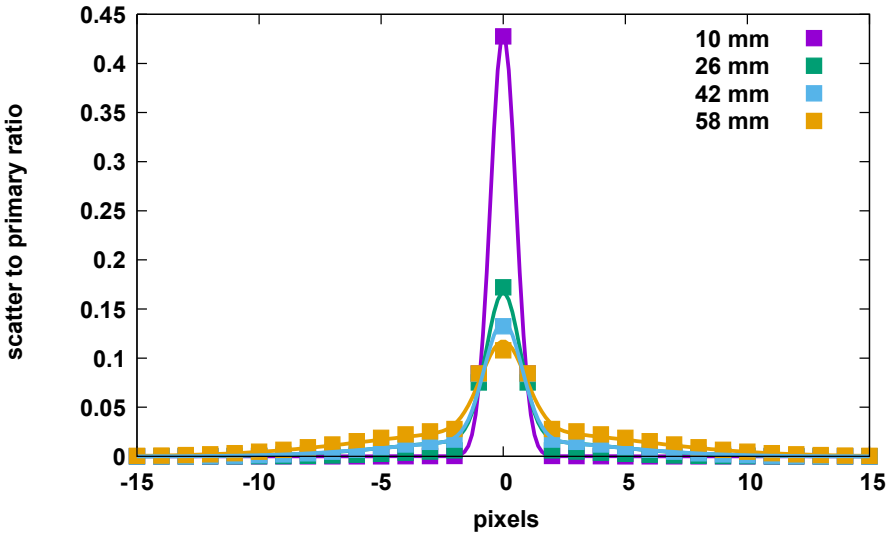

Figure 4.12: Plot profile of the experimental kernels for different thicknesses for the setup in figure 4.1 a)

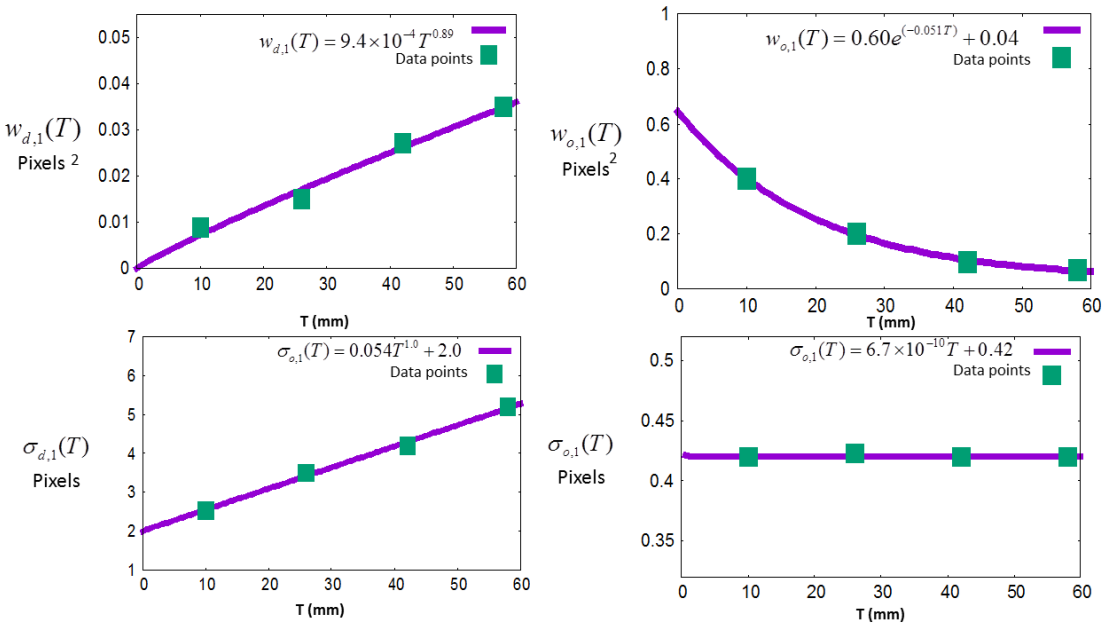

Figure 4.13: Fitting parameters of the experimental detector kernels using two Gaussian terms with respect to the thickness for the setup in figure 4.1 a)

4.3.4 Parameterisation of the kernels with respect to distance

As described in section 4.1.2, we propose a parameterisation of the kernels in terms of d_{OD} in order to facilitate the use of a single geometry for the calculation of the scatter kernels over the magnification range of the acquisition setup. Figure 4.14 shows the object scatter kernels for a 10 mm aluminium slab for different d_{OD}. In figure 4.14, the kernels are normalized to the peak of kernel for $d_{OD} = 95$ mm.

Figure 4.15 gives the fitting of the parameters of the object kernels for 10 mm slab over d_{OD}. The parameters were fitted in as power functions in terms of d_{OD} as given in equation 4.17. We used four data sets of d_{OD} to perform this parameterisation. Figure 4.16 shows the relative absolute error in percentage between the simulated kernels and the parameterised kernels.

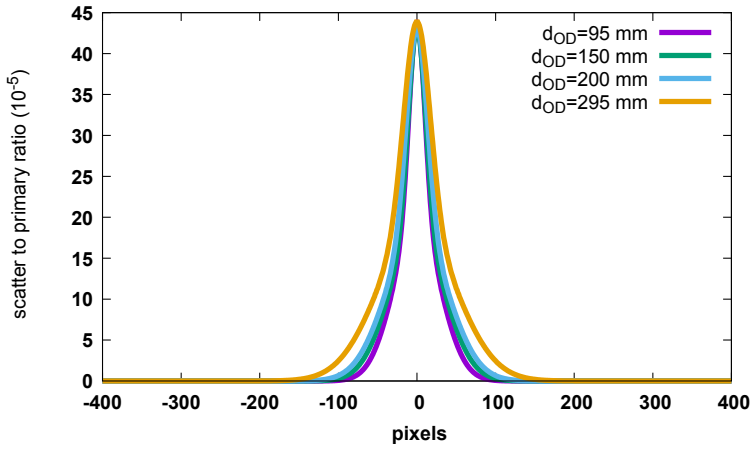

Figure 4.14: Normalized object scatter kernels over different object to detector distances for the $T = 10$ mm aluminium slab simulated with CIVA

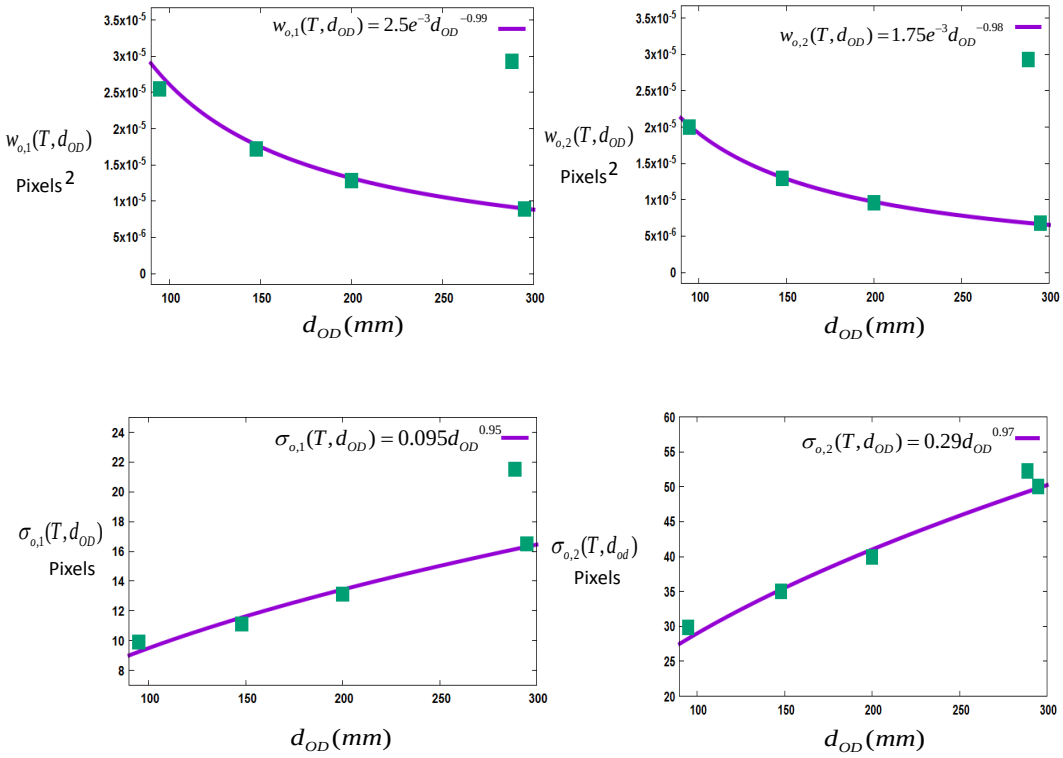

Figure 4.15: Fitting of parameters of the object scatter kernel for the $T = 10$ mm slab over the object-detector distance

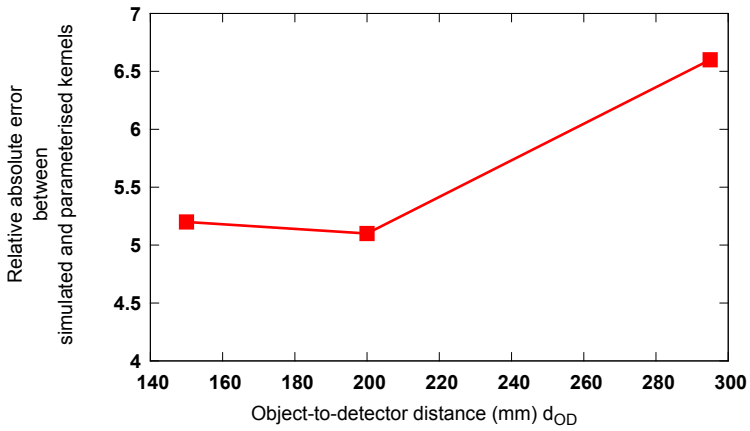

Figure 4.16: Relative absolute error between the simulated kernels and the parameterised kernels for the $T = 10$ mm slab

4.3.5 Scatter correction on the aluminium cylinder

Figure 4.17 a) shows the reconstruction obtained with the uncorrected projections. In figure 4.17 b) we show scatter correction result using kernels calculated with just MC simulations in CIVA. Figure 4.17 c) shows the scatter correction result with the combined model of simulation and experiments for kernel calculation. On comparison in later two we clearly see that combined simulation and experiments results in better

scatter correction than pure simulation as is also evident in the plot profiles in figure 4.18.

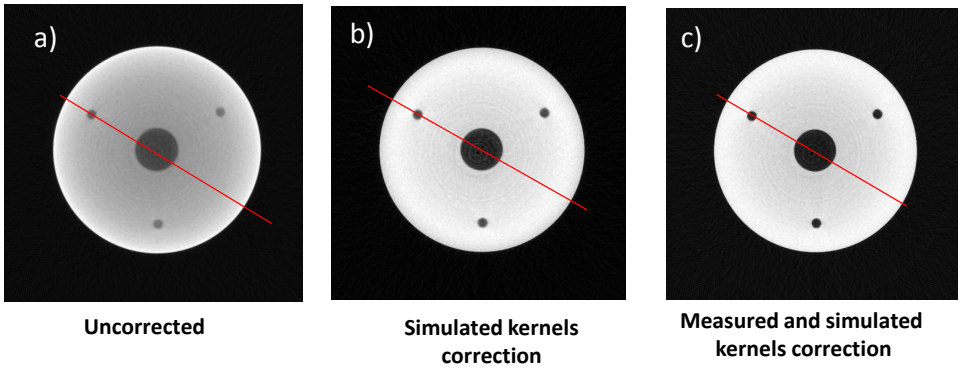

Figure 4.17: Reconstruction slice with a) uncorrected projections b)correction performed by simulated kernels c) correction performed by kernels calculated combining simulations and experiments

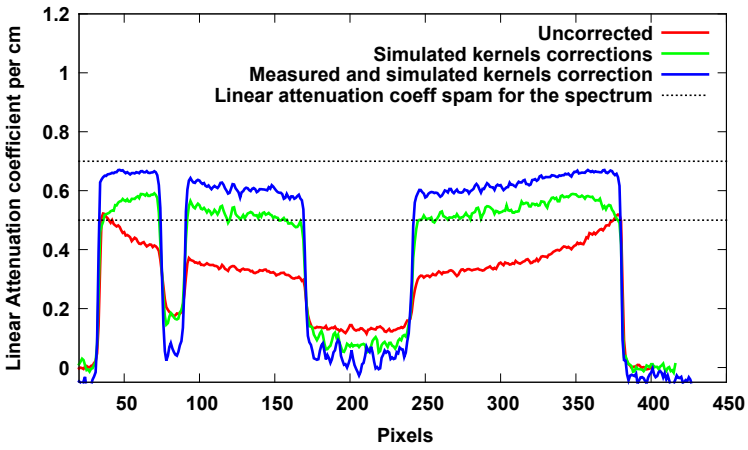

Figure 4.18: The plot profiles of the corrected and uncorrected reconstructions

Figure 4.19 a) shows the reconstruction obtained with the uncorrected projections. The red curve in the figure 4.20 shows the plot profile of this reconstruction with a clearly visible cupping effect. The green curve in figure 4.20 shows the result obtained with only beam hardening correction. Figure 4.19 b) shows the reconstruction obtained after scatter and beam hardening correction using the two-Gaussian model and figure 4.19 c) shows the reconstruction obtained after scatter and beam hardening correction using the four-Gaussian model.

The plot profiles of the reconstructions obtained after correction with the two-Gaussian and the four-Gaussian models are also shown in figure 4.20.

Table 4.3 displays the mean and the standard deviation of the reconstructed values for corrected and uncorrected data, in both air and aluminium region calculated using

binary masks. Uncorrected value of 0.41 cm^{-1} for the linear attenuation coefficient of aluminium is estimated. By using the two-Gaussian model, we obtain a value of 0.55 cm^{-1} for the linear attenuation coefficient of aluminium. In the considered energy range ($E \in$ [64 keV, 94keV]), the value of the linear attenuation coefficient for aluminium lies between 0.5 cm^{-1} at 64 keV and 0.7 cm^{-1} at 94 keV. The relative absolute error in percentage is approximately 10% for the two-Gaussian model. Whereas, with the four-Gaussian model, we obtain a value of 0.62 cm^{-1} for the aluminium. The relative absolute error is reduced to 3.4%.

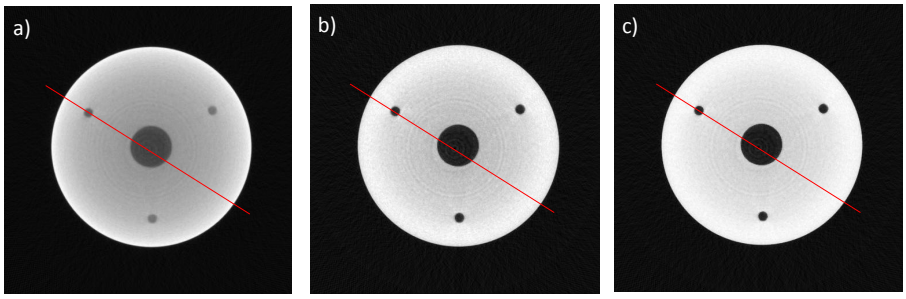

Figure 4.19: Reconstruction slice with a) uncorrected projections b) scatter and beam hardening corrected projections using the two-Gaussian model c) scatter and beam hardening corrected projections using the four-Gaussian model

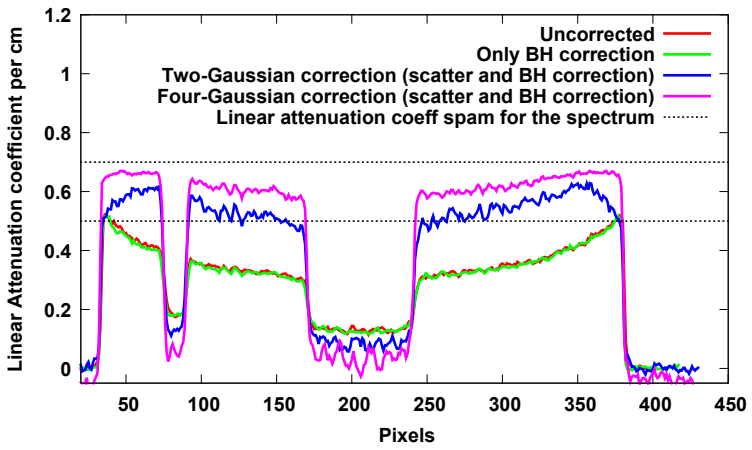

Figure 4.20: The plot profiles of the corrected and uncorrected reconstructions

Table 4.3: Mean and standard deviation values for aluminium and air region for uncorrected and corrected reconstruction slices

		mean (cm^{-1})	std. dev.
Uncorrected	air	0.132	± 0.002
	aluminium	0.413	± 0.007
Two-Gaussian correction	air	0.062	± 0.006
	aluminium	0.552	± 0.005
Four-Gaussian correction	air	0.060	± 0.006
	aluminium	0.622	± 0.009
Mean spectrum value	air	0.000	
	aluminium	0.614	

Figure 4.21 shows the reconstruction obtained with simulated object kernels and the parameterised object kernels with respect to object-to-detector distance in the four-Gaussian model. Figure 4.22 shows the plot profile of these two reconstructions.

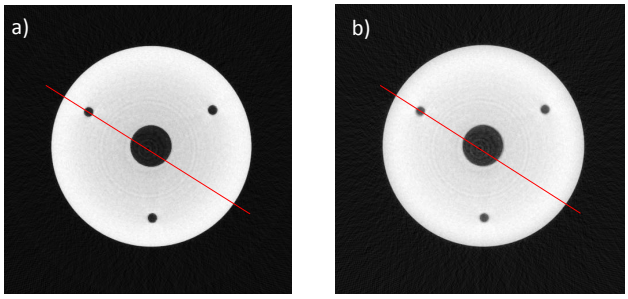

Figure 4.21: Reconstruction slice with a) simulated object kernels b) parameterised object kernels

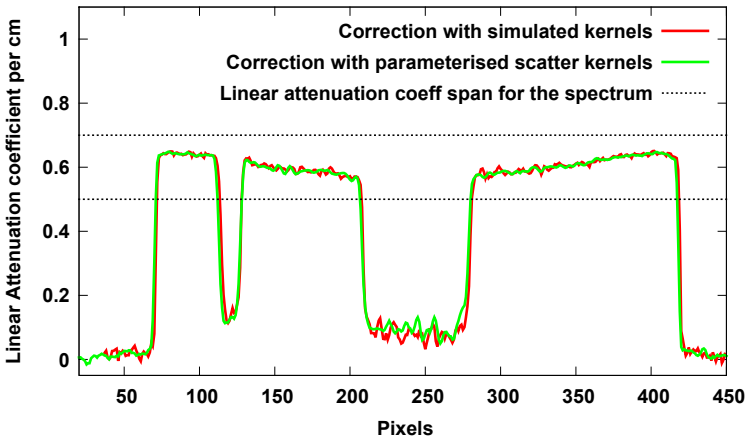

Figure 4.22: The plot profiles of the corrected reconstructions with simulated object kernels and parameterised object kernels

4.4 Discussion

This chapter presents a combination of experiments and simulations to calculate the scatter kernels for SKS method. The simulation of detector geometry is often tricky due

to the lack of sufficient information of the detector geometry. Therefore, this chapter presents an approach to calculate the detector PSF using experiments which takes into account this limitation of the MC simulation. Another important result presented in this chapter is the thickness dependency of the PSF of the detector. The weighting factor of the detector kernels is not a single constant, as assumed in most of the previous studies, but rather it is a function of the thickness of the object thickness present in front of the detector. This is due to the change in the spectrum by the presence of the object thickness. This is also evident from the variation of the parameter $\sigma_{d,1}$ related to the width of the detector kernel, with the thickness of the object (figure 4.8).

We have shown the comparison of a four-Gaussian model with a classical the two-Gaussian model of the scatter kernels. It shows that the four-Gaussian model clearly takes into account both the contribution of object and detector scattering whereas in the two-Gaussian model, the object contributions are not well taken into account. This results in a better reconstruction with the four-Gaussian model as compared to the two-Gaussian model.

Moreover, with the parameterisation of kernels with respect to the object-to-detector distance, only one set of kernels for a particular magnification are sufficient to recover the scatter corrected projections acquired at different setup geometries. We notice the effect of blurring in the kernels over the increase in object detector distance. This effect is also clear in the fitting of the parameters of the kernels, where the amplitude factors of the kernels decrease over object detector distance whereas the width of the two Gaussians increases as a power function of the object-to-detector distance.

The effect of beam hardening is insignificant in this case and the improvement of the cupping effect is thus limited if only the correction of beam hardening is considered. This can be explained by the fact that, with the filtration used, the X-ray spectrum, mainly lies within the energy of 25 keV to 120 keV. In this energy range, the linear attenuation coefficient of aluminium is almost steady subsequently leading to a minute beam hardening effect. However, we can also point out that the still remaining cupping artifact after correction can come from not so accurate modeling of the spectrum, which in that case, may produce the remaining beam hardening effect. We also observe that in the same energy range, if a material with high Z material, is used the variation in its linear attenuation coefficient is higher due to the higher probability of the interaction of photons in photoelectric domain. Moreover, in this energy range scatter correction of multi-material object is difficult because the probability of interaction is not dominantly Compton especially for high Z. Therefore, the likelihood of interaction is not just proportional to electron density and is dependent on the atomic number of the material.

4.5 Chapter Summary

In this chapter we presented, a combination of the experimental and simulation approach to form the scatter correction model. This approach solves the issue of inaccurate modeling of the detector using only simulations due to the lack of information of the detector geometry. A combination of experimental and simulation approach using a four-Gaussian model was compared with a pure experimental approach using a two-Gaussian model. The results obtained prove the accuracy of four-Gaussian model

over the two-Gaussian model in taking into account both the contribution of the object and the detector scatter. The results obtained also prove that the calibrated weighting factor of the detector kernels is not a single constant as assumed in most of the previous literature, but is a function of the object thickness present in front of the detector. This is due to the change in the spectrum by the presence of the object thickness.

Chapter 5

Conclusions and Perspectives

In this thesis, we first presented a comprehensive review of many of the scatter artifact correction techniques adopted in CBCT providing their advantages, disadvantages and scope of applications. The techniques are broadly divided into two sections of pre-processing and post-processing on the measured images. This comprehensive review demonstrated that presently SKS method gives a good compromise on the efficiency, the computation cost and the ease of implementation among all the methods described. Their applicability over a wide range of imaging conditions gives users an added advantage. Moreover, since no extra hardware is required by this approach, it forms a major advantage specially in those cases where experimental complexities must be avoided.

The main limitation of the SKS model comes from its limited efficiency in calculating effectively the distribution of scattering for complex geometries. Several modifications in SKS method have been adapted to solve this issue which includes the use of non-stationary kernels or free parameter adjustments for the kernels. However, for higher SPR that is often experienced in industrial energy, the different steps of the SKS correction algorithm have to be reconsidered while forming the scatter kernel parameterisation. In particular, a better sampling of the kernels with respect to the thickness of the object is required to get an accurate model of the variability both in shape and amplitude of the scatter kernels over the whole thickness range.

We propose an analytical parameterisation of the scatter kernel which are derived in terms of material thickness, to form continuously thickness-adapted kernel map. This approach proved to be efficient to produce better sampling of the kernels with respect to the thickness of the object. As a result, both the amplitude and the shape distribution of the scatter can be effectively calculated for complex geometries. The scatter corrections are performed using this approach and the results obtained are compared with the classical approach. The scatter correction with this novel approach produces better reconstruction values especially at the edges of the object where the variation in the object thickness is higher. As a result, the reconstruction values obtained from this method are also better than the classical approach. This method was also applied to a multi-material object, in the case when the energy range used is such that the dominant process of interaction is Compton scattering, which is mostly the case with NDT. In this energy range, the kernels for a particular thickness of a material do not depend on the atomic number of the material, but only on its electron density. Therefore, the equivalent thickness of different materials can be chosen for multi-material

corrections. Moreover, we implemented a multiplicative iteration approach to tackle the problem of negative estimates for the primary within the iteration process, which can be a possibility with higher SPR experienced in the energy range used. This work has led to a published journal article [75] in NDT&E International in the year of 2016. We had also published a conference article in the International Symposium on Digital Industrial Radiology (DIR) and Computed Tomography in the year of 2015 [83].

Most of the studies for the scatter correction in CBCT have emphasis given to mainly the object scatter contribution. In this thesis, we also performed a comprehensive evaluation of the contribution of the detector scattering. Since the scatter contributions from the detector and the object are entangled, it makes the parameter fitting of the continuous model tricky. Moreover, we noticed that the high frequency contribution of the detector scatter generates a strong peak in the center pixel of the detector where the pencil beam is impinged. This shape needed for the necessity to explore an increase in order of the Gaussian model.

Therefore, we improved on the model fitting of the continuous model and proposed to identify the respective scatter contributions of the object and detector using a four-Gaussian model to have a more accurate modeling. A first approach was performed using just MC simulations for calculating the scatter kernels for the detector and the object. The scatter correction performed in the case of our study proved that a major contribution of scattering came from the detector. The results obtained were also validated experimentally using a collimator slits setup. This work has been published in an another journal, JXST in the year of 2016 [84].

The scatter correction performed on the basis of simulations may not accurately model the detector geometry, as the modeling of the detector is only based on an approximate model of the detector. However, the scatter correction was still noteworthy taking into account both the detector and the object scattering. To further improve our approach in calculating the detector scatter contribution, we used experiments to calibrate the weights of the scatter kernels due to the detector. The results obtained in this study, also prove that a significant contribution of scattering came from the detector. Moreover, an important result presented is that the PSF of the detector is spectrum dependent which in turn depends on the object thickness present in front of the detector. Most of the studies that have been performed with regard to the detector scattering had taken the PSF of the detector to be a constant which is not the case as proved by our results. This work has also been submitted in the journal NDT&E and is currently under review [85].

In this study we aimed to develop a scatter correction scheme which is flexible and adaptable to many different users working with different conditions. The objective was to evaluate the contribution of the scattering from the object and the detector that is used commonly in industrial CBCT and to be able to propose a method of correction which is suited for over a wide range of energy. Using this method, scatter correction can be performed, in a much efficient manner by using MC simulation (if available to the user) or by experimentally calculating the scatter kernels by using simple set ups. The parameterisation of kernels both in terms of the thickness of the object, as well as the distance between the object and the detector, offers corrections for complex geometries using simple acquisition setups.

5.1 Perspectives

This scatter correction process is much faster than the MC estimation of the scatter that is already present in the software CIVA. The MC estimation of scatter is limited by the simulated data produced inside CIVA. A work is currently in progress to implement our method into CIVA, as it supports experimental data and produces results quicker. The addition of the Bremsstrahlung process has been reported to the developers and the work is under process.

Even after performing the scatter correction, we observed remaining cupping effects in some of the reconstructed images. One explanation to these remaining artifacts could be the mismatch of the simulated spectrum with the experimental spectrum used for acquisition of data or during the calculation of scatter kernels. Due to this mismatch, the remaining beam hardening may not be taken into account by the procedure followed for its correction. We point out that, in this study, no calibration procedure has been followed for the input spectrum. One way of removing these remaining artifacts could be the calibration of beam input spectrum based on methods like half-value layer etc. with the source model [86][87][88] and without the source model by using transmission measurements [89]. This forms the scope of future study.

Another important aspect of future study, is to individually study the various contribution of scatter originating within the detector, such as the effect of back-scattering from the back-plate of the detector, the contribution of the X-ray fluorescence photons and the glare produced by the optical photons. This type of evaluation can provide knowledge about the major contributor of scatter inside the detector. We show in the last chapter that one of the two parameters of the width of the Gaussian model of the detector kernels varies over the thickness of the object and does not remain constant. We note that with more hardened energy, due to the increasing thickness of the object, more photons reach the back-plate of the detector. But at the same time, a reduced number of photons should be back-scattered with this increase in energy of the photons. Therefore, it becomes important to study in detail, the compensation factor of these two effects due to hardened energy of photons. This type of study will also help in the development and the understanding of a better geometrical model of flat panel detectors which are employed in industrial CBCT.

In this study, some invariance of the kernels has been assumed. For example, in the calculation of beam hardening through LUT, spatial variability of the spectrum with respect to the position may be present owing to processes such as heel effect. Moreover, the energy distribution varies with the position of the beam, due to beam softening laterally and hardening longitudinally. This effect may also bring spatial variability in the scatter kernels. Additionally, the tilting of the kernels with respect to the divergence of the beam was observed [90]. Moreover, in the calculation of the kernels, we could take into account the non-uniformity due to the structure and the edges of the detector design. A further scope of study could be to take these spatial variability of the kernels into account during the modeling of the kernels.

Our approach of continuously thickness-adapted kernels takes into account the local thickness variability in the object due to fine sampling of kernels with respect to the thickness of the object. Sun et al. [5], adapted kernel asymmetry to produce a better modeling of the kernels, especially for the edges of the object. This adaptation of the asymmetry of the kernels could have been important due to the crude sampling of

the kernels used in their method. Moreover, their asymmetric adaptation is based on the assumption of water-like object and the stretching parameters in the asymmetric kernel formulations are limited to the first-order scattering. If higher-order scattering is present, as is the case in the industrial energy, the formulation of the asymmetric kernels may not be trivial as in their case. Moreover, asymmetry of the kernels may not be as important now, with the fine sampling of the kernels used in the continuous approach since the edges of the objects have been already well recovered. The validation of this point remains as a scope of further study.

If we go beyond a few tens of MeV energy, like in the applications of cargo screening at the airports, Compton interaction is not the dominant interaction any more. The probability of interaction in this region of energy varies to the square of atomic number, Z for pair production. It is no more independent of Z as in the case of Compton interaction. In that case, we cannot assume equivalent thickness hypothesis for the selection of kernels for multi-material objects. Future work can focus on addressing this issue of object heterogeneity in this higher energy range.

Appendix A

Résumé du travail de travail

A.1 Introduction

Dans ce chapitre en français, nous présentons de manière synthétique le travail effectué dans le cadre de cette thèse. Le lecteur intéressé par de plus amples détails pourra se référer aux différents chapitres suivants rédigés en anglais.

A.2 Contexte

La tomographie par rayons X à faisceau conique ou Cone Beam Computed tomography (CBCT) est une technologie d'imagerie utilisée dans le domaine médical ainsi que domaine industriel pour reconstruire en 3 dimensions un objet d'étude. La reconstruction en 3 dimensions de la géométrie de l'objet est réalisée en effectuant un traitement numérique sur un grand nombre d'images en 2 dimensions prises autour de l'objet soit sur un tour complet autours de l'objet ou sur des angles de rotation limité grâce au récents progrès dans le domaine. Le lecteur intéresse pourra se rapporter au chapitre 1 pour ce plus ample détails sur l'étude bibliographique proposé dans ce manuscrit.

La figure A.1 montre la géométrie standard définie dans CBCT avec un faisceau conique de rayons X source et détecteur plan (ou Flat Panel Detector FPD) tournant autour de l'axe de rotation passant par l'objet à l'étude. Une source émet un faisceau de rayons X conique qui se propagent à travers un objet. Le faisceau est plus ou moins atténué par l'objet. Le faisceau de rayons X transmis dernière l'objet permet de réaliser l'acquisition d'une projection de l'objet sous un angle d'acquisition donné. Cette forme conique du faisceau se distingue de la géométrie en éventail que l'on retrouve de manière classique dans les scanners médicaux. À partir de l'ensemble des projections obtenues, un algorithme de traitement des données combinant ces informations permet de reconstruire en 3 dimensions la carte d'atténuation de l'objet.

La théorie de la reconstruction CBCT a été largement étudiée dans divers articles. Pour les lecteurs intéressés, les détails mathématiques précis peuvent être trouvés dans les références suivantes [8][10]. Cependant des artefacts de reconstructions peuvent apparaitre. Le lecteur intéressé trouvera plus de détails dans les ouvrages suivants. Nous pouvons citer notamment :

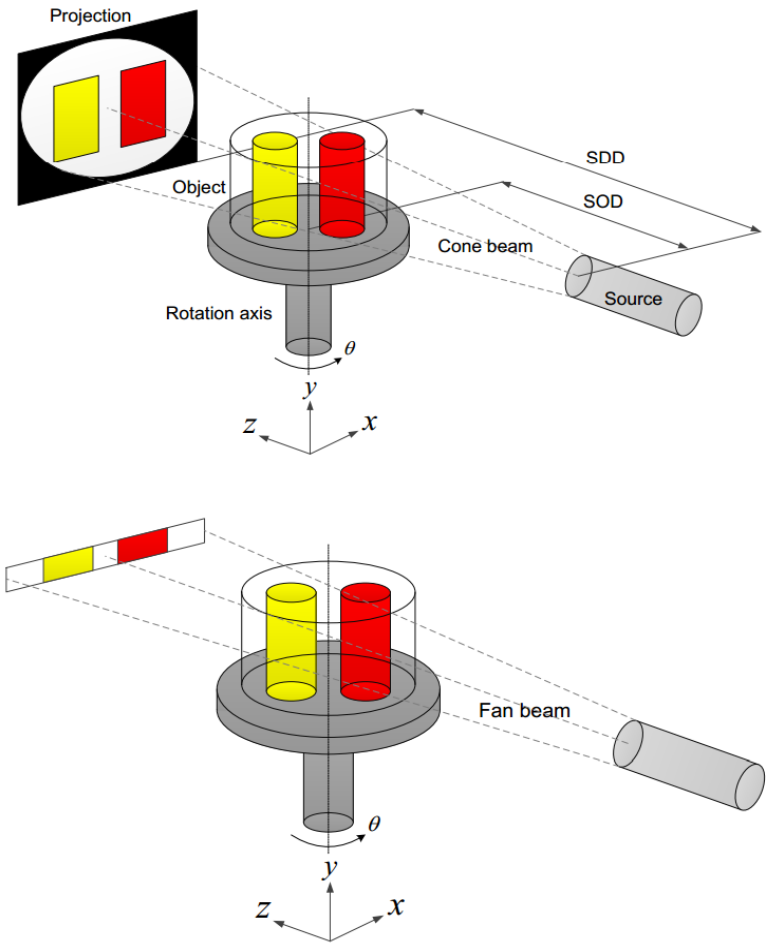

Figure A.1: Schéma d'une acquisition en faisceau conique et éventail[1]

- le durcissement de faisceau ou beam hardenning. Ce phénomène est dû au caractère polychromatique du faisceau de rayons X traversant la matière. Les photons de faible énergie sont préférentiellement absorbées ce qui induit une modification de l'énergie moyenne des rayons X dépendant de l'atténuation.
- le diffusé de l'objet
- le diffusé du détecteur

De nombreuses techniques ont été mises au point au cours du temps afin de corriger ces artefacts. Les différentes techniques peuvent être divisées en deux catégories. La première catégorie regroupe les techniques de type pré-traitement. Dans cette approche, le rayonnement diffusé est corrigée ou supprimée avant d'atteindre le détecteur et de contribuer aux niveaux de gris dans les projections. Ceci est réalisé en changeant la géométrie mise en place et nécessite souvent du matériel supplémentaire. Parmi ces méthodes, nous pouvons citer notamment :

- les grilles anti-diffusé,
- l'augmentation de la distance objet détecteur (méthode dite air gap),
- la collimation du champ de vue.

La seconde catégorie regroupe les techniques de type post-traitement. Le rayonnement diffusé est corrigé après l'acquisition des projections. Le traitement du signal peut intervenir dans les projections elles-mêmes. Nous pouvons citer les méthodes basé sur :

- des mesures directes sur la chaine d'acquisition [44, 6, 45, 47, 48, 49, 52, 50, 51],
- des simulations de type Monte Carlo [53, 54, 55, 56, 57, 27, 58, 59, 60, 61, 62, 58, 59, 60, 63, 64, 65, 64]
- des superpositions de noyau (Scatter kernel Superposition ou SKS) [65, 66, 67, 5, 68, 69, 70, 71, 73, 78, 25, 56]

Le traitement du signal peut intervenir également au niveau de l'algorithme de reconstruction ou après la reconstruction[79, 80, 81].

A.3 Objectifs

L'objectif de cette thèse est de concevoir une technique de correction du diffusé efficace dans une large gamme d'énergie (keV-MeV). Cette méthode doit permettre d'adresser des objets avec des géométries complexes multimatériau. Cette approche doit être simple à mettre en œuvre. Elle doit être adaptée à n'importe quel type de géométrie d'acquisition (circulaire, hélicoïdale ou robotisé).

Il est évident que la correction du diffusé à l'aide d'une approche de type SKS permet d'obtenir le meilleur compromis entre une correction du diffusé robuste et une rapidité dans la vitesse de calcul. Ces méthodes sont applicables sur une large gamme de conditions d'acquisition. Ces méthodes ne nécessitent pas de matériel supplémentaire (à la différence des grilles anti-diffusé par exemple) ce qui offre un avantage majeur en réduisant la complexité expérimentale. Les approches de type SKS sont informatiquement plus efficace que les méthodes Monte Carlo pure. En outre, ils ne nécessitent pas de dose ou d'acquisition supplémentaire, ce qui est important dans le domaine de l'imagerie médicale. De plus, cette approche n'est pas combinée avec une méthode de reconstruction. Le jeu de projections ainsi corrigé peut être reconstruit avec n'importe quel type d'algorithme.

Le seul inconvénient majeur de l'utilisation des méthodes de type SKS est qu'elles ne peuvent pas prendre pleinement en compte la variation de la dispersion due à la forme et les variations de l'épaisseur ainsi que la distribution spatiale de l'hétérogénéité dans l'objet. Ce qui est notamment le cas pour la tomographie industrielle un rapport diffusé sur directe assez élevé. Comme mentionné dans la section 1.5, beaucoup de modifications produites dans la méthode SKS ont été proposées, une de ces approches consiste à paramétrer les kernels en termes d'épaisseur telle que proposée par Sun et al. [5]. Dans cette approche, un ensemble discret de noyaux dépendants de l'épaisseur traversées sont utilisés pour une gamme d'épaisseur correspondantes. Cette méthode donne des résultats satisfaisants dans de nombreuses applications, y compris médicale où cette méthode originale a été testée. Cependant, pour des SPR plus élevés, les étapes différentes de l'algorithme de correction SKS doivent être reconsidérées. En particulier, un meilleur échantillonnage des noyaux par rapport à l'épaisseur de l'objet est nécessaire pour obtenir une meilleure précision. En outre, lorsque le niveau du diffusé est non négligeable en raison d'un SPR conséquent, la robustesse et la convergence de

la correction itérative du système devient critique. En effet, une légère surestimation du niveau de diffusé pourrait conduire à corrections aberrantes (comme des valeurs négatives). Le schéma d'itération adopté dans la méthode originale [5] est basée sur la soustraction du diffusé à partir des projections initiales. Ce type de schéma peut ne pas convenir à la gamme d'énergie de notre étude en raison du risque de surestimation du diffusé.

Par conséquent, le chapitre 3 de cette étude décrit une méthode adaptée à un niveau élevé de SPR. Nous vous proposons une paramétrisation analytique des noyaux de dispersion. Cette approche permet une plus grande précision dans la description des noyaux de convolution en fonction de l'épaisseur traversée. Les corrections du diffusé sont effectuées en utilisant cette approche et les résultats obtenus sont comparés à l'approche classique. L'objet et les matériaux utilisés sont typiques des applications industrielles. En outre, une approche itérative de type multiplicatif est mis en œuvre pour lutter contre le problème de surestimations du diffusé. Un autre aspect important de ce chapitre est l'étude de la méthode proposée sur des objets multimatériaux. Un autre aspect très important de ce travail est d'examiner la contribution du diffusé du détecteur. Tel que mentionné dans la section 1.5, des études récentes ont montré de la diffusion du détecteur est un point très important, spécialement dans le cas d'une source de rayons X de forte énergie [25][65][66]. Sun et al [5] a proposé, pour tenir compte du diffusé du détecteur, d'utiliser deux termes gaussiens. Mais cette étape de prétraitement avant la déconvolution SKS d'être modéliser avec précision et tenir compte de la variabilité du noyau en fonction de l'épaisseur de l'objet, notamment pour prendre en compte le durcissement du spectre du faisceau. Dans le chapitre 4, nous proposons d'évaluer la contribution du diffusé du détecteur dans la gamme classique des contrôles industrielles en proposant une évolution de la méthode présentée au chapitre 3. Ce modèle permet de séparer les contributions du diffusé dues au détecteur et à l'objet. Dans ce chapitre, nous avons testé notre approche sur une large gamme d'énergie depuis une centaine de keV jusqu'à 6 MeV.

Le chapitre 5 de ce travail présente la validation de notre approche par noyaux continus en utilisant des mesures expérimentales. En effet, la simulation de la contribution du diffusé détecteur est fortement dépendant de la description physique au plus près de la réalité du détecteur plan. Malheureusement, les constructeurs de détecteur ne donnent pas d'information très précises à ce sujet. Pour remédier à cela, nous proposons une adaptation de notre approche par noyaux continus basée sur la combinaison entre des simulations de type Monte Carlo pour le diffusé de l'objet et des mesures expérimentales pour le diffusé détecteur.

A.4 Correction du diffusé par une méthode de description continue des noyaux de convolution

Cette section se concentre sur des modifications de l'approche discrète classique proposée par la méthode SKS de Sun et al [5]. Le lecteur intéressé trouvera des précisions dans le chapitre 3. La méthode repose sur l'hypothèse que la contribution du diffusé résulte de la convolution entre le rayonnement direct et un noyau de convolution. Dans cette approche, chaque noyau est modélisé comme la somme des contributions des diffusés objet et détecteur sur une gamme d'épaisseur donnée. Cette méthode n'est

pas adapté au cas de figure ou le SPR est élevée typiquement (typiquement [300,500] keV).

Dans ce chapitre, nous proposons une description analytique du noyau de diffusé en fonction de l'épaisseur de matériau traversé afin de réaliser un meilleur échantillonnage des noyaux sur toute la plage d'épaisseur de l'objet. Nous proposons également une modification du schéma itératif afin de rendre la méthode robuste au cas de figure présentant un SPR élevé. Nous appelons cette correction du diffusé par une description continue des noyaux de convolution (en anglais scatter correction using continuously thickness-adapted kernels) ou plus simplement approche continue pour référence future. L'approche a été testé sur des vrais acquisitions avec un objet mono matériau et également par simulation sur des objets multimatériaux.Ce travail a fait l'objet d'un article de la revue NDT& E [75].

Le signal mesuré au niveau du détecteur $I(m,n)$ a deux composantes: $P(m,n)$ est le signal primaire constitué par les photons qui passent directement, sans aucune atténuation ou diffusion et $S(m,n)$ est la contribution du signal des photons diffusés par l'objet et par le détecteur. Par conséquent, le signal mesuré est donné par :

$$I(m,n) = P(m,n) + S(m,n) \tag{A.1}$$

où m et n correspondent à la position du pixel sur le détecteur. Le signal du diffusé peut être modélisé comme la somme des contributions d'un groupe de fins faisceaux passant par l'objet et le détecteur. Pour chaque faisceau, on détermine un noyau de convolution qui représente le rapport diffusé sur primaire. Le quantité totale de diffusé $S(m,n)$ peut alors être modélisée comme:

$$S(m,n) = \sum_k \sum_l P(k,l) h_{T(k,l)}(m-k, n-l) \tag{A.2}$$

où, h_T étant l'épaisseur (T) dépendant du noyau, avec une amplitude égale au rapport de la diffusé sur primaire au pixel courant, le faisceau est centré sur le pixel. La somme dans le processus de convolution est effectué sur tous les pixels (k,l) du détecteur L'épaisseur est calculée avec la loi de Beer Lambert

$$T(k,l) \approx \frac{1}{\mu} \ln \frac{O(k,l)}{P(k,l)} \tag{A.3}$$

avec μ étant la constante d'atténuation de l'objet à l'étude à l'énergie moyenne du spectre utilisé. h_T peut être approximé par l'équation formé par un facteur d'amplitude $C(k,l)$ (qui est une fonction du signal primaire $P(m,n)$ et $O(m,n)$ non atténué l'intensité de l'air) et un facteur de forme $G(m-k, n-l)$ constitué de deux gaussiennes de symétrie circulaire décrivant la forme du noyau. L'équation A.2 devient :

$$S(m,n) = \sum_k \sum_l P(k,l) C(k,l) G(m-k, n-l) \tag{A.4}$$

avec

$$\begin{aligned} G(m-k, n-l) = A \exp\left(-\frac{(m-k)^2 + (n-l)^2}{2\sigma_1^2} \right) \\ + B \exp\left(-\frac{(m-k)^2 + (n-l)^2}{2\sigma_2^2} \right) \end{aligned} \tag{A.5}$$

Dans l'approche discrète, on utilise un nombre fini de noyaux de convolution chaque noyau correspond une certaine gamme d'épaisseur. L'équation de superposition des noyaux de convolution est donc :

$$S(m,n) = \sum_i \sum_k \sum_l P(k,l) R_i(k,l) C_i(k,l) G_i(m-k)(n-l) \tag{A.6}$$

$$R_i(k,l) = \begin{cases} 1, & \text{si } T_i(k,l) \leq T(k,l) < T_{i+1}(k,l) \\ 0, & \text{sinon} \end{cases} \tag{A.7}$$

Où i donnes le numéro du groupe correspondant à l'épaisseur et T_i et T_{i+1} sont les bornes inférieure et supérieur correspondant au groupe i.

Dans l'approche continue, les paramètres des noyaux de convolution sont interpolés par des équations mathématique en fonction de l'épaisseur de matière traversée. Donc l'équation A.6 est modifiée pour obtenir l'équation suivante :

$$S(m,n) = \sum_k \sum_l P(k,l) C(k,l,T(k,l)) G(m-k, n-l, T(k,l)) \tag{A.8}$$

Les simulations des noyaux de convolution ont été réalisé à l'aide de simulation de type Monte-Carlo (MC), avec le logiciel CIVA [3]. Pour la simulation des noyaux de convolution, nous avons simulé la géométrie réelle de l'acquisition. Un nombre fini de cas a été simulé pour différentes épaisseur de plaque parallélépipédique , constitué du même matériau que l'objet, de manière à obtenir un ensemble discret de noyaux. On ajuste ensuite pour chaque noyau une courbe en utilisant l'équation 2.6. Pour chaque noyau on obtient donc un jeu de paramètres $\alpha, \beta, A, B, \sigma_1, \sigma_2$. Ensuite chacun de ces paramètres sont représentés en fonction de l'épaisseur de matière traversée. A l'aide d'une méthode de régression par moindre carré, on ajuste une courbe analytique pour chacun de ces paramètres (voir figure). Les deux fonctions dans l'équation A.5 sont de définies par les écarts-types σ_1, σ_2. Ces deux écarts types sont représentatifs de diffusé de l'objet et du détecteur :

- 1 est relié au diffusé objet, il doit augmenter en fonction de l'épaisseur traversé
- 2 est relié au diffusé détecteur et il doit être constant en fonction de l'épaisseur traversé

Le schéma itératif de correction du diffusé est donné par la figure A.2, il suit les étapes suivantes :

1. La projection brute (c'est-à-dire non corrigée) permet d'obtenir une estimation du rayonnement primaire
2. L'épaisseur traverse est calculé à partir de l'équation ref.
3. Pour chaque pixel de l'image on calcule le noyau de convolution à partir du modèle analytique
4. Le diffusé est estimé en utilisant l'équation (ref2.10)
5. Le rayonnement primaire estimé est mise à jour en utilisant les équations suivantes

$$P^{n+1}(m,n) = P^0(m,n) \times \frac{P^n(m,n)}{P^n(m,n) + S^n(m,n)} \tag{A.9}$$

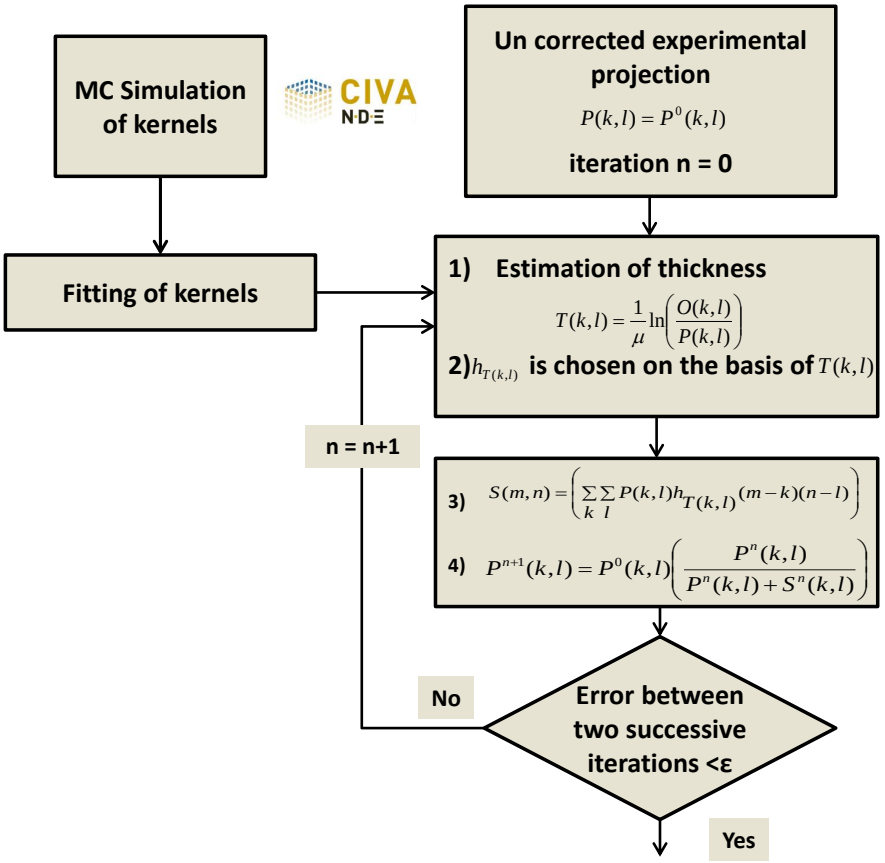

Figure A.2: Schéma de l'algorithme de correction du diffusé

Figure A.3: Image de l'engrenage en fer[6]

Les étapes 1 à 5 sont répété jusqu'à la convergence.

La méthode a été testé avec succès sur un objet type bague d'engrenage mono matériaux. La tomographie a été réalisé à une tension de 400 kV et un courant de 15 mA avec une filtration supplémentaire de 4 mm de plomb et 1 mm de cadmium. Le détecteur est de marque Thales référence Flashscan 33 consiste en une dalle de 2240 × 3200 pixels, chaque pixel de forme carré présente une taille de 127 µm. La figure A.3 présente une photo de l'engrenage, et la figure A.5 une projection expérimentale de l'engrenage.

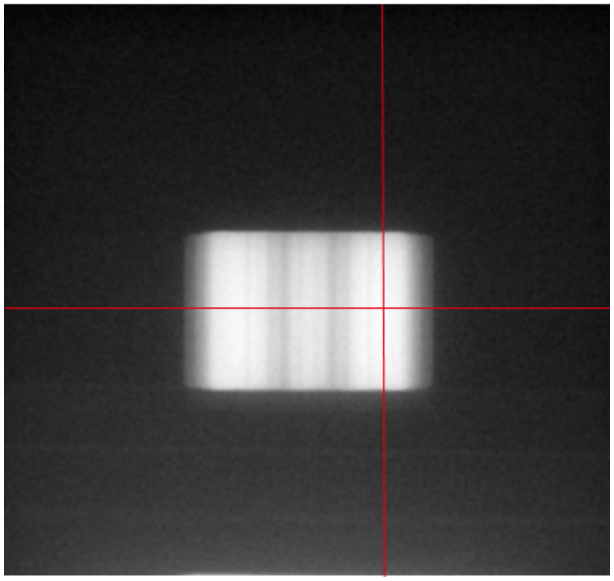

Figure A.4: Exemple d'une projection de l'engrenage

La figure A.5 présente les profiles horizontaux et verticaux extraits de la projection de la figure A.4 non et corrigé du rayonnement diffuse.

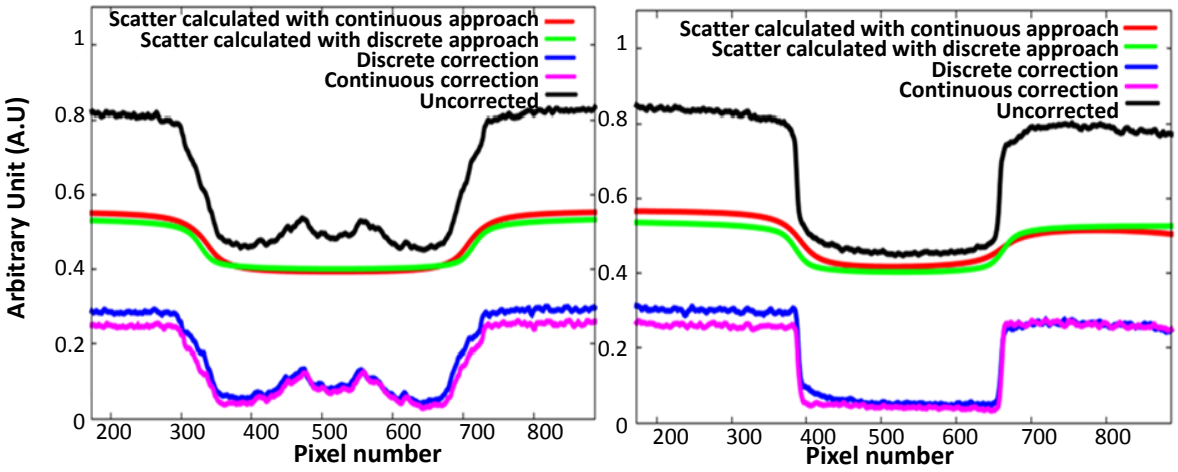

Figure A.5: a) Profil Horizontal le b) Profil vertical non corrigé et corrigé avec la méthode discrète et continue

Nous pouvons voir que la méthode avec les noyaux continus de meilleurs résultats notamment au niveau des contours de l'objet par rapport à la méthode discrète. Ceci est dû au meilleur échantillonnage des noyaux.

La figure A.6 montre les coupes reconstruites obtenu pour des projections non corrigées et corrigées utilisant les méthodes continue et discrète. Le tableau A.1 présente l'écart-type et la moyenne des valeurs reconstruites pour les données corrigées et non corrigées dans la région inter dent et dans une dent de l'engrenage en utilisant des masques binaires.

On obtient une valeur de l'atténuation linéaire non corrigée de 0.196 cm^{-1} pour le fer, de 0.634 cm^{-1} avec l'approche discrète et de 0.80 cm^{-1} avec l'approche continue. La valeur de la constante d'atténuation linéaire pour l'énergie moyenne du spectre

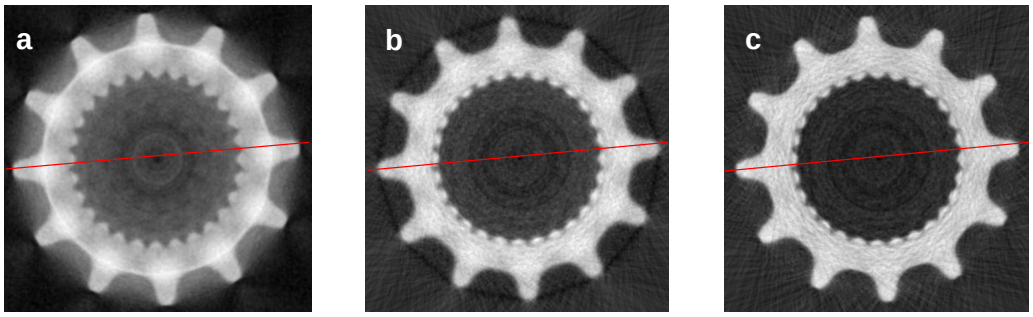

Figure A.6: Coupes reconstruites) sans correction b) corrigée avec la méthode discrète c) corrigée avec la méthode continue

		moyenne (cm^{-1})	éc. typ.
Non corrigé	air	0.024	± 0.002
	iron	0.196	± 0.007
Méthode discrète	air	0.003	± 0.006
	iron	0.634	± 0.005
Méthode continue	air	0.001	± 0.006
	iron	0.800	± 0.009
Valeur moyenne	air	0.0001	
	iron	0.836	

Table A.1: Moyenne et écart type pour l'air et le fer obtenues dans les coupes reconstruites sans et avec correction

(319 keV) est 0.836 cm^{-1}, ce qui démontre le bon accord entre la valeur obtenue par l'approche continue et la valeur théorique. Le méthode continue présente des profils de reconstruction améliorés par rapport à l'approche discrète comme on peut le voir sur la figure A.7. La méthode continue présente une meilleure amélioration de la netteté des contours de l'objet par rapport à la méthode discrète.

Les résultats obtenus avec la méthode continue sont en accord avec ceux obtenue par A. Peterzol et al [6] à l'aide d'une méthode utilisant un dispositif anti diffusé. Cette dernière nécessite de nombreuses acquisitions conduisant à une dose utile et des temps d'acquisition plus important.

Le chapitre 3 section 2.8.4 montre que les noyaux de diffusé, dans la gamme d'énergie considérée, de deux matériaux peuvent être considéré comme comparable pour une atténuation équivalente. La méthode fonctionne également pour un objet polymatériaux.

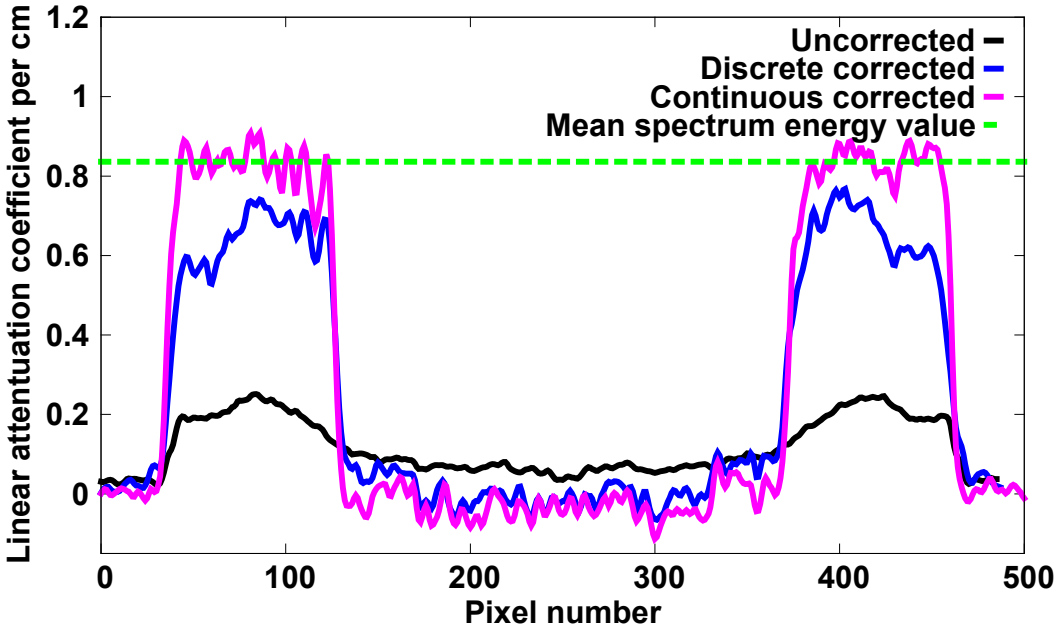

Figure A.7: Profiles extraites de la coupe reconstruite a) sans corrections b) correction avec la méthode discrète c) correction avec la méthode continue

A.5 Développement d'un modèle de sépération de la contribution du diffusé objet et détecteur

Beaucoup de recherche et développement a été consacrée pour corriger le diffusé de l'objet. Mais certaines récentes études ont prouvé l'importance de prendre en considération le diffusé du détecteur [23][24][25] particulièrement pour la gamme d'énergie utilisée pour des contrôles industriels. La contribution de diffusé à l'intérieur du détecteur peut venir de la diffusion Compton interagissant avec les parties diverses du détecteur comme le support, la contre-plaque etc. Le rétrodiffusé de la contre-plaque du détecteur augmente rapidement avec la source d'énergie plus haute comme l'a montré Heisel et al [26]. De plus, la contribution de la fluorescence des photons X et le flou dû aux photons visibles générés dans le scintillateur aboutit également à la réduction de la résolution spatiale.

Nous proposons d'évaluer la contribution du diffusé du détecteur dans la gamme classique du contrôle non destructif industriel (100 keV-6 MeV) en utilisant la méthode des noyaux continue présenté en détails dans le chapitre 3. La méthode continue et l'autre méthode SKS classique [5] utilisent un modèle à deux Gaussienne pour la description des noyaux de convolution. Cette paramétrisation avec deux Gaussienne comporte plusieurs lacunes. Tout d'abord, les contributions du diffusé du détecteur et de l'objet sont entremêlées, ce qui peut rendre l'ajustement du modèle continue délicat. En outre, la contribution à haute fréquence du diffusé du détecteur génère une forte contribution dans le pixel central du noyau. Cette forme particulière incite à explorer une augmentation du nombre de Gaussienne utilisée. Par conséquent, nous proposons d'utiliser un modèle de noyau de convolution à quatre Gaussienne afin de pouvoir identifier les contributions respectives du diffusé de l'objet et du détecteur mais aussi pour avoir une modélisation plus stable. Le lecteur intéressé par de plus ample détails pourra se rapporter au chapitre 3. Nous avons testé notre modèle, avec succès, dans le cas d'une

pièce de fonderie en aluminium. Ce travail a été publié dans la revue Journal of X-Ray Science and Technology 2016.

L'effet du diffusé devient plus important lorsque l'énergie de rayons X augmente, en particuliers dans le cas des hautes énergies de l'ordre du MeV. Tout d'abord, il y a une augmentation sensible de la probabilité du diffusé Compton vers l'avant et donc ces photons sont plus susceptibles d'atteindre le détecteur. En outre, ces photons diffusés sont plus énergiques et donc plus susceptibles de s'échapper de l'objet. En augmentant l'énergie incidente, l'énergie des particules chargées (électrons libérés de recul et de positrons) dans l'objet augmente également, ce qui entraîne une augmentation marquée du nombre de photons générés par le rayonnement de freinage. A des énergies de photons supérieures à 1.022 MeV, la production de paires produit des photons qui peuvent contribuer à l'augmentation de la contribution du diffusé. Afin de tester notre approche sur une large gamme d'énergie, nous avons testé notre méthode dans le cas d'acquisition avec un accélérateur linéaire de 6 MeV.

A.5.1 Modèle à quatre Gaussienne

Dans l'approche de correction du diffusé avec la méthode SKS avec des noyaux continus [75], le signal du diffusé peut être modélisée comme la somme des contributions du diffusé d'un groupe de faisceaux fin en passant par l'objet et le détecteur. Pour chaque faisceau, un noyau on peut déterminer le poids du diffusé de rapport au primaire. Le signal du diffusé totale $S(m,n)$ avec m and n la position du pixel sur le détecteur, peut alors être modélisé comme:

$$S(m,n) = \sum_k \sum_l P(k,l) h_{T(k,l)}(m-k, n-l) \tag{A.10}$$

où, h_T est l'amplitude égale au rapport du signal diffusé au niveau du pixel courant du signal primaire pour une épaisseur (T). P est le signal du rayonnement primaire constitué par les photons qui traversent directement l'objet sans aucune atténuation. Au lieu d'utiliser la loi de Beer-Lambert sur la base d'un coefficient d'atténuation linéaire comme [5], l'épaisseur $T(k,l)$ dans l'équation A.10 est directement calculé à partir d'une table look up f_{BH}, calculé pendant la phase de simulation des noyaux.

$$T(k,l) = f_{BH}\left(\frac{P(k,l)}{O(k,l)}\right) \tag{A.11}$$

où O est l'image non atténuée. Il est intéressant de noter que le durcissement de faisceau est pris en compte avec cette procédure. Les paramètres d'acquisition et le matériau des plaques de calibration doivent être le même que l'objet de l'étude. Les valeurs du rayonnement primaire directement transmis P ont été calculés pour chaque épaisseur simulée.

Le noyau de convolution h_T peut être estimé par une équation constituée de quatre fonctions Gaussiennes symétriques circulairement :

$$h_T(m-k,n-l) = A\exp\left(-\frac{(m-k)^2+(n-l)^2}{2\sigma_1^2}\right) + B\exp\left(-\frac{(m-k)^2+(n-l)^2}{2\sigma_2^2}\right) + C\exp\left(-\frac{(m-k)^2+(n-l)^2}{2\sigma_3^2}\right) + D\exp\left(-\frac{(m-k)^2+(n-l)^2}{2\sigma_4^2}\right) \tag{A.12}$$

Le modèle à quatre Gaussienne est nécessaire afin de séparer clairement les contributions du diffusé de l'objet et du détecteur.

Les simulations Monte Carlo (MC) ont été réalisées avec CIVA software [3] pour la génération de noyaux. Les simulations ont été réalisées avec des cales de de même matériau que l'objet de l'étude. Le détecteur de type écran plat a été simulé comme un empilement de plusieurs couches successives constitué de 0.1 mm couche avant en aluminium suivie d'un espacement de 0.8 mm, d'une couche de Csl d'épaisseur 0.06 mm, d'un substrat de silicium de 1 mm et enfin une plaque de plomb de 1 mm.

Les huit paramètres de l'équation A.12, $A, B, C, D, \sigma_1, \sigma_2, \sigma_3, \sigma_4$ sont également interpolées en fonction de l'épaisseur pour obtenir une description continue du noyau de convolution par rapport à l'épaisseur [75]. Nous avons utilisé un modèle à quatre Gaussienne afin de séparer la contribution du diffusé de l'objet et du détecteur.

A.5.2 Les acquisitions

Pour l'acquisition, la distance source-détecteur était de 845 mm et la distance entre la source et l'axe de rotation était de 424 mm. Le setup est principalement consisté d'une source de rayons X (tension maximal 230 kV filtré par 0.35 mm de cuivre), d'un objet posé sur une table de rotation et d'un détecteur type écran plat d'une taille de 1840 × 1456 avec un binnind 2×2 et d'une taille de pixel de 0.254 mm.

Les acquisitions ont été réalisées sur un turbo en aluminium comme indiqué dans la figure ref échantillon qui avait une dimension maximale d'environ 300 mm.

Figure A.8: Image du turbo en aluminium

Afin de valider d'établir ma contribution du diffusé objet par rapport au diffusé détecteur, nous avons réalisé une acquisition avec un collimateur de type fente insérée

juste devant le détecteur. Le setup est décrit à la figure A.9. Le collimateur est en acier avec une épaisseur de 30 mm et une largeur de 15 mm. Le collimateur élimine environ toute la contribution de la dispersion de l'objet.

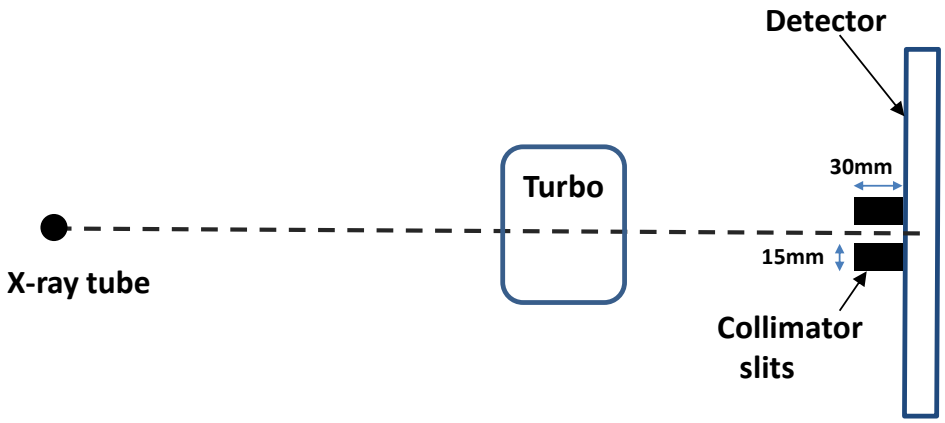

Figure A.9: Schéma de l'acquisition mis en place avec le collimateur

Concernant les acquisitions effectuées sur un accélérateur linéaire de 6.0 MV. La distance entre la source et le détecteur était de 3.18 m et la distance entre la source et l'axe de rotation était de 2.45 m. Les acquisitions ont été réalisées sur un engrenage en fer, avec un diamètre maximum de 7.5 cm, comme l'illustre la figure A.10. Le détecteur utilisé est un détecteur de type écran plat avec une taille de pixel de 200 µm, préfiltré par une plaque de cuivre d'épaisseur 10 mm.

Figure A.10: Image de l'engrenage utilisé pour les acquisitions avec l'accélérateur linéaire

A.5.3 Résultats et discussions

Comme indiqué précédemment, afin d'estimer dans les projections l'épaisseur traversé à chaque pixel, des simulations ont été réalisées avec des cales de différentes épaisseurs.

Les paramètres d'acquisition et la matière des plaques a été maintenue identique à l'acquisition réelle. La contribution du rayonnement primaire P a été calculé à l'aide de la simulation pour chaque épaisseur de plaque.

L'épaisseur en fonction de la transmittance LUT f_{BH} donnée dans l'équation A.12 a été analytiquement calculé à l'aide d'une régression aux moindres carrés pour déterminer les coefficients a_1, b_1, a_2, B_2 dans l'équation A.13 comme le montre la figure A.11. La détermination classique de l'épaisseur basée sur le coefficient d'atténuation linéaire moyen est également représentée par la courbe rouge de la figure A.11. Le durcissement de faisceau, pas très important, est cependant clairement visible. L'équation A.13 donne la relation de la valeur de l'épaisseur T en fonction de la transmittance $P(k,l)/O(k,l)$.

$$\begin{aligned} T(k,l) &= f_{BH}\left(\frac{P(k,l)}{O(k,l)}\right) \\ &= -a_1 ln\left(\frac{P(k,l)}{O(k,l)}\right)^{b_1} - a_2\left(ln\frac{P(k,l)}{O(k,l)}\right)^{b_2} \end{aligned} \tag{A.13}$$

avec $a_1 = 20.8$, $b_1 = 0.83$, $a_2 = 0.000572$, $b_2 = 1$

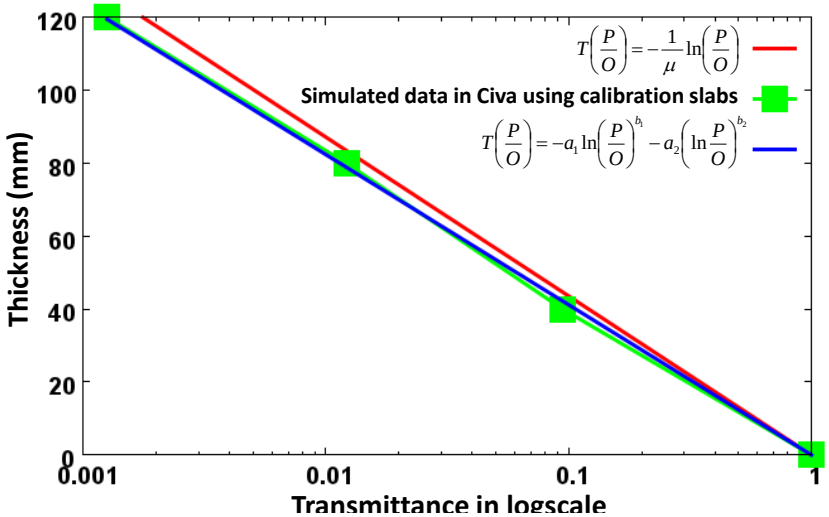

Figure A.11: Épaisseur en fonction de la transmittance

L'estimation des paramètres $A, B, C, D, \sigma_1, \sigma_2, \sigma_3, \sigma_4$ du modèle à quatre Gaussienne en fonction de l'épaisseur a été réalisé avec une régression aux moindres carrés comme illustré à la figure A.12. On peut constater que l'écart type σ_1 et σ_2 varient en fonction de l'épaisseur de l'objet alors que σ_3 et σ_4 restent constants. Nous pouvons en conclure que σ_1 et σ_2 correspondent à la contribution du diffusé de l'objet qui augmente sur l'épaisseur de l'objet. De plus, nous remarquons que σ_1 est très grand devant σ_2. Nous pouvons en déduire que σ_1 est relié à la contribution basse fréquence due à la diffusion multiple dans l'objet. Alors que la contribution de σ_2 est relativement faible. Nous remarquons également peu de différence entre les paramètres A et B qui correspondent au poids de l'amplitude des Gaussiennes. Cette variation des paramètres

A, B, σ_1, σ_2 démontre qu'un modèle à deux gaussien pour représenter le diffusé de l'objet est nécessaire.

De même, on observe que σ_3 et σ_4 restent constants en fonction de l'épaisseur de l'objet, nous en déduisons que σ_3 et σ_4 sont reliés à la contribution haute fréquence du détecteur. En suivant le même raisonnement, σ_3 et σ_4 sont différents les uns des autres alors et les paramètres C et D sont assez proche. Par conséquent, un modèle à deux Gaussienne pour le détecteur est également crucial.

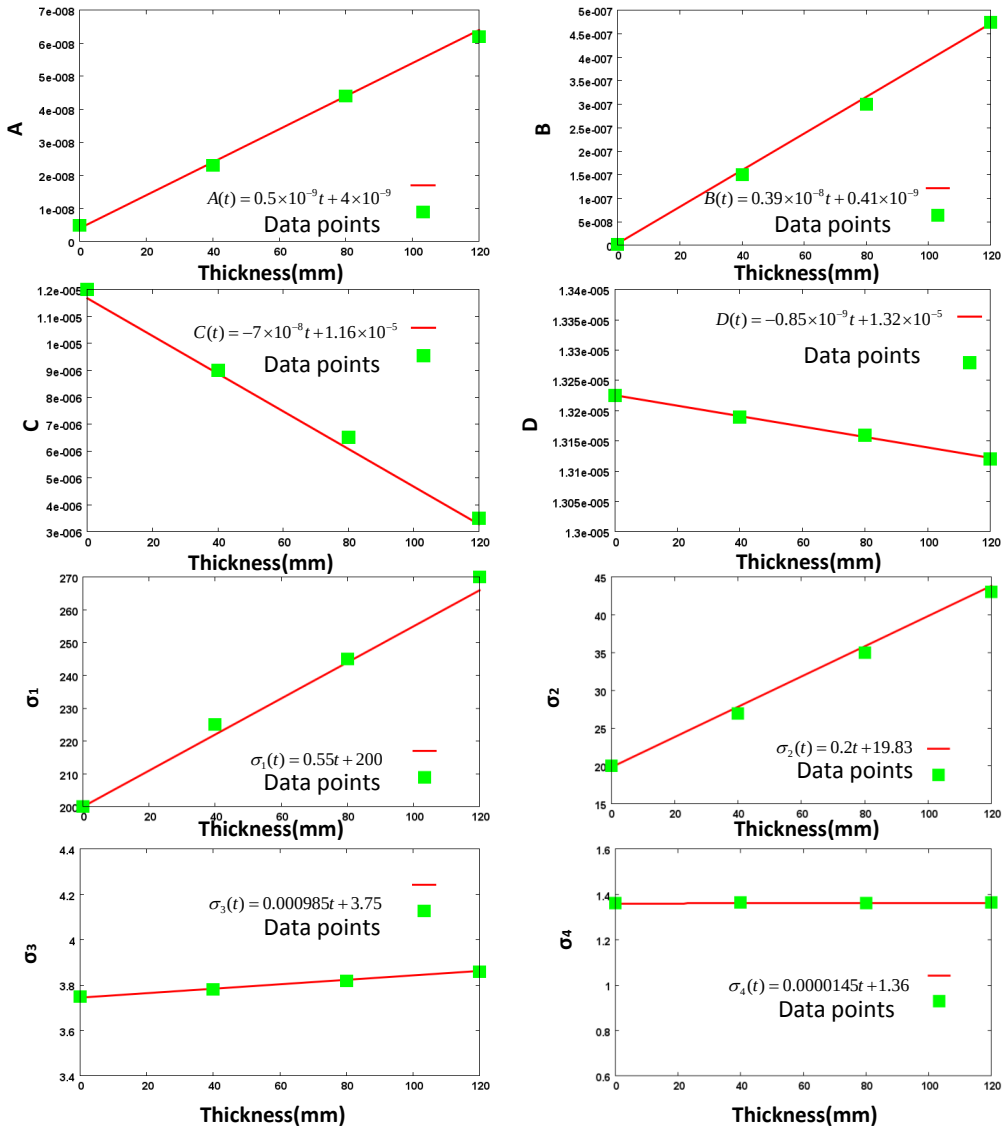

Figure A.12: Estimations des paramètres $A, B, C, D, \sigma_1, \sigma_2, \sigma_3, \sigma_4$ en fonction de l'épaisseur traversée

La figure A.13a) montre la coupe reconstruite obtenue avec des projections non corrigées en utilisant l'algorithme FDK [addref]. Nous avons d'abord évalué la contribution du diffusé de l'objet seul et nous avons corrigé les projections avec seulement les noyaux du diffusé de l'objet. Le résultat obtenu est présenté à la figureA.13b). Elle montre clairement que la correction du diffusé de l'objet seul ne suffit pas à corriger tous les artefacts dus au diffusé. Ceci est également démontré à la figureA.14 qui montre un profil extrait des coupes reconstruites corrigées et non corrigées. Les noyaux du diffusé du détecteur et de l'objet ont ensuite été utilisés pour effectuer les corrections des projections. La reconstruction obtenue avec cette correction est présenté sur la figure A.13 c). Le résultat obtenu avec la correction du diffusé de l'objet et du détecteur est en accord avec la valeur attendue du coefficient d'atténuation linéaire à une énergie moyenne de 98 keV (0.483 cm^{-1}).

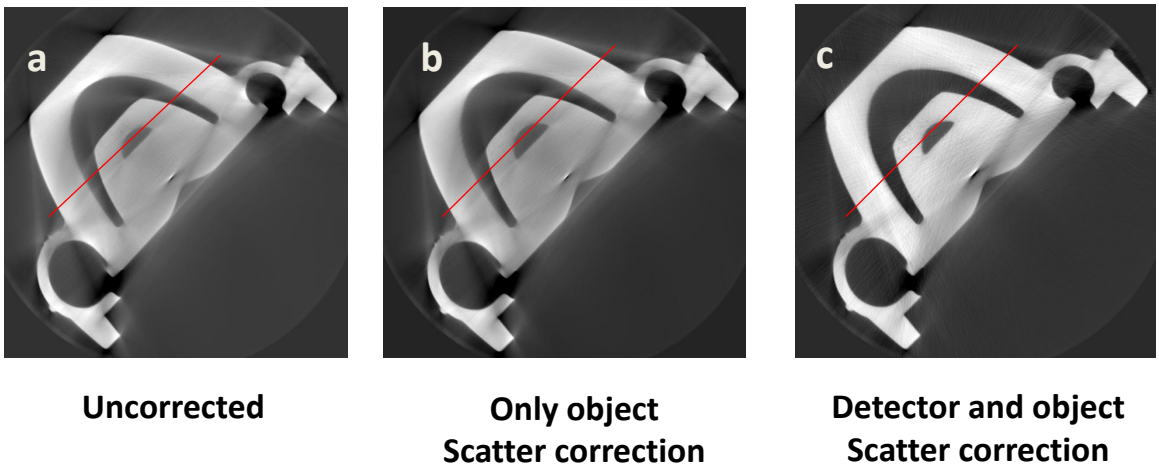

Figure A.13: Coupe reconstruite avec a) les projections non corrigées b) les projections corrigées avec les noyaux de convolution du diffusé objet c) les projections corrigées avec les noyaux de convolution du diffusé objet et détecteur

Le tableau A.2 montre la moyenne et l'écart type des valeurs reconstruites pour les données corrigées et non corrigées dans l'air et l'aluminium calculée en utilisant des masques binaires. Sans correction, le valeur du coefficient d'atténuation linéaire de l'aluminium est estimée à 0.258 cm^{-1} . En utilisant uniquement les noyaux du diffusé de l'objet, on obtient une valeur de 0.324 cm^{-1}. Pour l'énergie moyenne du spectre utilisée, la valeur du coefficient d'atténuation linéaire est 0.483 cm^{-1}. L'erreur absolue relative en pourcentage est de 32.5 % pour la correction du diffusé avec les noyaux d'objets. Considérant que, pour détecteur et objet noyaux à la fois, on obtient une valeur de 0.510 cm^{-1} pour l'aluminium. L'erreur absolue est de 6.25 %. L'artefact résiduel que nous voyons dans la reconstruction corrigée du diffusé objet et détecteur provient de l'atténuation très élevée le long de la plus grande dimension de l'objet. La dynamique du détecteur n'est pas suffisamment élevé pour prendre en compte l'atténuation le long de la plus haute dimension.

Figure A.14: Profils extraits des coupes reconstruites non corrigées, corrigées du diffusé objet et corrigées du diffusé objet et détecteur

		moy. (cm^{-1})	ec. ty.
Non corrigée	aluminium	0.258	± 0.008
	air	0.098	± 0.005
Correction du diffusé objet	aluminium	0.324	± 0.006
	air	0.106	± 0.006
Correction du diffusé objet et détecteur	aluminium	0.510	± 0.008
	air	0.001	± 0.004
Valeur théorique à l'énergie moyenne	aluminium	0.483	
	air	0.001	

Table A.2: Moyenne et écart type pour l'aluminium et l'air

Afin de valider les résultats obtenus avec l'algorithme de correction avec des noyaux continus sur une modèle de quatre Gaussienne, nous avons réalisé des acquisitions en utilisant un collimateur en acier d'une épaisseur de 30 mm (voir figure A.9). Un faisceau éventail a été produit et la contribution du diffusé de l'objet a été presque totalement éliminé par l'introduction du collimateur juste devant le détecteur. Tous les autres paramètres d'acquisition sont les mêmes que pour l'acquisition sans collimateur. La reconstruction a été réalisée sur les projections obtenues avec ce setup et le résultat est représenté sur la figure A.15 a). Elle montre clairement la présence d'artefacts due au diffusé du détecteur. On compare ensuite ce résultat expérimental avec le résultat obtenu par correction du diffusée de l'objet uniquement (voir figure A.15b). La figure A.16 compare le profil extrait de la coupe reconstruite dans le cas de l'acquisition avec le collimateur et le profil obtenu avec la correction du diffusé par laméthode des noyaux continues. Les profils montrent des résultats identiques validant les résultats obtenus par l'algorithme et prouvant la contribution majeur du diffusé du détecteur.

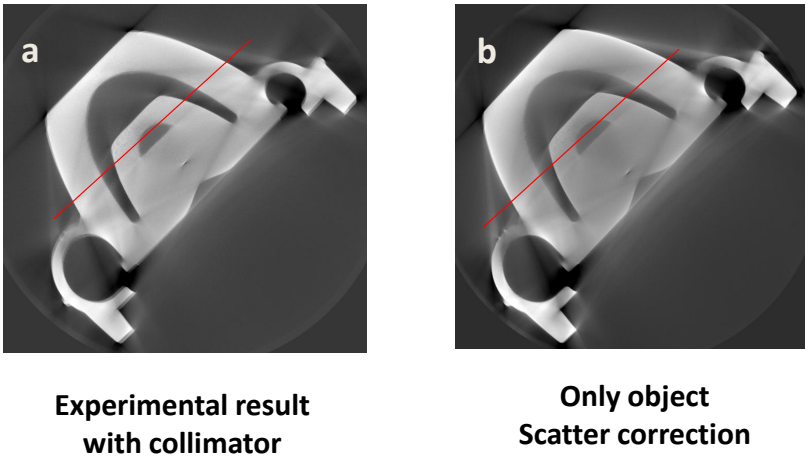

Figure A.15: Coupe reconstruite avec a) le collimateur b) la méthode de correction du diffusé objet seulement

Figure A.16: Profils extraits de la coupe reconstruite avec le collimateur devant le détecteur et la correction du diffusé objet par la méthode des noyaux continus

Le tableau A.3 présente la moyenne et l'écart type des valeurs des coefficient d'atténuation linéaire reconstruites pour l'air et l'aluminium obtenus avec le collimateur et la correction du diffusé objet par la méthode des noyaux continus. Le coefficient d'atténuation linéaire obtenu pour l'aluminium et de l'air est de 0.312 cm^{-1} and 0.096 cm^{-1}, respectivement, pour la reconstruction avec le collimateur. Ceci est en accord avec les résultats obtenus avec la correction du diffusé objet (0.324 cm^{-1} pour l'aluminium et 0.106 cm^{-1} pour l'air). Dans le domaine de l'énergie considérée, la valeur du coefficient d'atténuation linéaire moyen est de 0.483 cm^{-1} et 0.0001 cm^{-1} pour l'aluminium et de l'air respectivement. Ce résultat démontre que, dans la gamme d'énergie considérée, la correction du diffusé objet ne suffit pas et la contribution du diffusé détecteur doit également être pris en compte pour obtenir des valeurs de reconstruction correctes.

		moyenne(cm^{-1})	éc. typ.
Résultat expérimentale avec le collimateur	aluminium	0.312	± 0.006
	air	0.096	± 0.002
Correction avec les noyax du diffusé objet	aluminium	0.324	± 0.009
	air	0.106	± 0.007
Valeurs théoriques	aluminium	0.483	
	air	0.001	

Table A.3: Moyenne et écart type des coefficients d'atténuation linéaire obtenues pour l'aluminiulm et l'air pour l'acquisition avec le collimateur devant le détecteur et la correction du diffusé objet par la méthode des noyaux continus

La figure A.17 a) montre la coupe reconstruite obtenue avec des projections non corrigées pour l'engrenage de fer. La correction du diffusé sur les projections a été appliquée avec la méthode des noyaux continues. Le résultat obtenu est présenté sur la figure A.17 b). La figure A.18 montre un zoom de la coupe reconstruite. Nous pouvons remarquer des artefacts horizontaux sur les images reconstruites (voir Figure A.18a), ceci est dû à une torsion de l'axe de rotation du plateau tournant. Cette torsion résulte d'une charge mécanique trop importante d'une acquisition précédente.

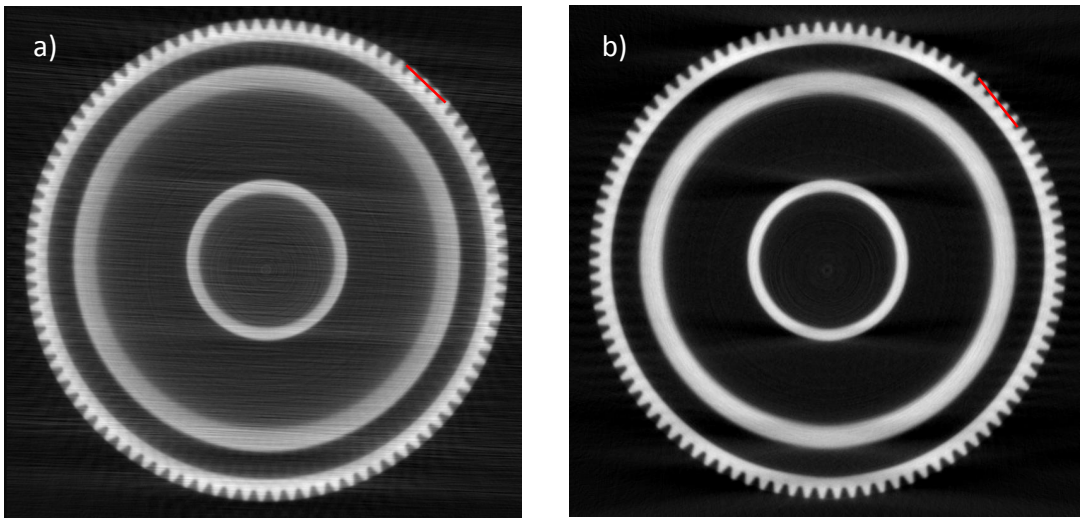

Figure A.17: Coupe reconstruite a) sans correction des projections b) avec corrections des projections

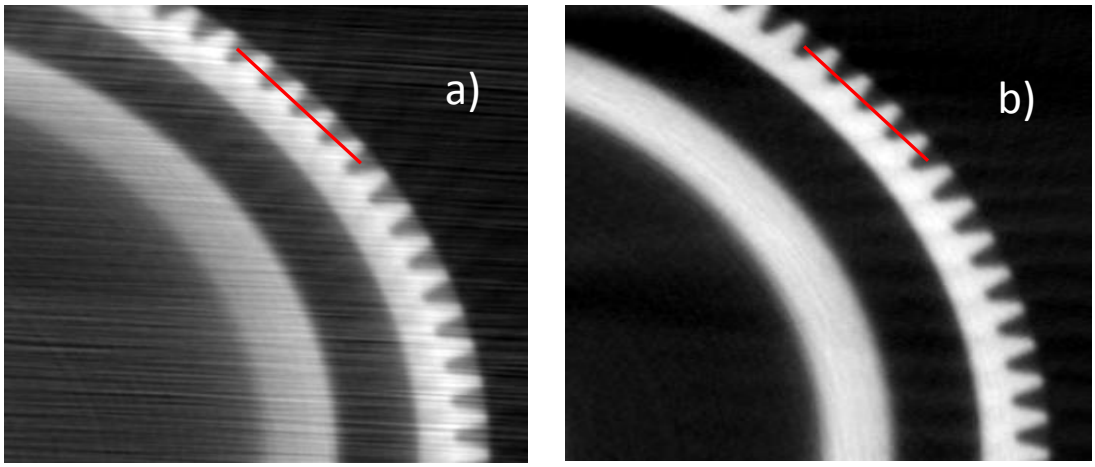

Figure A.18: Zoom sur une partie de la reconstruction a) sans correction des projections b) avec corrections des projections

La figure A.19 montre le profil extrait des images de reconstruites non corrigées et corrigées.

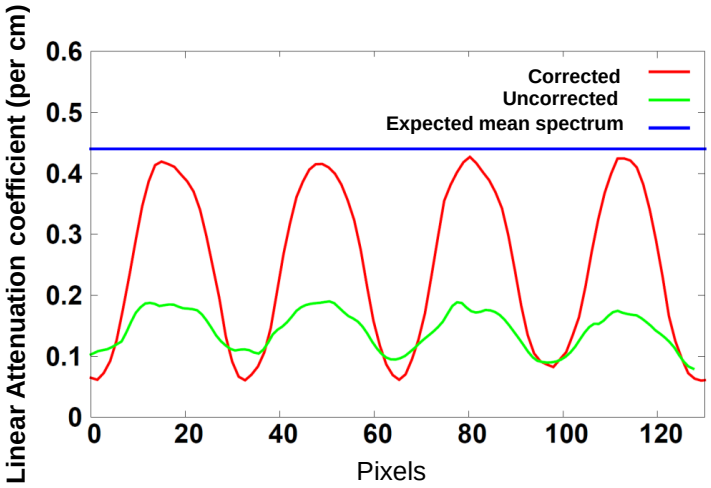

Figure A.19: Profils extraits de la coupe reconstruites à partir des projections non corrigées et corrigées

Le tableau A.4 résume les valeurs de la moyenne et l'écart type dans la coupe reconstruite pour les données corrigées et non corrigées dans l'air et de la région de fer (calculée en utilisant des masques binaires). On peut clairement voir que la correction du diffusé permet d'améliorer le contraste dans l'image reconstruite. La valeur du coefficient d'atténuation linéaire du fer est estimé à 0.172 cm^{-1} pour les données non corrigées. Après la correction du diffusé, on obtient une valeur du coefficient d'atténuation linéaire du fer de 0.41 cm^{-1}. En tenant compte de la valeur moyenne en énergie du faisceau incident (1100 keV), le coefficient d'atténuation linéaire théorique est de 0.445 cm^{-1}. L'erreur relative est réduite de 29.8 % à 6.8 %.

		mean (cm^{-1})	std. dev.
Uncorrected	iron	0.172	± 0.095
	air	0.085	± 0.004
Corrected	iron	0.414	± 0.032
	air	0.038	± 0.003
Mean spectrum value	iron	0.445	
	air	0.0001	

Table A.4: Moyenne et écart type des coefficients d'atténuation linéaire obtenues pour le fer et l'air sans correction et avec correction du diffusé objet et détecteur par la méthode des noyaux continus

A.5.4 Conclusions

La description analytique des noyaux de diffusé à l'aide d'un modèle à quatre Gaussienne permet de séparer la contribution à faible fréquence spatiale de l'objet et la con-

tribution plus haute fréquence du détecteur. Cette séparation des contributions est nécessaire pour bien corrigées les effets du rayonnement diffusé.

L'objet lui-même exige l'utilisation d'un modèle à deux Gaussiennes. Les paramètres d'amplitude A et B des noyaux augmentent avec l'augmentation de l'épaisseur de l'objet en raison de l'augmentation de la rapport diffusé sur primaire. σ_1 représente le contribution basse fréquence du diffusé de l'objet. Il correspond à la diffusion multiple des photons. σ_2 représente la contribution plus haute fréquence du diffusé de l'objet, σ_2 augmentent avec l'épaisseur de l'objet. Nous le relions à la contribution du diffusé simple de l'objet. De même, la contribution à haute fréquence du détecteur nécessite également un modèle à deux Gaussiennes. Les paramètres d'amplitude C et D, diminuent avec l'épaisseur. A cause de l'atténuation plus élevée, l'intensité du rayonnement primaire atteint moins le détecteur ce qui conduit à moins du diffusé Compton dans le détecteur et ses environs. En outre, D, qui pondère la contribution haute fréquence du détecteur, reste constant. Tandis que C, ayant un poids relativement plus faible, contribue la composante basse fréquence du détecteur et diminue en fonction de l'épaisseur traversée. Une explication à ce comportement pourrait être que C est liée à la rétrodiffusion de la plaque arrière. Le rayonnement rétrodiffusé de la plaque arrière diminue avec l'augmentation de l'énergie moyenne due à l'augmentation de l'épaisseur traversée. D pourrait être lié à fluorescence dans le scintillateur, qui reste constant en fonction de l'épaisseur. La contribution à haute fréquence du détecteur donné par σ_3, σ_4 reste constante .

En utilisant cette description analytique des noyaux du diffusé, les projections ont été corrigées pour des données utilisant un tube de 220 kV. Ceci a permis de faire une étude approfondie des contributions du diffusé de l'objet et du détecteur. La correction des projections en utilisant uniquement les noyaux diffusé de l'objet conduise à une image reconstruit avec des artefacts. L'erreur relative par rapport à la valeur attendue est de 32.5 % pour la correction du diffusé avec les noyaux d'objets. La correction des projections en utilisant les noyaux de diffusé de l'objet et du détecteur réduit l'erreur à 6.25 %. Les résultats obtenus ont été validés avec les résultats expérimentaux en utilisant un collimateur. L'erreur relative entre le résultat expérimental avec le collimateur et la correction du diffusé objet seul est 3.7 %. Ceci prouve que la correction du diffusé dû à l'objet ne suffit pas à éliminer complètement les artefacts dans la reconstruction. La contribution du diffusé du détecteur devient très important à la gamme d'énergie considérée.

A.6 Développement d'une méthode de correction du diffusé en combinant mesure et simulation Monte Carlo

Les résultats obtenus au chapitre **??** prouvent que la correction du diffusé de l'objet n'est pas suffisante pour éliminer complètement les artefacts dus au diffusé dans la reconstruction. Jusqu'à présent, les calculs des noyaux de diffusé ont été réalisées en utilisant des simulations Monte Carlo. On remarque que le diffusé du détecteur dépend de plusieurs paramètres : le spectre incident mais également les différents éléments composant le détecteur (filtre avant, plaque arrière, etc.). Ces derniers éléments sont très rarement divulgués par les constructeurs de détecteur plan. Par conséquent,

afin d'améliorer la méthode de correction, nous proposons une approche basé sur des mesures expérimentales et des simulations Monte Carlo. Les mesures expérimentales vont permettre d'estimer au mieux la contribution du détecteur. Les résultats obtenus prouvent la supériorité du modèle à quatre gaussienne pour prendre en compte efficacement à la fois la contribution du diffusé de l'objet et le détecteur par rapport à l'approche à deux gaussienne. L'étude prend compte également l'influence de la distance entre l'objet et le détecteur sur la description des noyaux de convolution.

A.6.1 Combinaison entre mesure et simulation

L'intensité mesurée I est la somme de la contribution du rayonnement primaire P et du rayonnement diffusé S :

$$I(x, y) = P(x, y) + S(x, y) \tag{A.14}$$

Le signal du diffusé peut être modélisé comme la somme du diffusé de l'objet et du détecteur. Pour chaque contribution, on peut associé à un poids qui correspond au ration entre le rayonnement diffusé (objet ou détecteur) et direct. En utilisant l'apporche continue décrite [75], le signal du diffusé total S peut être modélisé comme :

$$S(x, y) = P(x, y) \otimes K(x, y, T) = P(x, y) \otimes (K_o(x, y, T) + K_d(x, y, T)) \tag{A.15}$$

où, $\otimes$ représente le produit de convolution et K est dépendant de l'épaisseur traversée T qui tient compte de la contribution du diffusé de l'objet et du détecteur. L'indice d et o représente respectivement le détecteur et l'objet.

Le noyau du diffusé peut être réécrit comme

$$K(x, y, T) = k(T)\, K^*(x, y, T) \tag{A.16}$$

où, le poids $k(T)$ est appliqué au noyau normalisé à 1 K^* qui est la somme des poids correspondant au diffusé de l'objet $k_o(T)$ et du détecteur $k_d(T)$ de manière à ce que

$$k(T) = \iint K(x, y, T)\, \mathrm{d}x\, \mathrm{d}y = k_o(T) + k_d(T) \tag{A.17}$$

Pour déterminer le noyau du détecteur $K_d(x, y, T)$, on utilises le deux setup décrit à la figure A.20. Dans le dispositif décrit à la figure A.20a, une plaque de zirconium d'une épaisseur de 0,1 mm inclinée d'environ 5° par rapport de l'axe verticale a été placé devant les plaques en aluminium de différentes épaisseurs. Dans cette configuration, on obtient la Point Spread Function (PSF) qui tient compte du diffusé des objets et du détecteur. Dans le deuxième set-up décrit à la figure A.20b, la plaque de zirconium a été placée directement au contact du détecteur. Dans cette configuration, on obtient la contribution du diffusé du détecteur. ESF a été calculé pour les deux premiers les setups. Afin de réduire le bruit dans l'estimation des ESF, une centaine d'acquisitions ont été moyennée. La Line Spread Function (LSF) peut alors être déduite à partir de la dérivé de l'ESF.

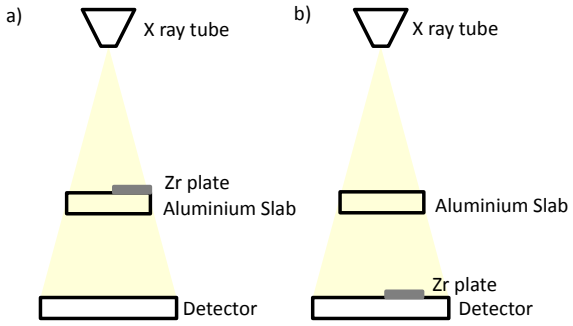

Figure A.20: Schéma de la configuration d'acquisition pour le calcul des noyaux expérimentaux

Les noyaux du diffusé de l'objet $K_o(x, y, T)$ sont obtenus à partir de simulations Monte Carlo comme décrit dans Bhatia et al. [75]. Pour chaque setup d'acquisition (Figure **??**) et pour chaque épaisseur, la LSF est obtenue en utilisant un ajustement au moindre carré avec un modèle à deux gaussienne.

$$LSF(x,T) = \sum_{i=1}^{2} A_i(T) \exp\left(-\frac{x^2}{2\sigma_i^2(T)}\right) \tag{A.18}$$

On doit noter que le modèle à deux gaussienne permet simplement de déterminer le poids $k(T)$ et ne sert pas à modéliser la forme du noyau. La relation entre la PSF et la LSF est donné par l'équation A.19

$$LSF(x,T) = \int_{-\infty}^{\infty} PSF(x,y,T)\mathrm{dy} \tag{A.19}$$

Cependant, en considérant une LSF décrite par 2 gaussienne on obtient

$$PSF(x,y,T) = \sum_{i=1}^{2} a_i(T) \exp\left(-\frac{x^2+y^2}{2\sigma_i^2(T)}\right) \tag{A.20}$$

où $a_i(T) = \dfrac{A_i(T)}{\sqrt{2\pi\sigma_i^2(T)}}$

Á partir de la PSF correspondant au setup de la figure A.20 a), nous obtenons l'équation suivante

$$W_a(T) = \iint PSF_a(x,y,T)\,\mathrm{d}x\,\mathrm{d}y \;\propto\; 1 + k_o(T) + k_d(T) \tag{A.21}$$

De manière similaire, à partir du setup de la figure A.20 b), on obtient

$$W_b(T) = \iint PSF_b(x,y,T)\,\mathrm{d}x\,\mathrm{d}y \;\propto\; 1 + k_d(T) \tag{A.22}$$

En combinant l'intégral de la PSF mesurée expérimentalement pour les deux setups, on a

$$\frac{W_b(T)}{W_a(T) - W_b(T)} = \frac{1 + k_d(T)}{k_o(T)} \tag{A.23}$$

Le poids de du diffusé de l'objet $k_o(T)$ est calculé à partir de simulations Monte Carlo (CIVA) et le poids du diffusé du détecteur $k_d(T)$ en utilisant l'équation suivante :

$$k_d(T) = \frac{W_b(T)}{W_a(T) - W_b(T)} k_o(T) - 1 \tag{A.24}$$

Le noyau final du diffusé détecteur peut être calculé comme

$$K_d(x, y, T) = (1 + k_d(T))\, PSF_b^*(x, y, T) - \delta[x, y] \tag{A.25}$$

où $\delta[x, y]$ est la fonction de Kronecker qui nulle partout sauf pour $x = 0$ et $y = 0$ où la fonction vaut 1. Le terme * correspond à une PSF normalisée à 1.

A la place d'utiliser la loi de Beer-Lambert basée sur un coefficient d'atténuation linéaire μ, l'épaisseur T à chaque pixel est directement calculée à partir de la table de conversion f_{BH} – calculée avec CIVA pour différentes épaisseurs de cales.

$$T(x, y) = f_{BH}\left(\frac{P(x, y)}{O(x, y)}\right) \tag{A.26}$$

où O est l'image non atténuée. On peut noter que le durcissement de faisceau est pris en compte dans cette procédure. Les paramètres d'acquisition et le matériau de l'objet doit être le même pour la phase de calibration et pour la tomographie. La valeur de l'intensité du faisceau directement transmis P est calculé pour chaque épaisseur ce cales simulées. L'épaisseur en fonction de la transmittance $P(x, y)/O(x, y)$ est donc calculée comme décrit dans la section A.6.5.

Les noyaux de convolution finaux sont ensuite ajusté à partir d'un modèle à quatre gaussienne comme le montre l'équation suivante

$$K(x, y, T) = \sum_{i=1}^{2} w_{d,i}(T) \exp\left(-\frac{x^2 + y^2}{2\sigma_{d,i}^2(T)}\right) + \sum_{i=1}^{2} w_{o,i}(T) \exp\left(-\frac{x^2 + y^2}{2\sigma_{o,i}^2(T)}\right) \tag{A.27}$$

où,

$$k_d(T) = 2\pi(w_{d,1}(T)\sigma_{d,1}^2(T) + w_{d,2}(T)\sigma_{d,2}^2(T)) \tag{A.28}$$

et

$$k_o(T) = 2\pi(w_{o,1}(T)\sigma_{o,1}^2(T) + w_{o,2}(T)\sigma_{o,2}^2(T)) \tag{A.29}$$

Pour générer une description continue des noyaux [75], les facteurs d'amplitude, w_d et w_o et de forme σ_d et σ_o sont également estimés en fonction de l'épaisseur traversée dans l'objet.

A.6.2 Estimation des noyaux de convolution en focntion de la distance objet-détecteur

Les acquisitions pour calculer les noyaux de convolution peuvent ennuyeuses et consommatrices de temps surtout si l'on souhaite faire des acquisitions avec différents grandissement. Nous proposons une solution simple et pratique pour corriger le diffusé en décrivant de manière analytiques les facteurs de forme et d'amplitude en fonction de

la distance objet-détecteur que nous noterons d_{OD}. Pour cela, nous utilisons le setup d'acquisition présenté à la figure 4.1 b). Puis, nous estimons analytiquement par une régression au moindre carré les paramètres des noyaux du diffusé de l'objet en fonction de d_{OD}. Les objets dans ce cas sont des cales parallélépipédique placées au centre de l'axe de rotation.

Les facteurs d'amplitude des noyaux de l'objet sont supposé être décroissant quand d_{OD} augmente. A contrario, les facteurs de forme doivent augmentés avec l'augmentation de la distance d_{OD}.

Nous décrivons la variation de ces paramètres à l'aide de fonctions puissance comme proposé à l'équation suivante :

$$p(T, d_{OD}) = p(T, 0) d_{OD}^{\alpha} \tag{A.30}$$

où $p \in \{w_{o,1}, w_{o,2}, \sigma_{o,1}, \sigma_{o,2}\}$ sont dépendant de l'épaisseur traversée T (comme le sont les paramètres des noyaux de convolution) et α est le poids de la fonction puissance. En toute logique, nous devons avoir α négatif pour les termes d'amplitude et positifs pour les termes de forme.

A.6.3 Approche expérimentale seule : modèle à deux gaussienne

De l'optique de proposer une approche expérimentale seule, nous calculons le facteur de poids $\bar{k}(T)$ en utilisant le ratio entre la transmittance experimentale et théorique calculé avec la loi de Beer-Lambert :

$$\bar{k}(T) = \frac{E_{trans}(T)}{T_{trans}(T)} - 1 \tag{A.31}$$

où, $E_{trans}(T)$ représente la transmittance expérimentale et $T_{trans}(T)$ est la transmittance théorique selon la loi de Beer-Lambert.

La transmittance expérimentale est calculée à partir des acquisitions obtenues avec le setup A.20 a).

$$E_{trans}(T) \propto \frac{W_a(T)}{W_a(0)} \propto \frac{1 + k_o(T) + k_d(T)}{1 + k_d(0)} \tag{A.32}$$

En utilisant l'équation A.31, $\bar{k}(T)$ correspond à

$$\bar{k}(T) = \frac{k_o(T) + k_d(T) - k_d(0)}{1 + k_d(0)} \tag{A.33}$$

On fait l'approximation que $\bar{k}(T) \simeq k(T)$ car en réalité $k_d(0) \neq 0$.

Les noyaux de convolution obtenus à la figure A.20 a) sont estimés au sens des moindres carrés à partir d'un modèle à deux gaussienne comme présentée à la figure suivante :

$$K(x, y, T) = w_{d,1}(T) \exp\left(-\frac{x^2 + y^2}{2\sigma_{d,1}^2(T)}\right) + w_{o,1}(T) \exp\left(-\frac{x^2 + y^2}{2\sigma_{d,1}^2(T)}\right) \tag{A.34}$$

où,

$$\bar{k}(T) = 2\pi(w_{d,1}(T)\sigma^2_{d,1}(T) + w_{o,1}(T)\sigma^2_{o,1}(T)) \tag{A.35}$$

Les résultats obtenus avec cette méthode seront comparés au modèle à quatre gaussienne présenté à la section A.6.1.

A.6.4 Le matériel utilisé

Les acquisitions ont été réalisé avec une tube à rayons X, un plateau tournant et un détecteur plan. Le tube à rayons X a été reglé à une haute tension de 150 kV et une intensité de 750 µA pour une taille de foyer de 120 µm environ. Nous avons utilisé un filtre en aluminium d'épaisseur 1,5 mm en plus de la filtration inhérente du tube. La figure A.21 montre le spectre simulé avec MCNP [7] tenant compte des différents filtres. La figure A.22 montre la variation du coefficient d'atténuation massique en fonction de l'énergie des photons. Les données proviennent des tables du NIST [2]. Le detecteur présente une matrice de 1024 × 1024 pixel, chaque pixel de forme carré présente une taille 0,2 mm de côté.

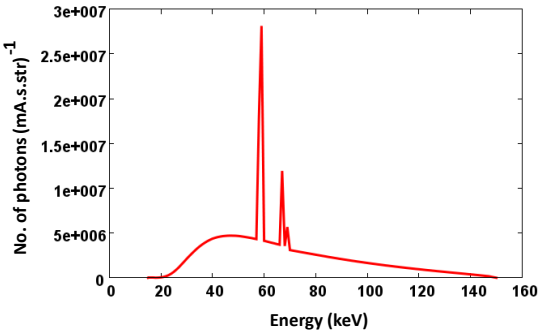

Figure A.21: Spectre simulé avec des filtres internes et externes à 150 kV tension de source avec MCNP[7]

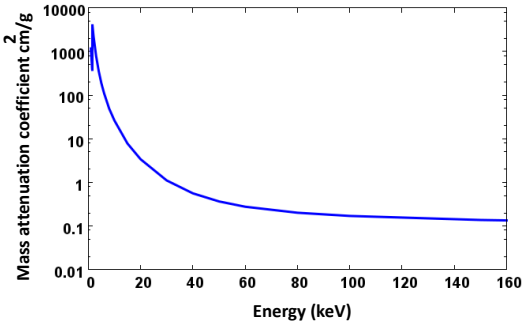

Figure A.22: Variation du coefficient d'atténuation de masse de l'aluminium sur l'énergie

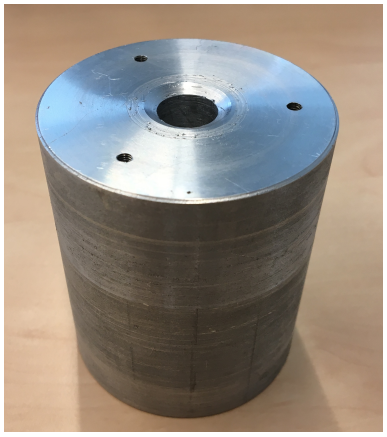

Figure A.23: L'image de l'échantillon de cylindre en aluminium avec des trous d'air

Les acquisitions ont été réalisé sur un cylindre d'aluminium (voir figure A.23 de diamètre 60 mm comportant un trou cylindrique central de diamètre 10 mm et 3 trous périphériques de 3 mm de diamètre. Deux acquisitions à deux grandissements différents ont été réalisé. Dans le premier cas, la distance d_{OD} était de 95 mm dans le second 295 mm. La distance entre la source et le détecteur est restée fixe à 600 mm.

A.6.5 Résultats

Correction du durcissemnt de faisceau

Pour calculer l'épaisseur traversé dans chaque pixel, nous avons utilisé le résultats des simulations. Les valeurs du flux directement transmis P ont été calculées pour chaque épaisseur de cale simulée. L'épaisseur en fonction de la transmittance LUT f_{BH} est donnée par l'équation **??**. Elle a été estimé numériquement à l'aide d'une régression aux moindres carrés comme présenté à la figure **??**. L'équation classique

Table A.5: Le tableau donne la valeur des poids $k(T)$ et $k_d(T)$ en utilisant les aires des PSF $W_a(T)$ et $W_b(T)$ ainsi que les poids du diffusé de l'objet obtenues par simulation $k_o(T)$ pour différentes épaisseurs de matière traversées

Thickness(mm)	$W_a(T)$ (pixel^2)	$W_b(T)$ (pixel^2)	$k_o(T)$	$k_d(T)$	$k(T)$
10	1867	1760	0.12	0.99	1.12
26	621	555	0.32	1.68	2.00
42	587	493	0.70	3.27	3.02
58	955	807	1.10	4.99	6.10

issu de la loi de Beer-Lambert est également présentée en bleu sur la figure **??**. Le phénomène de durcissement de faisceau n'est pas très important dans ce cas de figure. L'équation A.36 donne la relation est l'épaisseur T en fonction de la transmittance $P(x,y)/O(x,y)$.

$$\begin{aligned} T(x,y) &= f_{BH}\left(\frac{P(x,y)}{O(x,y)}\right) \\ &= b\left(\log\left(\frac{P(x,y)}{O(x,y)}\right)\right) + c \end{aligned} \tag{A.36}$$

avec $b = -14.1$, $c = 1.14$

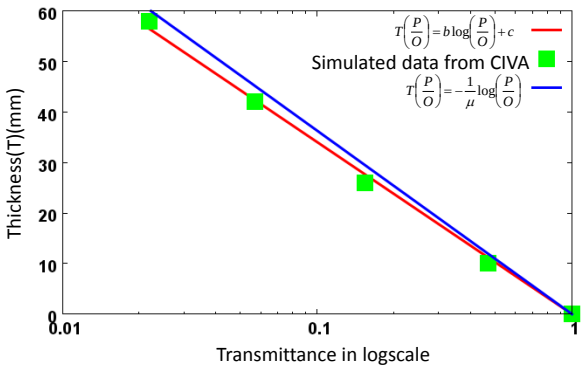

Figure A.24: L'épaisseur en fonction de la transmittance

Modèle à quatre gaussienne

Le tableau A.5 donne la valeur des poids $k(T)$ et $k_d(T)$ en utilisant les aires des PSF $W_a(T)$ et $W_b(T)$ ainsi que les poids du diffusé de l'objet obtenues par simulation $k_o(T)$ pour différentes épaisseurs de matière traversées en utilisant l'équation A.24.

La description à l'aide d'un modèle à quatre gaussienne au lieu de deux seulement permet de séparer la contribution basse fréquence due au diffusé de l'objet de la contribution haute fréquence du détecteur. Nous pouvons constater que le modèle à deux gaussienne n'est pas suffisant pour rendre compte du diffusé de l'objet. Le tableau A.6 montre une comparaison des paramètres estimés pour une épaisseur de 10 mm et 42 mm avec un modèle à deux gaussienne et quatre gaussienne pour les noyaux du

détecteur et de l'objet (tous sont simulés avec CIVA). Ce tableau montre également le paramètre du noyau de l'objet seule. Nous peut noter que le modèle à deux gaussienne utilise uniquement les termes $w_{(d,1)}$ and $w_{(d,2)}$ et néglige les termes de l'objet $w_{(o,1)}$ and $w_{(o,2)}$. Nous notons également une sous-estimation de la contribution du détecteur avec la simulation CIVA en comparaison avec les mesures expérimentales.

Table A.6: Paramètres pour les noyaux simulés pour le modéle à les deux gaussien et quatre gaussien

Thickness (mm)	Model	Detector				Object			
		$w_d(1)$ $\times 10^{-3}$	$w_d(2)$ $\times 10^{-1}$	$\sigma_d(1)$	$\sigma_d(2)$ $\times 10^{-1}$	$w_o(1)$ $\times 10^{-4}$	$w_o(2)$ $\times 10^{-4}$	$\sigma_d(2)$ $\times 10^{1}$	$\sigma_d(2)$ $\times 10^{1}$
10	Two-Gaussian	0.085	4.5	2.1	4.7				
	Four-Gaussian	0.076	4.2	2.5	4.8	0.27	2.0	1.0	2.9
	Two-Gaussian					0.25	1.8	1.0	2.9
46	Two-Gaussian	1.8	1.3	4.6	4.8				
	Four-Gaussian	1.7	1.2	4.6	4.9	1	2.6	1.9	4.8
	Two-Gaussian					1	2.7	4.8	5.0

Nous avons utilisé un modèle à quatre gaussienne composé d'un premier modèle à deux gaussienne décrivant le détecteur obtenu expérimentalement à l'aide du setup décrit à la figure A.20 b) et également un modèle à deux gaussienne du diffusé de l'objet obtenu avec des simulations Monte Carlo via CIVA. La figure A.25 montre les noyaux du détecteur pour différentes épaisseurs de matières traversées. La figure A.26 montre l'évolution des paramètres estimés des noyaux. La figure A.27 montre les noyaux du diffusé objet simulé et la figure A.28 montre l'évolution des paramètres pour les noyaux simulés du diffusé de l'objet.

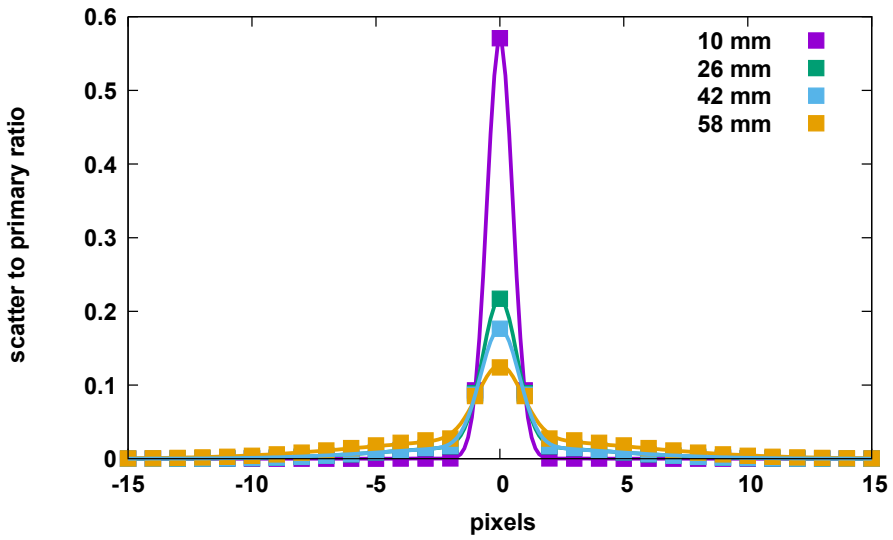

Figure A.25: Profils extraits de kernel expérimentales de le detecteur pour différentes épaisseurs de mise en place en Figure 4.1 b)

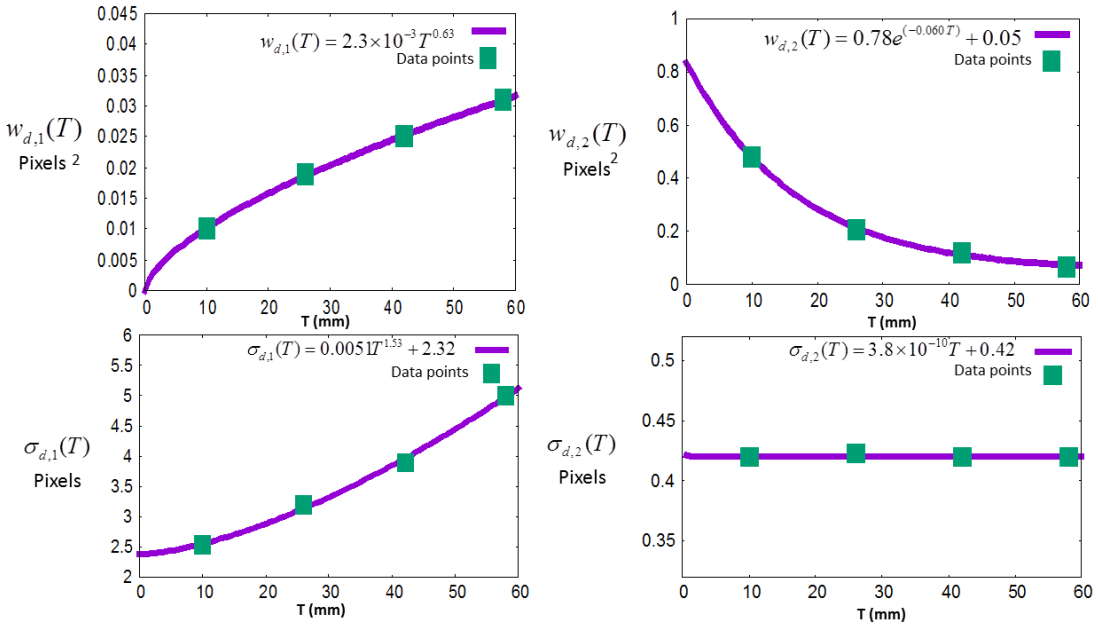

Figure A.26: Paramètres de montage de kernel expérimentales de le detecteur utilisant deux gaussien par rapport à l'épaisseur de la mise en place dans Figure 4.1 b)

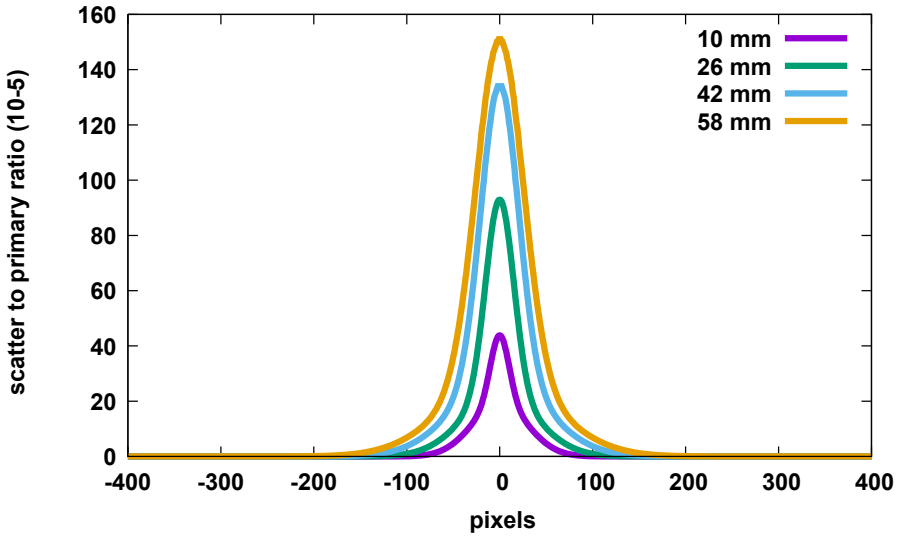

Figure A.27: Profils extraits de kernel simuleé de l'objet pour différentes épaisseurs

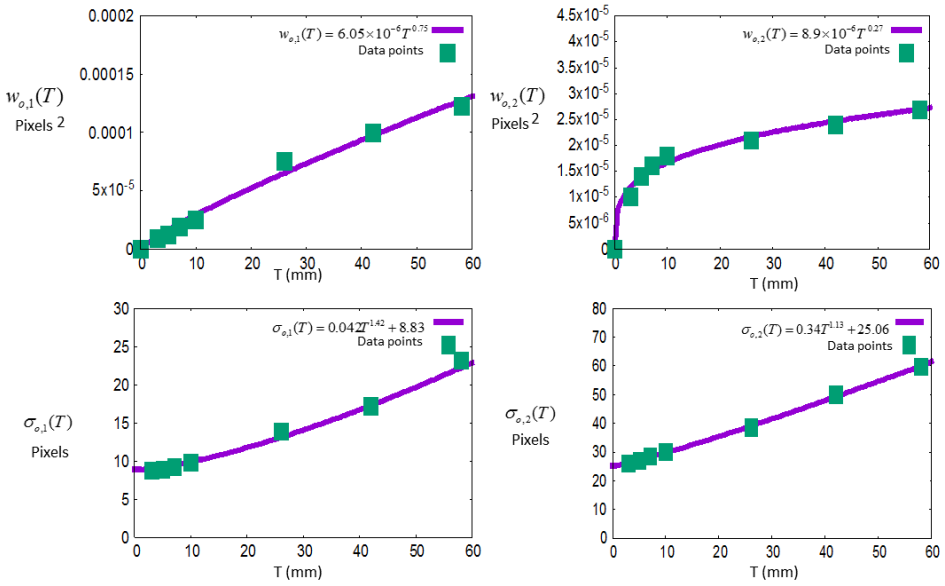

Figure A.28: Paramètres de montage de kernel simuleé de l'objet utilisant deux gaussien par rapport à l'épaisseur

Estimation continue des noyaux en fonction de la distance objet-détecteur

Comme décrit à la section A.6.2, nous proposons une description continue des paramètres des noyaux en fonction de la distance objet-détecteur d_{OD} afin de rendre notre approche la plus flexible possible en vue d'une utilisation industrielle. La figure A.29 montre le noyau du diffusé de l'objet pour 10 mm d'aluminium pour différentes distances d_{OD}. La figure A.29 montre les noyaux normalisés à la valeur centrale pour $d_{OD} = 95mm$.

La figure A.30 donne l'évolution des paramètres estimés des noyaux du diffusé objet pour une épaisseur de 10 mm en fonction de d_{OD}. Les paramètres sont estimés analytiquement avec une fonction puissance dépendant de d_{OD} comme indiqué à l'équation A.30. Pour réaliser cela, nous avons utilisé quatre grandissement différents. La figure A.31 montre la valeur absolue de l'erreur relative en pourcent entre les noyaux obtenus par simulation et par le modèle analytique.

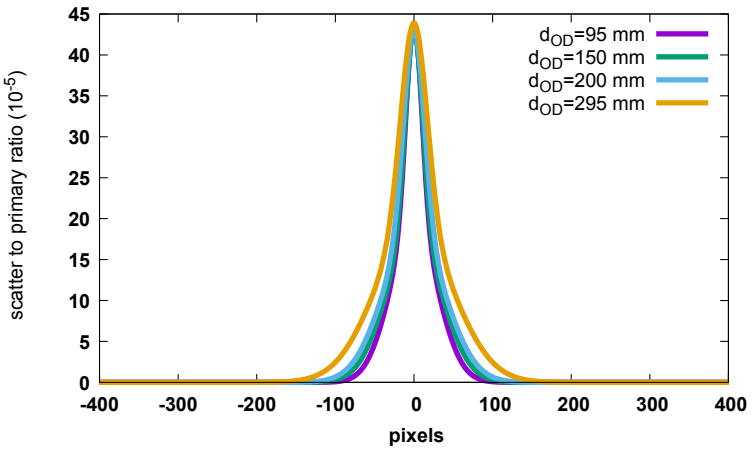

Figure A.29: Kernel de l'objet normlisé sur distance de object a detecteur simulé avec CIVA

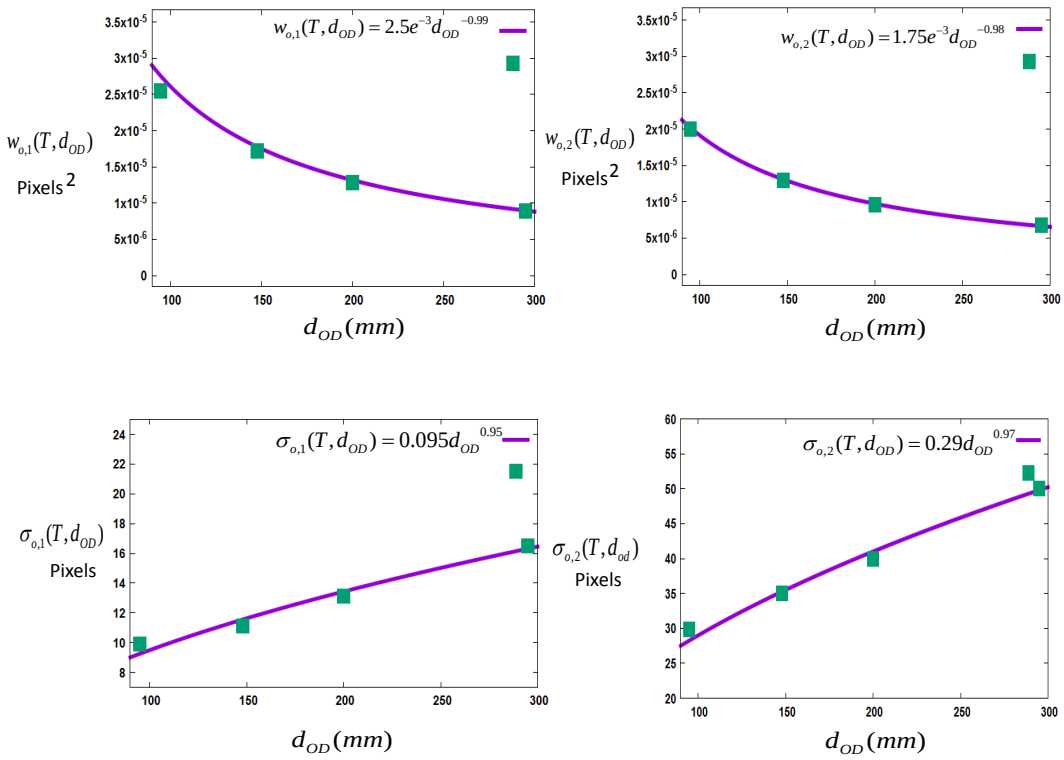

Figure A.30: Paramètres de montage de kernel simuleé de l'objet sur distance de object a detecteur simulé avec CIVA

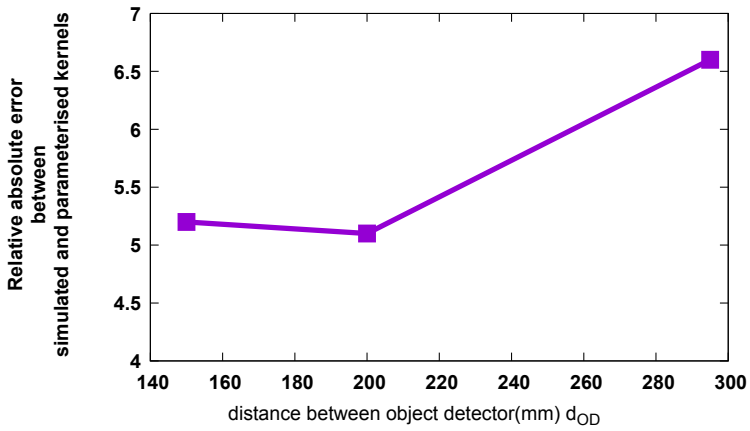

Figure A.31: Erreur absolue relative entre les kernels simulés et paramétrés pour $T = 10$ mm slab

Correction du diffusé sur le cylindre d'aluminium

La figure A.32 a) montre une coupe reconstruite sans correction des projections. La courbe rouge à la figure A.33 montre un profil extrait de la coupe reconstruite mettant en avant un effet cuvette assez prononcé. La courbe verte de la figure A.33 montre les résultats obtenus avec la correction du durcissment de faisceau seulement. La figure A.32 b) montre la reconstruction obtenue après correction du durcissement de faisceau et du diffusé avec un modèle à deux gaussienne. La figure A.32 c) montre

la reconstruction obtenue après correction du durcissement de faisceau et du diffusé à partir du modèle à quatre gaussienne.

Les profils extraits des reconstruction obtenues après correction du diffusé sur un modèle deux et quatre gaussienne sont présentés à la figure A.33.

Le tableau A.7 montrent les moyennes et écarts type obtenus pour l'air et l'aluminium pour les reconstruction corrigés et non corrigé. Dans la reconstruction non corrigée, on estime le coefficient d'atténuation linéïque de l'aluminium à $0,41$ cm^{-1}. En utilisant le modèle à deux gaussienne, nous obtenons une valeur de $0,55$ cm^{-1}. Dans la gamme d'énergie considérée ($E \in$ [64 keV, 94keV]), la valeur théorique se situe entre $0,5$ cm^{-1} pour une énergie moyenne de 64 keV et $0,7$ cm^{-1} pour une énergie moyenne de 94 keV. L'erreur relative en pourcent est approximativement de 10% pour le modèle à deux gaussienne. Avec le modèle à quatre gaussienne, nous obtenons une valeur de $0,62$ cm^{-1} pour l'aluminium. L'erreur relative est réduite à 3.4 %.

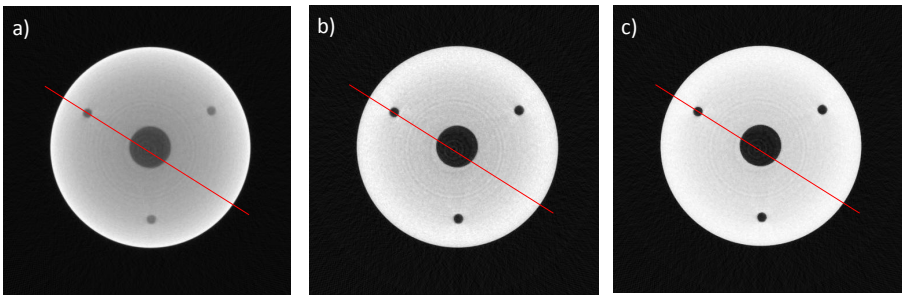

Figure A.32: Coupé de reconstruction pour a) projections non corrigeé b) correction de diffusé utilisant le modèle à deux gaussienne c) correction de diffusé utilisant le modèle à quatre gaussienne

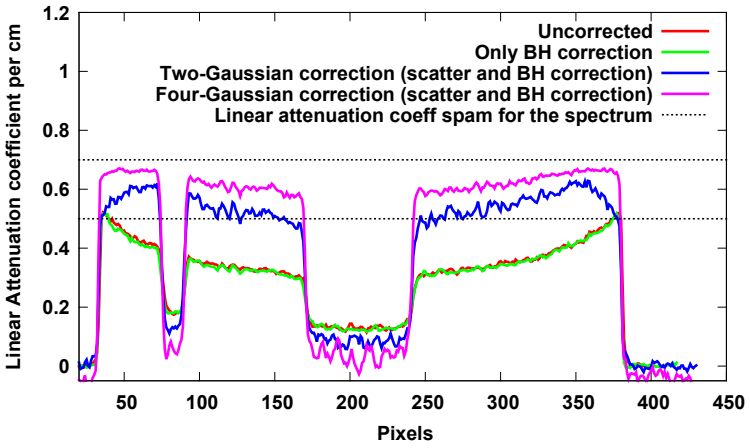

Figure A.33: Profils extraits de la coupe reconstruites à partir des projections non corrigées et corrigées

Table A.7: Les valeurs moyennes et d'écart-type pour l'aluminium et de la région d'air pour non corrigées et les tranches de reconstruction corrigées

		mean (cm^{-1})	std. dev.
Uncorrected	air	0.132	± 0.002
	aluminum	0.413	± 0.007
Two-Gaussian correction	air	0.062	± 0.006
	aluminum	0.552	± 0.005
Four-Gaussian correction	air	0.060	± 0.006
	aluminum	0.622	± 0.009
Mean spectrum value	air	0.0001	
	aluminum	0.614	

La figure **??** montre la reconstruction obtenue avec les noyaux du diffusé objet obtenus par simulation à la distance objet-détecteur de 295 mm et la reconstruction obtenue avec les noyaux de diffusé estimés par l'approche décrite dans la section A.6.5 (en utilisant un modèle à quatre gaussienne). La figure A.35 montre les profils extraits de ces deux reconstructions. Les deux reconstructions sont équivalentes ce qui valident notre approche par une description continue des noyaux de convolution en fonction de la distance objet-détecteur.

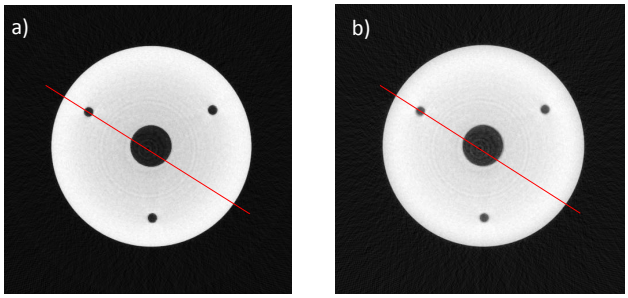

Figure A.34: Coupé de reconstruction pour a) kernels simuleé b)kernels parametereé en fonction de la distance objet-détecteur

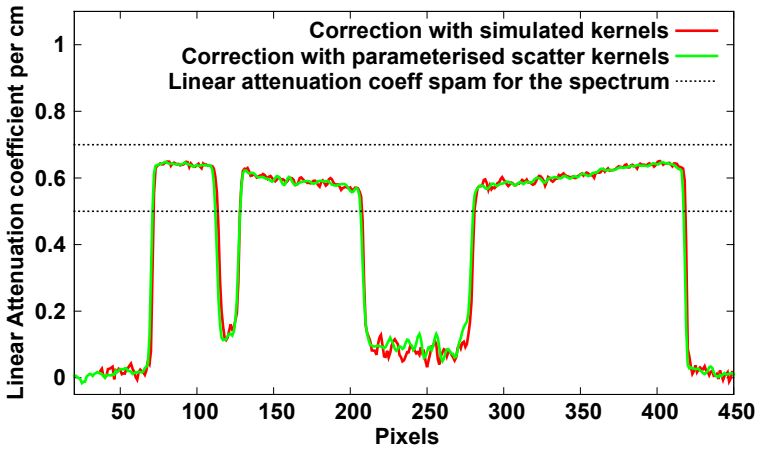

Figure A.35: Profils extraits de la coupe reconstruites kernels simuleé et kernels parametereé en fonction de la distance objet-détecteur

Ce travail a été soumis au journal NDT& E le 24 juin 2016. Le lecteur intéressé pourra se reporter au chapitre 5.

A.7 Conclusion et perspectives

Dans cette thèse, nous avons d'abord présenté une revue de la plupart des techniques de correction du diffusé en CBCT en précisant leurs avantages, les inconvénients et la portée des applications. Les techniques sont globalement divisés en deux sections : pré-traitement et post-traitement. Ce travail a démontré que la méthode SKS offre un bon compromis entre l'efficacité, le coût de calcul et la facilité de mise en œuvre parmi toutes les méthodes décrites. L'applicabilité sur une large gamme de conditions d'acquisition donne un avantage supplémentaire. Cet approche permet de ne rien ajouter au setup expérimentale et ne nécessite pas plusieurs acquisitions.

La principale limite du modèle SKS vient de son efficacité limitée dans le calcul de la distribution de diffusé pour les géométries complexes. Plusieurs modifications de cet méthode SKS ont été adaptées pour résoudre ce problème qui inclut l'utilisation de noyaux non stationnaires ou paramétriques libres. Cependant, à cause d'un ratio diffusé sur primaire élevé comme souvent rencontré en tomographie industrielle, les différentes étapes de l'algorithme de correction SKS doivent être réexaminées dans l'estimation des noyaux de convolution. En particulier, un meilleur échantillonnage des noyaux en fonction de l'épaisseur de l'objet est nécessaire pour obtenir un modèle précis de la variabilité de la forme et de l'amplitude des noyaux de diffusé sur toute la gamme d'épaisseurs considérée.

Nous proposons une description analytique des noyaux de diffusé qui sont estimés en termes d'épaisseur de matériau pour former une description continue adaptée. Cette approche a prouvé son efficacité pour produire un meilleur échantillonnage des noyaux par rapport à l'épaisseur de l'objet. En conséquence, à la fois l'amplitude et la distribution de la forme du diffusé peuvent être efficacement calculées pour des géométries complexes. Les corrections du diffusé sont effectuées en utilisant cette approche et les résultats obtenus sont comparés à l'approche classique.

La correction du diffusé avec cette approche conduit à une très notable amélioration de la qualité de la reconstruction en particulier sur les bords des objets où la variation de l'épaisseur de l'objet est plus élevée. En conséquence, les valeurs d'atténuation linéïque obtenues avec cette correction sont également plus proche de la valeur théorique. Cette méthode a également été appliquée des objets multimateriaux. Dans la gamme d'énergie considéré, l'effet Compton est prédominant. Dans cette gamme d'énergie, les noyaux sont considérés comme équivalents pour une épaisseur d'atténuation équivalente. De plus, nous avons mis en œuvre une approche itérative multiplicative pour résoudre le problème de l'estimation négative du primaire dans le processus d'itération qui peut être possible lorsque le ratio diffusé sur directe est important.

De plus, nous avons amélioré la compréhension de notre approche en menant une étude pour identifier les contributions respectives du diffusé de l'objet et du détecteur en utilisant un modèle à quatre gaussienne. Une première approche a été réalisée en utilisant des simulations MC pures pour le calcul des noyaux de diffusé pour détecteur et l'objet. La correction du diffusé a démontré une contribution majeure du diffusé provenant du

détecteur. Les résultats obtenus ont également été validés expérimentalement en utilisant un collimateur. Ce travail a été publié dans la revue, JXST en 2016.

La correction du diffusé effectuée sur la base de simulations est fortement dépendante de la précision de la géométrie du détecteur. Les éléments composants le détecteur sont des éléments tenu secret, la plupart du temps, par les constructeurs. Afin d'améliorer encore notre approche dans le calcul de la contribution du diffusé du détecteur, nous avons utilisé des acquisitions pour calibrer les poids des noyaux du diffusé du détecteur.

Dans cette travail de thèse, nous avons développé une méthode de correction du diffusé flexible et adaptable à de nombreux cas rencontrés en tomographie industrielle (100 keV-6 MeV). La méthode développée s'applique sur les projections, elle est donc indépendante de l'algorithme de reconstruction utilisée ensuite. La méthode nécessite de simuler que quelques cas (typiquement 5) dans la gamme d'épaisseur considérée. La simulation peut être réalisé avec des codes accessibles et peu onéreux(GEANT4, MCNP, PENELOPE). La méthode peut être affinée avec des mesures expérimentales simples. La méthode fonctionne avec des objets polymatériaux.

Le modèle basé sur la carte continue du noyau est fortement dépendante du calcul correct de l'épaisseur à chaque pixel. Dans la première approche, nous avons adopté la méthode simple de calcul d'épaisseur en utilisant la loi de Beer-Lambert. Pour tenir compte davantage de l'effet de durcissement du faisceau de l'épaisseur a été calculée sur la base des tables de consultation. Cependant, cette approche est également limitée sur la modélisation du spectre du logiciel simulant. Une des méthodes de calcul de l'épaisseur au niveau de chaque pixel peut se faire par l'utilisation de la méthode de lancer de rayon, qui calcule l'épaisseur de l'objet en se basant sur les points du rayon direct passant à travers l'objet à l'étude d'interaction.

Ce travail pourrait être complété par une étude des facteurs influents sur le diffusé du détecteur (plaque arrière, fenêtre d'entrée). L'étude pourrait se poursuivre pour des applications à basse énergie (<100keV) où l'effet photoélectrique et l'effet Rayleight sont prédominant. Il serait intéressant de poursuivre ce travail dans la gamme d'énergie 6-30 MeV. Dans cette gamme d'énergie les processus électroniques comme le rayonnement de freinage deviennent non négligeable. CIVA ne tenant pas compte de ces processus, il faudra simuler les noyaux avec des codes plus complet comme MCNP ou Penelope. Ce travail de thèse pourrait être également insérer dans CIVA afin de le rendre accessible au plus grand nombre.

Bibliography

[1] J J Lifton. The influence of scatter and beam hardening in X-ray computed tomography for dimensional metrology. University of Southampton, Engineering and the Environment, Doctoral Thesis. 2015. x, xii, 3, 5, III

[2] M J Berger, J H Hubbell, and S M Seltzer et al. NIST XCOM: photon cross sections database. *NIST*, 2016. x, xi, 6, 67, XXIX

[3] http://www-civa.cea.fr/. x, 7, 25, 44, VII, XIII

[4] M Costin and D Tisseur et al. Civa CT, an advanced simulation platform for NDT. *iCT*, 2016. x, 7

[5] M Sun and J M Star-Lack. Improved scatter correction using adaptive scatter kernel superposition. *Phys Med. Biol*, 55:6675 – 6720, 2010. x, xi, 15, 16, 17, 18, 20, 22, 23, 27, 39, 42, 43, 44, 61, 65, 83, IV, V, XI, XII

[6] A Peterzol, J M Létang, and D Babot. A beam stop based correction procedure for high spatial frequency scatter in industrial cone-beam X-ray CT. NIMB, 266:4042 – 4054, 2008. x, xii, 13, 28, 35, IV, VIII, X

[7] J F Briesmeister. MCNP-A general Monte Carlo code for neutron and photon transport. 1986. xi, xiii, 67, XXIX

[8] R Gordon, R Bender, and G.T Herman. Algebraic Reconstruction Techniques (ART) for three-dimensional electron microscopy and X-ray photography. *J. theor. Biol.*, 29:471–481, 1970. 6, II

[9] T M Buzug. Computed tomography: From photon statistics to modern conebeam CT. *1st edition. Springer*, 2008. 6

[10] A C Kak and M Slaney. Principles of computerized tomographic imaging. *1st edition. IEEE Press, New York,*, 1988. 6, II

[11] L A Feldkamp, L C Davis, and J W Kress. Practical cone-beam algorithm. *JOSA A*, 1:612–619, 1984. 6, 22, 48, 58, 61

[12] F Xu, W Xu, and K Mueller et al. On the efficiency of iterative ordered subset reconstruction algorithms for acceleration on GPUs. *Computer Methods and Programs in Biomedicine*, 98:261–270, 2010. 7

[13] C L Byrne. Iterative image reconstruction algorithms based on cross-entropy minimization. *TMP*, 2:261–270, 1993. 7

[14] E Y Sidky, C M Kao, and X Pan. Accurate image reconstruction from few-views and limited-angle data in divergent-beam CT. *JXST*, 14:119–139, 2006. 7

[15] R Schulze, U Heil, D D Bruellmann, E Dranischnikow, U Schwanecke, and E Schoemer. Artefacts in CBCT: a review. *DMFR*, 40:265–273, 2011. 8

[16] R L McKinley, M P Toraai, E Samei, and M L Bradshaw. Initial study of quasi-monochromatic X-ray beam performance for X-ray computed mammotomography. *TNS*, 52:1243–1250, 2005. 8

[17] G Zentai. Signal-to-Noise and contrast ratio enhancements by quasimonochromatic imaging. *TIM*, 60:908–915, 2011. 8

[18] G T Herman. Correction for beam hardening in computed tomography. *Phys.Med. Biol.*, 24:81–106, 1979. 8

[19] P Hammersberg and M Mangard. Correction for beam hardening artefacts in computerised tomography. *JXST*, 8:75–93, 1998. 8

[20] J M Meagher, C D Mote, and H B Skinner. CT image correction for beam hardening using simulated projection data. *TNS*, 37:1520–1524, 1990. 8

[21] J Hsieh, R C Molthen, C A Dawson, and R H Johnson. An iterative approach to the beam hardening correction in cone beam CT. *Med. Phys.*, 27:23–29, 2000. 8

[22] A J Coleman and M Sinclair. A beam-hardening correction using dual-energy computed tomography. *Phys. Med. Biol.*, 30:1251–1256, 1985. 8

[23] A Bub, S Gondrom, M Maisl, N Uhlmann, and W Arnold. Image blur in a flat-panel detector due to Compton scattering at its internal mountings. *MST*, 18:1270–1277, 2007. 10, 42, XI

[24] P Wils, J M Létang, and J P Bruandet. Secondary radiations in cone-beam computed tomography: simulation study. *JEI*, 21:021113, 2012. 10, 42, XI

[25] G Poludniowski, P M Evans, A Kavanagh, and S Webb. Removal and effects of scatter-glare in cone-beam CT with an amorphous-silicon flat-panel detector. *Med. Phys.*, 56:1837–1851, 2011. 10, 16, 18, 42, 61, IV, V, XI

[26] M Hoheisel, A Korn, and J Giersch. Influence of backscattering on the spatial resolution of semiconductor X-ray detectors. *NIMB*, 546:252–257, 2005. 10, 42, XI

[27] D Nikolopoulos, I Kandarakis, and D Cavouras et al. Investigation of radiation absorption and X-ray fluorescence properties of medical imaging scintillators by Monte Carlo methods. *NIMB*, 565:821 – 832, 2006. 10, 14, IV

[28] J M Boone, J A Seibert, J M Sabol, and M Tecotzky. A Monte Carlo study of X-ray fluorescence in X-ray detectors. *Med. Phys.*, 26:905–916, 1999. 10

[29] R Luhta and J A Rowlands. Origins of flare in X-ray image intensifiers. *Med. Phys.*, 17:913–921, 1990. 10

[30] L Dimitrios and W F Jeffrey. Impact of flat panel-imager veiling glare on scatter-estimation accuracy and image quality of a commercial on-board cone-beam CT imaging system. *Med. Phys.*, 39:5639–5651, 2012. 10

[31] L C Alexander, J M Boone, and N Shah. Evaluation of X-ray scatter properties in a dedicated cone-beam breast ct scanner. *Med. Phys.*, 32:2967–2975, 2005. 11

[32] S Z Shen, A K Bloomquist, G E Mawdsley, J M Yaffe, and I Elbakri. Effect of scatter and an antiscatter grid on the performance of a slot-scanning digital mammography system. *Med. Phys.*, 33:1108–1115, 2006. 11

[33] H P Chan and K Dio. Investigation of the performance of antiscatter grids: Monte carlo simulation studies. *Phys. Med. Biol.*, 27:785–803, 1982. 11

[34] H P Chan, Y Higashida, and K Dio. Performance of anti-scatter grids in diagnostic radiology: Experimental measurements and Monte Carlo simulation studies. *Med. Phys.*, 12:449–454, 1985. 11

[35] J M Boone and O V Makarova et al. Development and monte carlo analysis of antiscatter grids for mammography. *TCRT*, 1:441–7, 2002. 11

[36] J Wiegert, M Bertram, D Schaefer, N Conrads, J Timmer, T Aach, and G Rose. Performance of standard fluoroscopy antiscatter grids in flat-detector-based cone-beam CT. *Proc. SPIE*, 5368:67–78, 2004. 11

[37] Ulrich Neitzel. Grids or air gaps for scatter reduction in digital radiography: A model calculation. *Med. Phys.*, 19:475–81, 1992. 11

[38] A Krol, D A Bassano, C C Chamberlain, and S C Prasad. Scatter reduction in mammography with air gap. *Med. Phys.*, 23:1263–1270, 1996. 11

[39] J A Sorenson and J Floch. Scatter rejection by air gaps: an empirical model. *Med. Phys.*, 12:308–16, 1985. 11, 12

[40] R Chityala, K.R Hoffmann, D R Bednarek, and S Rudin. Region of interest (ROI) computed tomography. *Proc SPIE*, 5368:534–41, 2004. 12

[41] L Chen, C C Shaw, and M C Altunbas. Feasibility of volume of interest (VOI) scanning technique in cone beam breast CT—a preliminary study. *Med. Phys.*, 35:3482–90, 2008. 12

[42] D Kolditz, Y Kyriakou, and W A Kalender. Volume-of-interest VOI imaging in c-arm flat-detector CT for high image quality at reduced dose. *Med. Phys.*, 37:2719–30, 2010. 12

[43] C J Lai, L Chen, and H Zhang. Reduction in X-ray scatter and radiation dose for volume-of-interest (VOI) cone-beam breast CT—a phantom study. *Phys. Med. Biol.*, 54:6691–709, 2009. 12

[44] J S Maltz, B Gangadharan, and M Vidal et al. Focused beam-stop array for the measurement of scatter in megavoltage portal and cone beam CT imaging. *Med. Phys.*, 35:2452–2462, 2008. 13, IV

[45] R Ning, X Tang, and D L Conover. X-ray scatter suppression algorithm for cone-beam volume CT. *SPIE Proceedings, Bellingham, WA*, pages 774–81, 2002. 13, IV

[46] R Ning, X Tang, and D L Conover. X-ray scatter correction algorithm for cone-beam volume ct. *Med. Phys.*, 31:1195–202, 2004. 13

[47] W Cai, R Ning, and D L Conover. Simplified method of scatter correction using a beam-stop-array algorithm for cone-beam computed tomography breast imaging. *Opt Eng*, 47:97003, 2008. 13, IV

[48] X Liu, C Shaw, M Altunbas, and T Wang. TU-D-I-611-07: a scanning sampled measurement (SSM) technique for scatter measurement and correction in cone beam breast CT. *Med. Phys.*, 32:2093, 2005. 13, IV

[49] L Zhu, N Strobel, and R Fahrig. X-ray scatter correction for cone-beam CT using moving blocker array. *SPIE Proceedings, Bellingham, WA*, pages 251–8, 2005. 13, IV

[50] L Zhu, N R Bennett, and R Fahrig. Scatter correction method for X-ray CT using primary modulation: Theory and preliminary results. *TMI*, 25:1573–1587, 2006. 13, IV

[51] J S Maltz and W E Blanz et al. Cone beam X-ray scatter removal via image frequency modulation and filtering. *Proceedings of the 2005 IEEE, EMBS*, pages 1854–1857, 2005. 13, IV

[52] H Gao, R Fahrig, and N R Bennett. Scatter correction method for X-ray CT using primary modulation: phantom studies. *Med. Phys.*, 37:934–46, 2010. 13, IV

[53] A P Colijn and F J Beekman. Accelerated simulation of cone beam X-ray scatter projections. *TMI*, 23:584 – 590, 2004. 14, IV

[54] Y Kyriakou and W A Kalender. X-ray scatter data for flat-panel detector CT. *Phys. Med. Biol.*, 23:3–15, 2007. 14, IV

[55] A Malusek, M P Sandborg, and G A Carlsson. Simulation of scatter in cone beam CT: effects on projection image quality. *Proc SPIE*, 5030:740–51, 2003. 14, IV

[56] D Lazos and J F Williamson. Impact of flat panel-imager veiling glare on scatter-estimation accuracy and image quality of a commercial on-board cone-beam CT imaging system. *Phys. Med. Biol.*, 39:5639–5651, 2012. 14, 16, 61, IV

[57] G Jarry, S A Graham, and D J Moseley. Characterization of scattered radiation in kV CBCT images using Monte Carlo simulations. *Med. Phys.*, 33:4320–9, 2006. 14, IV

[58] W Zbijewski and F J Beekman. Efficient Monte Carlo based scatter artifact reduction in cone-beam micro-CT. *TIM*, 25:817–27, 2006. 14, IV

[59] G Jarry, S.A Graham, D A Jaffray, D J Moseley, and F Verhaegen. Scatter correction for kilovoltage cone-beam computed tomography (CBCT) images using Monte Carlo simulations. *SPIE Proceedings, Bellingham, WA*, page 614254, 2006. 14, IV

[60] M Bertram, T Sattel, S Hohmann, and J Wiegert. Monte-Carlo scatter correction for cone-beam computed tomography with limited scan field-of-view. *SPIE Proceedings, Bellingham, WA*, page 69131Y, 2006. 14, IV

[61] E Mainegra-Hing and I Kawrakow. Fast Monte Carlo calculation of scatter corrections for CBCT images. *JPCS*, 102:12017, 2008. 14, IV

[62] E Mainegra-Hing and I Kawrakow. Variance reduction techniques for fast Monte Carlo CBCT scatter correction calculations. *Phys. Med. Biol.*, 55:4495–507, 2010. 14, IV

[63] A Badal and A Badano. Accelerating Monte Carlo simulations of photon transport in a voxelized geometry using a massively parallel graphics processing unit. *Med. Phys.*, 36:4878–80, 2009. 14, IV

[64] X Jia, H Yan, L Cervino, M Folkerts, and S B Jiang. A GPU tool for efficient, accurate, and realistic simulation of cone beam CT projections. *Med. Phys.*, 39:7368–78, 2012. 14, IV

[65] V N Hansen, W Swindell, and P M Evans. Extraction of primary signal from EPIDs using only forward convolution. *Med. Phys.*, 24:1477–1484, 1997. 14, 15, 16, 18, 20, 61, IV, V

[66] L Spies, M Ebert, B A Groh, B M Hesse, and T Bortfeld. Correction of scatter in megavoltage cone-beam CT. *Phys. Med. Biol.*, 46:821–833, 2001. 15, 16, 18, 20, 61, IV, V

[67] J S Maltz, B Gangadharan, and S Bose et al. Algorithm for X-ray scatter, beam-hardening, and beam profile correction in diagnostic (kilovoltage) and treatment (megavoltage) cone beam CT. *TMI*, 27:1791–1810, 2008. 15, 20, 24, IV

[68] S F Petit, W J C Elmpt, S M J J G Nijsten, A L A J Dekker, and P Lambin. Correction of cupping artifacts in megavoltage cone beam computed tomography. *Department of Radiation Oncology (MAASTRO)*. 15, IV

[69] L A Love and R A Kruger. Scatter estimation for a digital radiographic system using convolution filtering. *Med. Phys.*, 14:178–85, 1987. 15, IV

[70] J A Seibert and J M Boone. X-ray scatter removal by deconvolution. *Med. Phys.*, 15:567–75, 1988. 15, IV

[71] S Naimuddin, B Hasegawa, and C A Mistretta. Scatter-glare correction using a convolution algorithm with variable weighting. *Med. Phys.*, 14:330–4, 1987. 15, IV

[72] D G Kruger, F Zink, W W Peppler, D L Ergun, and C A Mistretta. A regional convolution kernel algorithm for scatter correction in dual-energy images: comparison to single-kernel algorithms. *Med. Phys.*, 21:175–84, 1994. 15

[73] M Meyer, W A Kalender, and Y Kyriakou. A fast and pragmatic approach for scatter correction in flat-detector CT using elliptic modeling and iterative optimization. *Phys. Med. Biol.*, 55:99–120, 2010. 15, IV

[74] J Rinkel, L Gerfault, F Esteve, and J M Dinten. A new method for X-ray scatter correction: first assessment on a cone-beam CT experimental setup. *Phys. Med. Biol.*, 52:4633–4652, 2007. 16, 61

[75] N Bhatia, D Tisseur, F Buyens, and J M Létang. Scattering correction using continuously thickness-adapted kernels. *NDT & E*, 78:52–60, 2016. 16, 18, 20, 22, 39, 42, 43, 44, 61, 62, 63, 64, 82, VI, XII, XIII, XXV, XXVI, XXVII

[76] M Baer and M Kachelrieß. Hybrid scatter correction for CT imaging. *Phys. Med. Biol.*, 57:6849–6867, 2012. 16, 61

[77] W Zhao, S Brunner, K Niu, S Schafer, K Royalty, and GH Chen. Patient-specific scatter correction for flat-panel detector-based cone-beam CT imaging. *Phys. Med. Biol.*, 60:1339–65, 2015. 16, 61

[78] H Li, R Mohan, and X R Zhu. Scatter kernel estimation with an edge-spread function method for cone-beam computed tomography imaging. *Med. Phys.*, 53:6729–48, 2008. 16, 61, IV

[79] Y Kyriakou, M Meyer, R Lapp, and W A Kalender. Histogram-driven cupping correction (HDCC) in CT. *Proc. SPIE*, page 7622: 76221S, 2010. 16, IV

[80] J Wiegert, S Hohmann, and M Bertram. Iterative scatter correction based on artifact assessment. *SPIE Proceedings, Bellingham, WA*, page 69132B, 2008. 16, IV

[81] C Altunbas C, C C Shaw, and L Chen. A post-reconstruction method to correct cupping artifacts in cone beam breast computed tomography. *Med. Phys.*, 34:3109–18, 2007. 16, IV

[82] J Tabary, R Guillemaud, F Mathy, A Gliere, and P Hugonnard. Combination of high resolution analytically computed uncollided flux images with low resolution Monte Carlo computed scattered flux images. *TNS*, 51:212–217, 2004. 25

[83] N Bhatia, D Tisseur, F buyens, and J M Létang. Scattering correction in cone beam computed tomography using scatter kernel superposition. *DIR*, 2015. 82

[84] N Bhatia, D Tisseur, S Valton, and J M Létang. Separable scatter model of the detector and object contributions using continuously thickness-adapted kernels in CBCT. *JXST*, 2016. 82

[85] N Bhatia, D Tisseur, and J M Létang. Convolution-based scatter correction using kernels combining measurements and Monte Carlo simulations. *NDT&E*, 2016. 82

[86] G Poludniowski and P M Hasen et al. An efficient Monte Carlo-based algorithm for scatter correction in keV cone-beam CT. *Phys. Med. Biol.*, 54:3847–3864, 2009. 83

[87] E Spezi and P Downes et al. Monte carlo simulation of an X-ray volume imaging cone beam CT unit. *Med. Phys.*, 36:127–136, 2009. 83

[88] M Randazzo and M Tambasco. A rapid noninvasive characterization of ct x-ray sources. *Med. Phys.*, 42:3960–3968, 2015. 83

[89] E Y Sidky and L Yu et al. A robust method of x-ray source spectrum estimation from transmission measurements: Demonstrated on computer simulated, scatter-free transmission data. *JAP*, 2005. 83

[90] H H Liu, T R Mackie TR, and E C McCullough. Correcting kernel tilting and hardening in convolution/superposition dose calculations for clinical divergent and polychromatic photon beams. *Med. Phys.*, 24:1729–41, 1997. 83

FOLIO ADMINISTRATIF

THESE DE L'UNIVERSITE DE LYON OPEREE AU SEIN DE L'INSA LYON

NOM : **BHATIA** DATE de SOUTENANCE : **29/09/2016**

Prénoms : **Navnina**

TITRE : **Scattering Correction in Cone Beam Tomography using continuously thickness-adapted kernels**

NATURE : Doctorat Numéro d'ordre :

Ecole doctorale : **Électronique, Électrotechnique, Automatique**

Spécialité : **Traitement du Signal et de l'Image**

RESUME : La tomodensitométrie intégrant une source de rayons X à faisceau divergent et un détecteur grand champ est une technique bien connue dans le domaine de la tomographie industrielle. La nature des matériaux et les épaisseurs traversées conduisent inévitablement à la génération de rayonnement diffusé. Ce dernier est généré par l'objet mais également par le détecteur. La présence de rayonnement parasite conduit à ne plus respecter l'hypothèse de la loi de Beer-Lambert. Par conséquent, on voit apparaitre sur les coupes tomographiques des artefacts de reconstruction comme des streaks, des effets ventouses ou des valeurs d'atténuation linéaire erronée. Par conséquence, on retrouve dans la littérature de nombreuses méthodes de correction du diffusé. Ce travail vise à mettre en point et tester une méthode originale de correction du diffusé. Le premier chapitre de cette étude, dresse un état de l'art de la plupart des méthodes de corrections existantes. Nous proposons, dans le deuxième chapitre, une évolution de la méthode de superposition des noyaux de convolution (Scatter Kernel Superposition). Notre méthode repose sur une description continue des noyaux en fonction de l'épaisseur traversée. Dans cette méthode, les noyaux de diffusion sont paramétrés analytiquement sur toute la plage d'épaisseur. Le procédé a été testé pour des objets à la fois mono-matériaux et poly-matériaux, ainsi que sur des données expérimentales et simulées. Nous montrons dans le troisième chapitre l'importance de la contribution du diffusé détecteur dans la qualité de l'image reconstruite. Mais également l'importance de décrire les noyaux de convolution à l'aide d'un modèle à quatre gaussienne. Les résultats obtenus à partir de données expérimentales prouvent que la correction du diffusé de l'objet seul ne suffit pas pour obtenir une image de reconstruite sans artefacts. Afin de disposer d'une meilleur modélisation du diffusé du détecteur, nous décrivons, dans le dernier chapitre, une méthode basée sur la combinaison de données expérimentales et simulées permettant d'améliorer l'estimation des noyaux de diffusé.

MOTS-CLÉS : **Tomographie RX 3D, correction de diffusé, Contrôle Non Destructif (CND)**

Laboratoire (s) de recherche :

CEA - LIST, Département d'Imagerie et de Simulation pour le Contrôle (DISC)
Centre de Recherche en Acquisition et Traitement de l'Image pour la Santé (CREATIS)

Directeur de thèse: **Jean Michel Létang**

Président de jury :

Composition du jury : **Jean Michel Létang, David Tisseur, Jan Sijbers, Alessandro Olivo et Dimitris Visvikis**